

Environments and Structures of Explosively  
Developing Extratropical Cyclones in the  
Northwestern Pacific Region

Akira Yoshida

Division of Earth and Planetary Sciences, Graduate School of Science,  
Hokkaido University

## Abstract

The characteristics of explosively developing extratropical cyclones in the northwestern Pacific region were analyzed using the Global objectively ANALyzed data set (GANAL) provided by the Japan Meteorological Agency (JMA). In this thesis, these cyclones were classified into three types, depending on positions of formation and of rapid development: OJ cyclones originate over the eastern Asian continent and develop over the Sea of Japan or the Sea of Okhotsk; PO-L cyclones are also formed over the Asian continent and develop over the northwestern Pacific Ocean; and PO-O cyclones are formed and develop over the northwestern Pacific Ocean. Statistical analyses suggested that OJ cyclones frequently appeared in late fall and had the smallest deepening rates of the three types; PO-L cyclones had medium deepening rates and frequently occurred in early and late winter; and, PO-O cyclones mainly occurred in mid-winter and had the largest deepening rates.

Two kinds of composite analyses were conducted to understand the structures and the mechanisms of development. The first composite analysis used geographically fixed coordinates. The results suggested that the favorable atmospheric conditions for the development of each type of cyclone were closely connected to the presence and extension of the cold air mass over the Asian continent. In addition, these conditions were closely related to seasonal variations across the area. The other analysis of cyclone mesoscale structure, using cyclone relative coordinates at the maximum deepening rate, suggested that OJ cyclones had a short-wave, upper-level trough and a strong baroclinic zone in the lower level. PO-L cyclones, associated with a zonally stretched jet stream, had a remarkable mid-level baroclinic zone. PO-O cyclones with a strong jet streak, also had a distinct baroclinic zone in the mid-level and a large water vapor budget (precipitation minus evaporation) appeared around the cyclone center. A diagnosis using an geostrophic relative vorticity tendency equation and sensitivity experiments for the effect of latent heat release using a mesoscale numerical model suggested that cyclone structures reflected larger scale atmospheric environment, which affected the mechanism of cyclone development, and larger deepening rate of PO-O cyclones attributed to the latent heat release.

# Contents

<b>1</b>	<b>Introduction</b>	<b>1</b>
<b>2</b>	<b>Data sources and definition of the explosive cyclone</b>	<b>4</b>
2.1	Data sources . . . . .	4
2.2	Definition of the explosively developing cyclone . . . . .	4
<b>3</b>	<b>Statistical analysis</b>	<b>6</b>
3.1	Classification of explosively developing cyclones . . . . .	6
3.2	Statistical analysis . . . . .	7
<b>4</b>	<b>Planetary- and synoptic-scale environments</b>	<b>9</b>
4.1	Geographically fixed composite analysis . . . . .	9
4.2	Monthly averaged environments . . . . .	11
<b>5</b>	<b>Mesoscale structures and development factors</b>	<b>14</b>
5.1	Zwack-Okossi development equation . . . . .	14
5.2	Fixed cyclone center composite analysis . . . . .	17
<b>6</b>	<b>Numerical simulations of extreme cases</b>	<b>23</b>
6.1	Synoptic overview of extreme cases . . . . .	23
6.2	Model description . . . . .	25
6.3	Results of simulations and trajectory analyses . . . . .	26
6.4	Sensitivity experiments . . . . .	29
<b>7</b>	<b>Discussion</b>	<b>33</b>
7.1	Comparison with explosive cyclones in the north Atlantic region . . . . .	33
7.2	Contributions to the global energy and water transportation . . . . .	35
<b>8</b>	<b>Conclusions</b>	<b>39</b>

<b>Acknowledgments</b>	<b>42</b>
<b>References</b>	<b>43</b>
<b>Tables and figures</b>	<b>49</b>

# 1 Introduction

The rapid deepening of extratropical cyclones is one of the most exciting topics in modern meteorology, in academics as well as weather forecasting, natural disaster protection and traffic safety. Heavy precipitation and severe winds, which sometimes disturb human activities, are often reported with this event. Rapidly deepening cyclones are also considered to be an important contributor to global climate change and energy transportation. Chen et al. (1991) reported climatological characteristics of extratropical cyclones in eastern Asia, describing two active cyclogenesis areas: one downstream of the mountainous region across the Asian continent, the other over the East China Sea and the Sea of Japan. The former was related to lee cyclogenesis, the latter to coastal cyclogenesis in the east of the continent. Nitta and Yamamoto (1972, 1974) analyzed coastal cyclogenesis for medium-scale cyclones, which were defined as having wavelengths between 1000 and 2000 km. They reported statistical analyses and classified cyclones, but did not describe the physical implications. Saito (1977) reported a case study of medium-scale cyclones over the East China Sea during the Air-Mass Transformation Experiment (AMTEX) in 1975, and concluded that the crucial factors for cyclogenesis were warm air advection, synoptic scale updraft and heat supply from the sea surface. Coastal cyclones occasionally developed more rapidly than other cyclones.

Sanders and Gyakum (1980) defined an explosively developing extratropical cyclone as a cyclone that had a central sea level pressure decrease normalized at 60°N over 24 hPa in a day (24 hours). Explosively developing extratropical cyclones frequently appear in the cold seasons in the east of a continent, such as the northwestern Pacific Ocean and northwestern Atlantic Ocean (Sanders and Gyakum 1980; Roebber 1984). For the past two decades, researches of explosively developing cyclones had mainly focused on those over the North Atlantic Ocean. For example, the Experiment on Rapidly Intensifying Cyclones over the Atlantic (ERICA) (Hadlock and Kretzberg 1988) and the Fronts and Atlantic Storm-Track Experiment (FASTEX) (Joly et al. 1997) were conducted in the north Atlantic Ocean and provided detailed informations for explosively developing cyclones over the region. These investigations showed that the rapidly deepening

ing cyclones had complicated developing mechanisms and several atmospheric phenomena on various scales were interrelated, producing the explosive development. Shapiro et al. (1999) discussed a planetary-scale to mesoscale perspective of extratropical cyclones, and suggested that the planetary-scale environment such as tropopause folding, jet stream, upper-level high potential vorticity, and low-level baroclinicity influences the life cycles of extratropical cyclone. The structures and evolutions of explosively developing cyclones were investigated by Neiman and Shapiro (1993), Neiman et al. (1993), and Liu et al. (1997) from an observational point of view; by Chen and Dell'Osso (1987), and Kuo and Low-Nam (1990) from a numerical point of view; and, by Manobianco (1989), and Wang and Rogers (2001) using synoptic scale analyses. These papers suggested that a short-wave trough in the upper and middle troposphere approached over the shallow cyclone, inducing strong upward forcing, creating updrafts that occurred around the cyclone center in rapidly developing cyclones. Kuo and Low-Nam (1990) compared case studies using numerical models and examined the physical processes of cyclone development. Sinclair (1997), and Sinclair and Revell (2000) discussed upper- and lower-level conditions favorable to cyclogenesis, and reported that cyclogenesis frequently occurred above the equatorward of the SST gradient maxima and beneath the equatorward entrance and poleward exit of an upper-level jet streak.

In the northwestern Pacific region, Chen et al. (1992) showed that explosive cyclones often appeared over the Sea of Japan and over the Kuroshio current. They also suggested that two peaks of monthly frequency existed in early winter (January) and late winter (March) over the northwestern Pacific Ocean. However, Sanders and Gyakum (1980) reported a single peak, in February, occurred over the northwestern Atlantic Ocean. Except for studies by Bullock and Gyakum (1993), Kelly et al. (1994) and Gyakum and Danielson (2000), there have been few analyses of synoptic conditions for explosive cyclogenesis over the northwestern Pacific region.

The purpose of the present study is to characterize explosive cyclones in the northwestern Pacific region. Geographical and seasonal variation, and statistical properties are analyzed first using an objectively analyzed data set. Secondly, favorable synoptic and planetary-scale atmo-

spheric environments and mesoscale structures around the cyclone center are investigated using two kinds of composite analysis. Finally, extreme cases in the northwestern Pacific region are simulated using a mesoscale regional model to clarify air flows near the cyclone and a role of latent heat release.

Definition of explosively developing extratropical cyclone and data sources are described in section 2, and section 3 provides the result of statistical analysis. Section 4 provides larger scale environment and section 5 provides mesoscale structure and development factors. In section 6, results of numerical simulation for extreme cases are described. Differences from explosive cyclones in the North Atlantic region and roles on the global energy and water circulation are discussed in section 7. Conclusions are found in section 8.

## 2 Data sources and definition of the explosive cyclone

### 2.1 Data sources

The data source for the present study is the Global objectively ANALyzed data set (GANAL) provided by the Japan Meteorological Agency (JMA). GANAL data set includes sea level pressures, geopotential heights, air temperatures and dew point depressions with horizontal resolutions of  $1.875^\circ$  in latitude and longitude, and 16 vertical levels from the surface to 10 hPa, collected from March 1988 through February 1996. After this date, resolution improved to  $1.25^\circ$  for horizontal resolution, and to 18 vertical levels between the surface and 10 hPa. The temporal interval is 12 hours prior to April 1995, and 6 hours afterwards. Five cold seasons from 1 October 1994 to 31 March 1999 were used in the present analysis. To analyze synoptic overview of extreme cases in section 6, surface weather map provided by JMA are used. They cover over the northwestern Pacific region and temporal interval is 6 hours. To provide lower boundary conditions of a numerical simulation in section 6, Reynolds Sea Surface Temperature (SST) data provided by the National Oceanic and Atmospheric Administration-Cooperative Institute for Research in Environmental Sciences Climate Diagnostics Center (NOAA-CIRES CDC) is used. This data set provides weakly mean SST every  $1^\circ$  gridded point in latitude and longitude.

### 2.2 Definition of the explosively developing cyclone

A cyclone was defined at any grid point with sea level pressure at least one hPa lower than the value at an adjacent grid point. The cyclone deepening rate (unit: Bergeron) was calculated from the following definition for each cyclone:

$$\text{Cyclone deepening rate} = \left\{ \frac{p(t-6) - p(t+6)}{12} \right\} \cdot \frac{\sin 60^\circ}{\sin \frac{\phi(t-6) + \phi(t+6)}{2}}, \quad (1)$$

where  $t$  is analyzed time in hours,  $p$  is the sea level pressure at the cyclone center, and  $\phi$  is the latitude at the cyclone center. Although the definition of the cyclone deepening rate by Sanders and Gyakum (1980) used a 24-hour pressure change, a 12-hour pressure change

was used in this study to find an instance of the most rapid deepening in a cyclone's life period. An explosively developing cyclone was defined as having a deepening rate of at least 1 Bergeron within the analysis area which was taken between 100°E and 180°E in longitude and between 20°N and 65°N in latitude (the area surrounded by a bold solid line in Fig. 1(b)). Cyclones that disappeared within 24 hours after initial appearance were excluded from the analysis.

### 3 Statistical analysis

#### 3.1 Classification of explosively developing cyclones

In total, 224 explosively developing cyclones were analyzed. Figure 1 shows the locations of formation, maximum deepening and minimum center pressure. Although they formed over land and ocean (Fig. 1(a)), the maximum deepening almost always occurred over the ocean at latitudes greater than 35°N (Fig. 1(b)). The areas of maximum deepening were classified into two regions. One region was over the Sea of Japan and the Sea of Okhotsk, which are near the Asian continent, and the other was over the northwestern Pacific Ocean. Although most cyclones that deepened maximally (developed) over the Sea of Japan and the Sea of Okhotsk were formed on the Asian continent, those that developed over the Pacific Ocean were further classified into two types: those formed over the continent and those formed over the ocean. Therefore, three types of cyclones existed in total: formed over land and developed over the Sea of Japan or the Sea of Okhotsk (the Okhotsk-Japan Sea type, hereafter referred to as OJ type); formed over land and developed over the Pacific Ocean (the Pacific Ocean-Land type, referred to as PO-L type); and formed over the ocean and developed over the Pacific Ocean (the Pacific Ocean-Ocean type, referred to as PO-O type). Cyclone tracks from the place of formation to that of minimum center pressure are shown in Fig. 2. OJ cyclones formed over the continent and developed maximally during passage over the sea (Fig. 2(a)). PO-L cyclones were formed over the continent, moved across the Japan archipelago and developed over the Pacific Ocean (Fig. 2(b)). PO-O cyclones were formed over the ocean near the southern Asian continent, moved to south of Japan and developed over the ocean (Fig. 2(c)).

The cyclones identified as explosively developing cyclones are further classified into three categories of intensification: strong intensification (ST) cyclone is larger than 1.8 Bergeron; moderate intensification (MO) cyclone ranges between 1.3 and 1.8 Bergeron; and weak intensification (WE) cyclone is less than 1.3 Bergeron. These three classifications of intensification were followed by Sanders (1986).

## 3.2 Statistical analysis

The frequency of each type is summarized in Table 1. PO-O cyclones occurred most frequently (110 cases), followed by PO-L cyclones (50 cases) and OJ cyclones (42 cases). In the five cold seasons from October 1994 to March 1999, 202 cyclones were classified into the above three types, and the remaining 22 cases were unclassified. Of these, 14 formed and developed over the continent, 5 formed over the northwestern Pacific Ocean, moved northwestward and developed over the Sea of Okhotsk. The others formed over the Sea of Okhotsk, moved southeastward and developed over the northwestern Pacific Ocean. Most of OJ cyclones were categorized as WE and only three cases were ST. Most of PO-L cyclones were MO and most of PO-O cyclones were also categorized as MO. Approximately two third of ST cyclones belong to PO-O cyclones. Figure 3 shows the frequency distribution of maximum deepening rate of the three types. The average properties of PO-O, PO-L, and OJ cyclones were 1.51 Bergeron (standard deviation is 0.43 Bergeron), 1.49 Bergeron (standard deviation , 0.36 Bergeron) and 1.33 Bergeron (standard deviation, 0.30 Bergeron), respectively. This may indicate that PO-O cyclones are the strongest of the three, PO-L cyclones are next and OJ cyclones are the weakest. Although the frequency of OJ cyclones peaked at 1.1 - 1.2 Bergeron, frequency decreased nearly monotonically with intensity. PO-L and PO-O cyclones peaked at 1.3 - 1.4 Bergeron and 1.2 - 1.3 Bergeron, respectively, with several cases stronger than 2.0 Bergeron. The strongest deepening rate for the PO-O cyclones was about 3.0 Bergeron.

The distribution of monthly frequencies for the three types of cyclones during the five cold seasons from October 1994 to March 1999 are shown in Fig. 4. These frequencies for each season are also listed in Table 2. Figure 4(a) shows the total frequency of the explosively developing cyclones. Although the only a single peak, in January, was evident for “total” frequency, monthly frequency patterns were different among cyclone types (Figs. 4(b)-(d)). OJ cyclones peaked in November (late autumn), PO-L cyclones peaked in December (early winter) and February (late winter), and PO-O cyclones peaked in January (mid-winter). Although there are variations in occurrence in each season (Table 2), the above mentioned seasonal ap-

pearance tendencies for the different types are identifiable. Chen et al. (1992) reported that explosive cyclones frequently occurred in January and March over the northwestern Pacific Ocean, while Sanders and Gyakum (1980) reported only a peak in January over the northwestern Atlantic Ocean. While our target area is close to the analysis region of Chen et al. (1992), differences in frequencies between the types are evident.

In summary, explosively developing cyclones over the northwestern Pacific region were classified into three types by locations of formation and of maximum deepening, revealing different characteristic deepening intensities, with occurrence frequencies exhibiting distinct seasonal variations.

## **4 Planetary- and synoptic-scale environments**

### **4.1 Geographically fixed composite analysis**

Schultz et al. (1998) suggested that the surface frontal structure was changed by a larger scale flow and affected cyclone development. Wang and Rogers (2001) reported that environmental baroclinicity affected the geographical properties of the development of explosive cyclones. They also suggested that cyclone structures may change under the influence of atmospheric and geographical environments. To understand the influence of the larger scale environment on each type of cyclone, a composite analysis was conducted. Three cold seasons, from October 1996 to March 1999, were analyzed because of the coarse spatial resolution of the data set prior to 1996. Composite analysis was performed using geographically fixed positions for each type. All explosive cyclones that occurred during the three winter seasons were used in the analysis. The key time examined in the composite analysis was the time of the most rapid deepening.

Composite charts for OJ cyclones are shown in Fig. 5. An upper-level trough with large curvature can be seen to extend from Siberia to northeastern China at 300 hPa and 500 hPa. A confluence of wind occurred over China, a diffluence occurred over the northwestern Pacific Ocean, and a relatively short and weak jet streak associated with the trough was located over the Sea of Japan and Japan islands. A baroclinic zone was located over northern China and the east coast of the Asian continent at 850 hPa, behind which a cold air mass presented. The 850 hPa geopotential height was a minimum over the Sea of Okhotsk and a strong wind was identified southeast of the low. OJ cyclones developed along the southeastern boundary of the cold air mass. These conditions suggest that the low-level baroclinicity near the continental coast over the ocean and the upper- and middle-level vorticity advection associated with a short-wave trough are favorable factors for the development of OJ cyclones.

Composite analyses of PO-L cyclones are shown in Fig. 6. A zonally stretched strong jet stream associated with a long-wave upper-level trough can be seen near 35°N at 300 hPa and 500 hPa. The 850 hPa geopotential height was a minimum over the Kamchatka Peninsula. A baroclinic zone, which was weaker than that of OJ cyclones, extended over southern Japan

and east of Japan at 500 and 850 hPa. A cold air mass presented over the northeastern Asian continent and a low-level baroclinic zone was zonally extended over southern Japan and east of the Japan mainland. PO-L cyclones developed in a low-level baroclinic zone east of Japan and northeast of a zonally stretched jet stream.

Figure 7 shows composite analyses of PO-O cyclones. The upper-level trough became shorter than that of PO-L cyclones with its axis extending from Siberia to the northwestern Pacific Ocean through the Sea of Okhotsk in the upper and middle levels. An upper-level strong jet streak associated with the trough was located over the southeastern coast of Japan. The jet streak was stronger than that of PO-L cyclones at 300 and 500 hPa. A 850 hPa geopotential height was a minimum east of the Kamchatka Peninsula. The features were similar to the synoptic conditions reported by Bullock and Gyakum (1993), Kelly et al. (1994), and Gyakum and Danielson (2000). The baroclinic zone appeared over middle China at 300 hPa and the southeastern coast of Japan at 500 and 850 hPa. It was weaker than that of PO-L cyclones at 850 hPa and stronger at 500 hPa, which may be a result of the differences in the cold air extension from the east coast of the Asian continent to the baroclinic zone. Since the fetch of a cold air mass from the continent for PO-O cyclones was longer than for PO-L cyclones, the cold air mass was more heated by sea surface than for PO-L cyclones. Explosive deepening occurred under the diffluent region of the upper-level jet streak above the low-level baroclinic zone.

Figure 8 shows the difference fields between PO-L and PO-O (PO-L field minus PO-O field). A positive wind difference shows stronger (weaker) wind in PO-L (PO-O) cyclones than that in PO-O (PO-L) cyclones and vice versa. A positive region appeared approximately between 40°N and 50°N at 300 and 500 hPa, and a negative region appeared approximately between 25°N and 40°N. These difference field patterns show that upper- and mid-level winds were stronger in PO-L cyclones in the northern area than 40°N and were stronger in PO-O cyclones in the southern area. Namely, the jet stream in PO-L cyclones was located northward and that in PO-O cyclones was southward. For temperature difference fields, a positive temperature

difference indicates colder (warmer) in PO-O (PO-L) cyclones than in PO-L (PO-O) cyclones and vice versa. A positive region extended zonally from the southern Asian continent to the east of Japan islands at 850 and 500 hPa. This means that the cold air mass in the middle and lower atmosphere was more extended southward in PO-O cyclones than that in PO-L cyclones. The difference fields for wind and temperature suggested that the extension of the continental cold air mass causes the meridional shift of the jet stream through the thermal wind relationship.

The larger scale atmospheric conditions exhibited different features for each of the three types. These conditions reflect the presence and extension of a cold air mass over the Asian continent. The extension of the cold air mass was smaller for OJ cyclones and larger for PO-O cyclones. The upper-level trough, the jet streak and the low-level baroclinicity were associated with the presence of a cold air mass over the continent. OJ cyclones developed under a shorter upper-level trough located over the eastern Asian continent with a distinct low-level baroclinic zone over the Sea of Japan. PO-L cyclones developed under a zonally stretched upper-level jet stream near 35°N and a relatively weaker low-level baroclinic zone located over southern Japan and the northwestern Pacific Ocean. For PO-O cyclones, a strong jet streak was located over the southeast of Japan and a weaker low-level baroclinic zone extended from the southern coast of Japan to the northwestern Pacific Ocean. The cold air mass spread over the northwestern Pacific Ocean and the East China Sea. The seasonal variation of appearance frequency, as shown in Fig. 4, may be related to the extension of the cold air mass. This will be further discussed next.

## **4.2 Monthly averaged environments**

Statistical analysis suggests that there were two prominent characteristics of the three types of rapidly deepening cyclones in the northwestern Pacific region. One is seasonal variation of occurrence frequency and another is the relationship between maximum deepening rate and cyclone type. The former is consistent with the results of Chen et al. (1991), which showed that cyclogenesis over east Asia was active near 40°N in late fall and early winter, and near 30°N from mid-winter to late winter. The seasonal variation may reflect larger-scale atmospheric

conditions, such as the cold air mass over the Asian continent and the upper jet streak, as shown in previous section.

Figure 9 shows monthly averaged geopotential height and relative vorticity for the three cold seasons between October 1996 and March 1999 at 300 hPa, superimposed on the tracks of the explosively developing cyclones from formation to maximum deepening. Figure 10 shows monthly averaged potential temperature and its horizontal gradient at 850 hPa. These figures clearly show the tendency for explosive cyclones to form in the planetary-scale low-level baroclinicity between sub-tropical and sub-polar regions, and develop under the upper-level positive vorticity maximum. The upper-level positive vorticity maximum (Fig. 9) exhibits a zonal extension over northern Japan toward the east in the mid-winter of January and February, especially noticeable in January. This extends over the northern Sea of Japan and the Sea of Okhotsk in late autumn (November), and in early and late winter (December and March), but is weaker in October. As the strong cold air mass forms over the Asian continent in mid-winter, the low-level baroclinic zones (Fig. 10) extend over southern China, the East China Sea, and the southern coast of Japan toward the east in January and February, especially prominent in January. This extends from the northern China and southern Russia across the central Sea of Japan toward the east of Japan in early and late winter (December and March), and extends from the central continent along the western coastal line of the Sea of Japan in late autumn (November), then becomes weaker and slightly less easily identified above the central continent in autumn (October).

The northern baroclinic zone corresponded with tracks of OJ and PO-L cyclones, while the southern one corresponded with those of PO-O cyclones. The seasonal variation of baroclinic zone, in other words extension of cold air mass over the Asian continent, is consistent with monthly variation of frequency of each cyclone type as shown in Fig. 4. As the cold air mass affects the location and intensity of the upper jet stream and vorticity as well as those of the low-level baroclinic zone, it also affects the explosively development of the cyclone. These results reveal that the classification of explosively developing cyclones introduced in the present study

may reflect the planetary- and synoptic-scale atmospheric conditions in the northwestern Pacific region during the cold season.

## 5 Mesoscale structures and development factors

### 5.1 Zwack-Okossi development equation

The previous section discussed on the geographically fixed larger scale atmospheric environments. The analysis revealed that an upper-level jet stream and a low-level baroclinicity, which were related to the cold air mass over the continent, differed among cyclone types. However, their quantitative contributions to cyclone development were vague. A diagnosis using a geostrophic relative vorticity tendency equation will be used to investigate development mechanisms for extratropical cyclones. Figure 11 shows a scatter diagram between the maximum deepening rate and the surface vorticity tendency. The vorticity tendency was calculated using the geostrophic wind circulation increment by finite-difference method with a 12-hour interval. Values were averaged by an area within 500 km of the cyclone center 6 hours after observing the maximum deepening rate. The graph shows a positive correlation, and the surface cyclonic circulation indeed increased after cyclone rapid development. The relationship between the surface pressure tendency and the surface geostrophic vorticity tendency, which shows a relatively good positive correlation, depends on cyclone scale, speed, and magnitude. Figure 11 reveals that a diagnosis for the explosive cyclogenesis analysis through the geostrophic vorticity tendency would be appropriate.

The Zwack-Okossi development equation (Z-O equation) was used to diagnose explosive cyclogenesis (Zwack and Okossi 1986). The Z-O equation describes a geostrophic relative vorticity tendency at the lower boundary as a result of dynamic and thermodynamic forcing vertically integrated through the atmosphere. Zwack and Okossi (1986) derived the quasigeostrophic version and Lupo et al. (1992) generalized and simplified the equation, known as the “extended form.” This form may be appropriate for synoptic scale diagnoses, and is used in the present study neglecting the frictional term. The equation can be written as follows:

$$\frac{\partial \zeta_{gl}}{\partial t} = P_d \int_{p_t}^{p_l} (-\mathbf{V} \cdot \nabla \zeta_a) dp - P_d \int_{p_t}^{p_l} \left\{ \frac{R}{f} \int_p^{p_l} \frac{\nabla^2 (-\mathbf{V} \cdot \nabla T)}{p} dp \right\} dp$$

$$\begin{aligned}
& -P_d \int_{p_t}^{p_l} \left\{ \frac{R}{f} \int_p^{p_l} \frac{\nabla^2 \left( \frac{\dot{Q}}{c_p} \right)}{p} dp \right\} dp - P_d \int_{p_t}^{p_l} \left\{ \frac{R}{f} \int_p^{p_l} \frac{\nabla^2 (S\omega)}{p} dp \right\} dp \\
& = P_d \int_{p_t}^{p_l} (\text{VADV} + \text{TADV} + \text{LATH} + \text{ADIA}) dp, \tag{2}
\end{aligned}$$

where  $p_l$  is the pressure at the lower boundary (1000 hPa),  $p_t$  is the pressure at the upper boundary (50 hPa),  $\zeta_{gl}$  is the geostrophic relative vorticity at the lower boundary,  $\zeta_a$  is the absolute vorticity ( $\zeta_a = \zeta + f$ ,  $\zeta$  is the relative vorticity),  $f$  is the Coriolis parameter,  $R$  is the gas constant of dry air,  $\mathbf{V}$  is the horizontal wind,  $\dot{Q}$  is the diabatic heating and cooling rate,  $c_p$  is the specific heat at constant pressure,  $S$  is the static stability ( $S = -(T/\theta)(\partial\theta/\partial p)$ , where the  $\theta$  is potential temperature),  $\omega$  is the vertical motion in isobaric coordinates ( $\omega = dp/dt$ ), and  $P_d = 1/(p_l - p_t)$ . The first term in the right-hand side of Eq. (2), which is referred to as VADV, is dynamic forcing and the effect of horizontal absolute vorticity advection on the geostrophic relative vorticity tendency at the lower boundary. The second term (TADV) describes the effect of horizontal temperature advection, and the third term (LATH) represents diabatic heating and cooling. The fourth term (ADIA) is the effect of adiabatic temperature change due to vertical motion. Fourth-order and second-order finite difference methods were used for horizontal and vertical differentiations, respectively, and a trapezoidal method was used for vertical integration to calculate physical quantities. To reduce subsynoptic-scale noise, each term was smoothed by the two-dimensional second-order filtering scheme explained by Shapiro (1970). Results contain less than 25% of the original information with wavelengths smaller than 800 km, and about 89% or more with wavelengths larger than 1500 km.

Vertical velocities ( $\omega$ ) were calculated by the kinematic method (O'Brien 1970), derived from the vertical integration of horizontal divergence and the boundary conditions where vertical velocities are zero at 1000 hPa and 50 hPa. The diabatic heating and cooling rate ( $\dot{Q}$ ) expresses both explicit and implicit processes. Evaporative and radiative cooling processes were not considered. The explicit process was considered as the latent heat release on the grid scale and the implicit process as the convective latent heat release in the sub-grid scale. The explicit latent heat release was calculated using the methods of Krishnamurti and Moxim (1971) and Vincent

et al. (1977) for the grid scale, and was proportional to the vertical advection of the saturated specific humidity. This was calculated under the following conditions: 1) upward motion; 2) positive vertical gradient of saturated water vapor mixing ratio; and, 3) relative humidity  $\geq$  80%. The convective latent heat release in the sub-grid scale was calculated by Kuo's parameterization scheme (Kuo 1965,1974), improved by Edmon and Vincent (1976), Lin and Smith (1979), and Smith et al. (1984). Kuo's scheme parameterizes the convective latent heat release (CLHR) as follows:

$$\text{CLHR} = \frac{g(1-b)LM_t[T_c(p) - T(p)]}{\int_{p_t}^{p_b} (T_c - T) dp} \frac{\theta}{T}, \quad (3)$$

where  $M_t$  is the rate of moisture convergence from the surface to the cloud top,  $T$  is the environmental temperature,  $T_c$  is the temperature within the cloud,  $\theta$  is the potential temperature,  $L$  is the latent heat of condensation ( $2.501 \times 10^6$  J kg<sup>-1</sup> for  $T \geq -20^\circ\text{C}$ ,  $2.835 \times 10^6$  J kg<sup>-1</sup> for  $T < -20^\circ\text{C}$ ),  $p_b$  is the pressure at the cloud base, the base of the first conditionally unstable layer,  $p_t$  is the pressure at the cloud top, the level where the moist adiabat from the cloud base crosses the environmental sounding,  $g$  is gravitational acceleration, and  $b$  is the fraction of converged water vapor that moistens the atmosphere. When the mean relative humidity from the surface to 500 hPa (RHAV) was greater than 0.8,  $b$  was 0. When RHAV was smaller than 0.4,  $b$  was 1.0. When RHAV was between these two limiting values,  $b = 1.0 - \text{RHAV}$ . Following Rausch and Smith (1996), the geostrophic relative vorticity tendency at the lower boundary ( $\partial\zeta_{gl}/\partial t$ ) forced by each level above was calculated and then vertically integrated.

To evaluate the significance of Eq. (2), we compare the sum of the four terms on the right hand side (R.H.S.) and the surface vorticity tendency on the left hand side (L.H.S.). The surface vorticity tendency was evaluated using the finite-difference method with a 12-hour interval. Values were averaged within 500 km from the cyclone center, 6 hours after observing the maximum deepening rate. The results are shown in Fig. 12. The sum of each term on the R.H.S. would be equal to the surface vorticity tendency ( $\partial\zeta_{gl}/\partial t$ ) on the L.H.S., if excluded terms and errors in data and estimation are not considered. The sum of each term on the R.H.S. in Eq. (2) is somewhat overestimated. However, this result may be reasonable, as the tendencies estimated

by the R.H.S. in Eq. (2) show instant values at the maximum deepening rate and those on the L.H.S. show averaged values over 12 hours using the finite-difference method. The positive correlation between the two sides supports the justification of diagnosing the explosive deepening cyclones using Eq. (2).

## 5.2 Fixed cyclone center composite analysis

To investigate mesoscale structures and development mechanisms for each type of cyclone, another kind of composite analysis was conducted in which each element to be analyzed was superimposed over the position of the surface cyclone center at its maximum deepening rate. The analysis domain was the area within 1500 km from the cyclone center in the zonal and meridional directions. To reduce the influence of the cyclone strength dispersion, analyses were conducted on MO deepening cyclones, as discussed in section 3.1. Each term of Eq. (2) was also evaluated to provide an understanding of the development mechanisms.

Composite analyses of the geopotential heights, horizontal winds and vertical motions for each type of cyclone are shown in Fig. 13. The legends show the same scale of contour lines and arrows at each height (300, 500 and 850 hPa). On the whole, horizontal winds became stronger with height, stronger updrafts appeared in the middle level (500 hPa) and cyclonic circulation was evident in the lower level (850 hPa). Horizontal winds were weaker in OJ cyclones and stronger in PO-O cyclones. The wavelength of the upper-level trough was shorter in OJ cyclones and became longer in PO-L and PO-O cyclones. The upper-level jet streak was shorter and weaker in OJ cyclones, and was longer in PO-L cyclones. In PO-O cyclones, the upper-level jet streak clearly terminated near the center of the cyclones with horizontal winds diffluent east of the cyclone. Updrafts were stronger in PO-L and PO-O cyclones and weaker in OJ cyclones. Low-level strong winds were identified in the southeast quadrant, especially in PO-L and PO-O cyclones. Low-level winds tended to be drawn into the cyclone center and northward in PO-O cyclones, while the cyclones were zonally stretched and the air mass was found to move quickly ahead of the cyclone (eastward) in the PO-L case.

Figure 14 shows the relative vorticities and contributions of the VADV term to the surface vorticity tendency. Large cyclonic vorticities, associated with the upper-level trough, extended from the northwest to the cyclone center and were strongest in OJ cyclones. The contributions of VADV were stronger at 300 hPa and extended around the cyclone center, but were weaker in the middle and lower levels.

Composite maps for potential temperatures, their horizontal gradients and contributions of the TADV term are shown in Fig. 15. A meridionally extended baroclinic zone was identified in the lower level of OJ cyclones. While a strong and zonally extended baroclinic zone was present in PO-L and PO-O cyclones in the middle level, it was weaker in the lower level. As discussed in the previous section, each type of cyclone had a characteristic atmospheric environment structure reflecting the extension of a cold air outbreak over the ocean. These baroclinic structures revealed that OJ cyclones developed near the continent during the smaller cold air mass extension and PO-L and PO-O cyclones developed with a long distance fetch apart from the continent during the larger cold air mass extension. Since the strong jet stream was longer in PO-L cyclones, the baroclinic zone was zonally elongated in PO-L cyclones than that in PO-O cyclones. The TADV contributions were positive (deepening) in the eastern part of the cyclone due to warm air advection and negative (filling) in the western part due to the cold air advection at the lower level, while the TADV term was positive north or northwest of cyclones in the upper level. Contributions in the upper and lower levels were larger than those in the middle level.

Figure 16 shows moisture conditions of specific humidities and LATH contributions. Specific humidities were smaller in OJ and PO-L cyclones, but were significantly larger in PO-O cyclones. Moist air moved into the cyclone center from the south in PO-O cyclones, but moved eastward in OJ and PO-L cyclones except at the lower level. Although the contributions of LATH were larger near the cyclone center in the lower level of OJ and PO-L cyclones, the largest contributions were in PO-O cyclones. A significant amount of latent heat was released due to the low-level moist air advection under the strong mid-level updraft region (Fig. 13) in PO-O cyclones. A large amount of latent heat release may lead to the higher deepening rate of

PO-O cyclones, as discussed in section 3.2.

To estimate the contributions of each term to explosive cyclogenesis, correlations between each term on the R.H.S. and the surface vorticity tendency of the L.H.S. in Eq. (2) were plotted in Fig. 17. The surface vorticity tendency was averaged within 500 km around the cyclone center, 6 hours after observing the maximum deepening rate. The gradient of the regression line is a measure of the degree of the contribution to the cyclone development. Figure 17 shows that VADV, TADV and LATH positively contributed to cyclone development, while ADIA contributed negatively. The contribution of TADV was largest, with a high correlation coefficient among the positive contributors. This tendency can be seen in each type of cyclone. Except for this feature, LATH in PO-O cyclones had a larger contribution than that of the other two cyclone types and VADV in OJ cyclones was also larger. The negative contribution of ADIA was large in the order of PO-O, PO-L and OJ cyclones. As discussed in the first half of this section, these tendencies would be supported by composite analyses for mesoscale cyclone structures. The rapid deepening of cyclones occurred in the baroclinic zone, PO-O cyclones had a strong low-level moisture advection, and OJ cyclones had a strong upper-level vorticity advection. These factors characterize cyclone types and their mesoscale structures.

The results of the diagnostic study using Eq. (2) suggested that latent heat release has an important contribution to the explosive cyclogenesis as well as vorticity and temperature advectons. However, in the previous climatological studies for the midlatitude weather system (Hoskins and Valdes 1990; Paciorek et al. 2002), the "Eady index" (or called as the "Eady growth rate"),  $\sigma_{BI}$ , had been used. The Eady index was derived by Lindzen and Farrell (1980). The adiabatic quasi-geostrophic momentum, thermodynamic, hydrostatic and continuity equations on  $\beta$  plane can be written as follows:

$$\frac{\partial u_g}{\partial t} + u_g \frac{\partial u_g}{\partial x} + v_g \frac{\partial u_g}{\partial y} = f_0 v_{ag} + \beta y v_g, \quad (4)$$

$$\frac{\partial v_g}{\partial t} + u_g \frac{\partial v_g}{\partial x} + v_g \frac{\partial v_g}{\partial y} = -f_0 u_{ag} - \beta y u_g, \quad (5)$$

$$\frac{\partial}{\partial t} \left( \frac{\partial \phi'}{\partial p} \right) = - \left( u_g \frac{\partial}{\partial x} + v_g \frac{\partial}{\partial y} \right) \left( \frac{\partial \phi'}{\partial p} \right) - \sigma \omega, \quad (6)$$

$$\frac{\partial \phi}{\partial p} = -\alpha, \quad (7)$$

$$\frac{\partial u_{ag}}{\partial x} + \frac{\partial v_{ag}}{\partial y} + \frac{\partial \omega}{\partial p} = 0, \quad (8)$$

where  $u_g$  and  $v_g$  are geostrophic winds,  $u_{ag}$  and  $v_{ag}$  are ageostrophic winds,  $\beta = df/dy$ ,  $f = f_0 + \beta y$ ,  $\phi'$  is geopotential perturbation,  $\alpha$  is specific volume, and  $\sigma = -(\alpha/\theta)(d\theta/dp)$ . Perturbations ( $u'$ ,  $v'$ ) in a zonal basic flow ( $\bar{u}$ ) in a baroclinic atmosphere can be written as follows:

$$u = \bar{u}(y, z) + u' = -\frac{\partial \bar{\psi}}{\partial y} - \frac{\partial \psi'}{\partial y}, \quad (9)$$

$$v = v' = \frac{\partial \psi'}{\partial x}, \quad (10)$$

where  $\psi$  is streamfunction. To substitute these to the above equations leads to the linearized potential vorticity and thermodynamic equations as follows:

$$\left( \frac{\partial}{\partial t} + \bar{u} \frac{\partial}{\partial x} \right) \left( \nabla^2 \psi' + \frac{f_0^2}{\sigma} \frac{\partial^2 \psi'}{\partial p^2} \right) + \frac{\partial \psi'}{\partial x} \frac{\partial}{\partial y} \left[ \frac{\partial^2 \bar{\psi}}{\partial y^2} + \beta(y - y_0) + \frac{f_0^2}{\sigma} \frac{\partial^2 \bar{\psi}}{\partial p^2} \right] = 0 \quad (11)$$

$$\left( \frac{\partial}{\partial t} + \bar{u} \frac{\partial}{\partial x} \right) \left( \frac{\partial \psi'}{\partial p} \right) - \frac{\partial \psi'}{\partial x} \frac{\partial \bar{u}}{\partial p} + \frac{\sigma}{f_0} \omega = 0 \quad (12)$$

Lindzen and Farrell (1980) assumed a solution of Eq. (11) whose form was as follow:

$$\Psi = \psi(z) e^{\frac{z}{2H}} e^{ik(x-ct)}, \quad (13)$$

where  $H$  is scale height for constant density and  $z$  is height. The equation for geostrophic streamfunction can be obtained by substituting the solution to Eq. (11):

$$\frac{\partial^2 \psi}{\partial z^2} + \left( \frac{\beta}{\epsilon} + \frac{1}{H} \frac{d\bar{u}}{dz} - \frac{d^2 \bar{u}}{dz^2} - \frac{k^2}{\epsilon} - \frac{1}{4H^2} \right) \psi = 0, \quad (14)$$

where  $\epsilon = f^2/N^2$  and  $N$  is the Brunt-Väisälä frequency. The upper and lower boundary conditions were obtained to substitute  $\omega = 0$  at the boundaries to Eq. (12):

$$\frac{\partial \psi}{\partial z} + \frac{1}{2H} \psi - \frac{\frac{d\bar{u}}{dz}}{\bar{u} - c} \psi = 0, \quad (15)$$

at  $z = 0$  and  $z = z_T$ . They numerically solved Eq. (14) for several  $d\bar{u}/dz$ ,  $\beta$ ,  $H$  and  $\epsilon$  with the boundary conditions and calculated the maximum growth rates,  $(kci)_{max}$ , which corresponded

to the Eady index. In result, they defined the Eady index as follow:

$$\sigma_{BI} = 0.31 \frac{f}{N} \left| \frac{\partial \mathbf{v}}{\partial z} \right|, \quad (16)$$

where  $\mathbf{v}$  is the horizontal wind vector. Thus, the Eady index indicates the maximum growth rate of adiabatic perturbation in quasi-geostrophic baroclinic flow on  $\beta$  plane with a constant vertical wind shear and static stability.

To compare explosive cyclogenesis with adiabatic linear baroclinic theory, the Eady index were calculated around the cyclone center at the maximum deepening rate. Figure 18 shows scatter diagrams between the maximum deepening rates and the Eady indices at 650 hPa, which were calculated with 300 and 1000 hPa winds and potential temperatures 6 hours before observing the maximum deepening rate, and values were averaged over an area within 500 km of the cyclone center. The gradient of the regression line is a measure how much the adiabatic (dry) baroclinic theory explains the cyclone deepening rate. Every panels show a positive correlation between maximum deepening rates and the Eady indices. OJ cyclones showed smaller gradient with a small correlation coefficient of the three types. PO-L and PO-O cyclones had relatively larger gradient with coefficients. Several extreme cases that had larger deepening rates showed distinct large discrepancy than that expected by the regression line. Especially, the discrepancies of the extreme cases in the PO-O cyclones was largest of the three types. These results suggest that the explosive cyclogenesis cannot be explained simply by the Eady index assuming adiabatic (dry) baroclinic instability and the tendency became larger for extreme cases which had larger maximum deepening rate, even if OJ cyclones in which the contribution of latent heat release was small.

As shown in this section, the cyclone mesoscale structures reflected the large-scale environment, which affected the cyclongenesis mechanism, and the explosive development could not be explained simply by linear adiabatic baroclinic theory. The OJ cyclones explosively developed due to upper-level vorticity advection and low-level temperature advection, which reflected upper-level short-wave trough and lower stronger baroclinicity along the east coast of the Asian continent. The PO-L cyclones mainly developed by temperature advection and

vorticity advection and latent heat release secondary, because the upper zonally stretched jet stream was dominant and spread precipitation area eastward. The PO-O cyclones explosively developed due to large latent heat release, because large amount of moisture over the north-western Pacific Ocean condensed near the cyclone center due to strong updrafts which were dynamically forced under the exit of the upper-level jet streak.

## 6 Numerical simulations of extreme cases

### 6.1 Synoptic overview of extreme cases

Two kinds of composite analysis showed differences of the large-scale atmospheric environments and mesoscale structures for the three types of explosive cyclones. Composite analyses show averaged structures but they may mask important structures of the extreme cyclone cases which produce large deepening rates. It may also be interesting how the explosive cyclones evolve to characterize features. In this section, the most extreme case in each of the three cyclone types during three cold seasons between 1 October 1996 and 31 March 1999 simulates with a mesoscale numerical model. The extreme OJ case was between 1200 UTC 24 February and 1800 UTC 3 March 1999, explosively developed at 1200 UTC February 1999 and its maximum deepening rate was 1.84 Bergeron. The extreme PO-L case was between 1800 UTC 7 and 0000 UTC 13 February 1998, explosively developed at 1800 UTC 10 February 1998 and its maximum deepening rate was 2.54 Bergeron. The extreme PO-O case was between 0000 UTC 29 December 1997 and 0000 UTC 3 January 1998, explosively developed at 0000 UTC 31 December 1997 and its maximum deepening rate was 2.96 Bergeron. First of all, synoptic overviews of extreme cases would be described using surface weather maps provided by JMA. Figure 19 shows the track and central sea-level pressure of each of extreme cyclones from its formation to disappearance. These positions and magnitudes were read out from JMA weather charts. A time series of surface weather maps of 24 hours intervals before and after the most explosively developing rate are shown in Fig. 20 for the OJ case, Fig. 21 for the PO-L case, and Fig. 22 for the PO-O case, respectively.

As shown in Figs. 19(a) and (b), the extreme OJ cyclone formed over the Asian continent at 1200 UTC 24 February 1999, moved eastward, and had the maximum deepening rate at 1200 UTC 27 February 1999 over the Sea of Okhotsk. After then the cyclone stayed there for a while, it achieved the minimum central sea-level pressure, which was 960 hPa at 0600 UTC 28 February 1999, and disappeared at 1800 UTC 3 March 1999. The cyclone was located over the northern Sea of Japan and the central sea-level pressure was 1004 hPa at 1200 UTC 26

February 1999 (Fig. 20(a); 24 hours before its maximum deepening rate). A cold front extended along the east coast of the Asian continent, and another small cyclone (1010 hPa) with frontal systems can be seen over the southern Japan mainland. A strong anticyclone (1046 hPa) was located over the north of China and spread over the continent. The cyclone moved over the Sea of Okhotsk at 1200 UTC 27 February 1999 (Fig. 20(b)), it had the maximum deepening rate and its central sea-level pressure deepened down to 972 hPa. The weather chart shows that the northern part of cold front began to occlude and elongated southwestward over the northwestern Pacific Ocean. The cyclone somewhat moved northeastward at 1200 UTC 28 February 1999 (Fig. 20(c); 24 hours after its maximum deepening rate) and its central sea-level pressure became 960 hPa which was the minimum throughout the cyclone life. The occluded front elongated southeastward from the cyclone center, and continued to the cold front which extended southeastward bending southwestward over the northwestern Pacific Ocean.

Figures 19(c) and (d) show the track and central sea-level pressure of the extreme PO-L cyclones. The cyclone formed over the Asian continent at 1800 UTC 7 February 1998, rapidly moved eastward, and developed explosively after passing over Japan at 1800 UTC 10 February 1998. After that, the cyclone continued to move eastward, its central sea-level pressure minimized with 968 hPa at 1800 UTC 11 February 1998 and disappeared at 0000 UTC 13 February 1998. The cyclone was located over the southern Sea of Japan at 1800 UTC 9 February 1998 (Fig. 21(a); 24 hours before analyzing the maximum deepening rate) and its central sea-level pressure was 1010 hPa. A cold front extended southwestward from the cyclone center and a warm front was short. We can also see a large cyclone existed over the central North Pacific Ocean, and a relatively weak anticyclone (1026 hPa) was located over China. When the cyclone developed explosively at 1800 UTC 10 February 1998 (Fig. 21(b)), the cyclone was located offshore east of Japan and its central sea-level pressure was 980 hPa. The cold front elongated westward. The cyclone moved more eastward at 0600 UTC 11 February 1998 (Fig. 21(c); 24 hours after then) with deepening and its central sea-level pressure achieved 968 hPa at 1800 UTC 11 February 1998, which was the minimum central sea-level pressure of the cyclone. A

front did not analyzed around the cyclone center, and a secondary cyclone analyzed with warm and cold fronts.

The track and central sea-level pressure of the extreme PO-O case are shown in Figs. 19(e) and (f). The cyclone formed over the west coast of the East China Sea at 0000 UTC 29 December 1997. It moved northeastward and experienced explosive development at 0000 UTC 31 December 1997 over the northwestern Pacific Ocean. The cyclone kept moving northeastward and the central sea-level pressure minimized with 960 hPa. After then, the cyclone turned northwestward with rapid filling and disappeared over the north of the Sea of Okhotsk. The cyclone was located over the south coast of Japan at 0000 UTC 30 December 1997 (Fig. 22(a); 24 hours before analyzing the maximum deepening rate) associated with a cold front which extended southwestward and a shorter warm front which extended eastward. Its central sea-level pressure was 1006 hPa. A large anticyclone (1040 hPa) was located over the central Asian continent and spread eastward. When the maximum deepening occurred at 0000 UTC 31 December 1997 (Fig. 22(b)), the cyclone was located over the offshore east of Japan. Its central sea-level pressure deepened down to 974 hPa, and the cold front elongated southward. The cyclone continued deepening by 0000 UTC 1 January 1998 (Fig. 22(c)), moved northeastward. Its central sea-level pressure became 960 hPa, which was the minimum central sea-level pressure of the cyclone. The fronts were not analyzed near the cyclone center and a secondary cyclone analyzed with warm and cold fronts.

## **6.2 Model description**

The Pennsylvania State University-National Center for Atmospheric Research (PSU-NCAR) fifth-generation Mesoscale Model (MM5), a nonhydrostatic, primitive-equation model (Grell et al. 1995), was used to simulate for extreme cyclone cases. Simulations were initiated at 24 hours before analyzing the maximum deepening rate and conducted for 48 hours; the OJ case started at 1200 UTC 26 February 1999, the PO-L case started at 1800 UTC 9 Feb 1998, and the PO-O case started at 0000 UTC 30 December 1997.

The GANAL data set was used as initial and lateral boundary conditions. Reynolds SST data set which was provided by NOAA-CIRES CDC was used as the sea surface temperature condition. A two-way, two-domain nested grid in the Lambert conformal projection map was used. Horizontal resolution of outer domain was 45 km with  $200 \times 160$  grid points and that of inner domain was 15 km with  $301 \times 271$  grid points. Centers of each domain set up the position of the surface cyclone center at the maximum deepening rate. The domains for the each case are shown in Fig. 23. Vertical resolution was 23 sigma levels from surface to 100 hPa. The simple ice explicit moisture scheme, which predicts water vapor, cloud water, and rain water for the air temperature above  $0^{\circ}\text{C}$  and cloud ice and snow in stead of cloud water and rain for below  $0^{\circ}\text{C}$ , was used for the outer domain (Dudhia 1989). For the inner domain, mixed-phase explicit moisture scheme, that also predicted supercooled water along with simple ice scheme (Reisner et al. 1998). Grell's cumulus parameterization (Grell 1993) was used to represent subgrid-scale convective precipitation for both domains.

### **6.3 Results of simulations and trajectory analyses**

Geopotential heights, cyclonic (positive) relative vorticity and horizontal wind speeds at 300 hPa are shown in Fig. 24 for the extreme OJ case. Sea-level pressure, 850 hPa temperature, vertically integrated rain water and precipitable water are shown in Fig. 25. Cyclone tracks, its central sea-level pressure and deepening rates are shown in Figs. 30 and 31. A cyclone, associated with an upper narrow trough over the Asian continent, was well simulated over the north of the Sea of Japan at  $T = 12$  h (0000 UTC 27 February 1999, Figs. 24(a) and 25(a)). An upper-level relative vorticity maximum was located at the southern edge of the trough and a relatively weak jet streak was located over the southern Sea of Japan. The large amount of precipitable water appeared along the south coast of Japan. Vertically integrated rain water also occurred in this area. As the cyclone developed, the upper vorticity maximum advected over the cyclone center and the leading edge of jet streak elongated northeastward (Figs. 24(b) and (c)). Vertically integrated rain water increased along the cold front but was not remarkable

around the cyclone center (Figs. 25(b) and (c)). The cyclone tracks analyzed in GANAL data set(GANAL) and those simulated by numerical model (CNTL) are shown in Fig. 30(a). The simulated cyclone track shifted northward compared with GANAL analysis. Figures 31(a) and (b) show time series of the central sea-level pressures and deepening rates. The central sea-level pressures were a little deeper in simulation than those in GANAL analysis. Simulated deepening rate at  $T = 24$  h (1200 UTC 27 February 1999) was 1.55 Bergeron and it was smaller than GANAL analysis. The simulated maximum deepening rate was 1.78 Bergeron at  $T = 16$  h (0400 UTC 27 February 1999) and the central pressure depression from the Beginning ( $T = 0$ ) to the minimum central sea-level pressure was 53 hPa. GANAL analyses were 1.84 Bergeron and 49 hPa, respectively. Although there were some differences, the numerical model simulated the cyclone well for this case.

The results for the extreme PO-L case are shown in Figs. 26, 27, 30(b), 31(c) and (d). The cyclone was located offshore east of Japan at  $T = 12$  h (0600 UTC 10 February 1998, Fig. 27(a)) with some amount of vertically integrated rain water around the cyclone center. An upper level zonally stretched jet stream extended along the  $30^{\circ}\text{N}$  latitude line, a short-wave trough approached to the surface cyclone center from the northwest (Fig. 26(a)). After  $T = 24$  h (1800 UTC 10 February 1998), vertically integrated rain water and moist area gradually separated eastward from the cyclone center, and an upper vorticity maximum advected over the cyclone center (Figs. 27(b), (c), 26(b), and (c)). Although the simulated cyclone track showed good correspondence with the GANAL analysis (Fig. 30(b)), the deepening rate at  $T = 24$  h (1800 UTC 10 February 1998), was 1.24 Bergeron and it was relatively smaller than the GANAL analysis, and temporal evolution of the simulated central pressure was also somewhat different from the analysis (Figs. 31(c) and (d)). The maximum deepening rate through the simulated period was 1.85 Bergeron at  $T = 16$  h (1000 UTC 10 February 1998) and this was also smaller than the analysis. There were two peaks in the deepening rate at  $T = 15$  h and 33 h, The maximum central pressure depression from the beginning ( $T = 0$ ) was 42 hPa. This is approximately the same as the analysis (40 hPa).

In the extreme PO-O case, the cyclone was located southeast of Japan at  $T = 12$  h (1200 UTC 30 December 1997) and large amount of vertically integrated rain water appeared around the cyclone center (Fig. 29(a)). An upper short-wave trough was relatively weak, associated with a short jet streak over the south coast of Japan (Fig. 28(a)). During explosive development, the cyclone had comma shaped region where considerable vertically integrated rain water occurred (Fig. 29(b)). At upper level, another jet streak appeared north of the cyclone and vorticity maximum associated with short-wave trough strengthened (Fig. 28(b)). The northern jet streak was weakened, the area of large amount of vertically integrated rain water separated from the cyclone center, keeping its intensification at  $T = 36$  h (Fig. 29(c)). The deepening rate was 2.38 Bergeron at  $T = 24$  h (0000 UTC 31 December 1997) and the maximum deepening rate showed 2.75 Bergeron at  $T = 16$  h (1600 UTC 30 December 1997). The maximum pressure depression from the beginning ( $T = 0$ ) was 51 hPa in simulation which was comparable with the GANAL analysis (52 hPa). The simulations reproduced well the PO-O explosive cyclone.

Air flows near the cyclone center were different in the three type of cyclones. Visualizing air flow nears the cyclone center provides us an important information on the origin of the air parcels and characterizes the cyclogenesis. To achieve the purpose, forward and backward trajectory analyses near the cyclone center were conducted. Winds were linearly interpolated every 15 minutes using 2-hours model output in outer domain. At first, air parcels were placed at  $7 \times 7 \times 7$  points, whose horizontal center corresponded with the surface cyclone center. Air parcels were placed at every 450 km in horizontal and at 850, 700, 600, 500, 400, 300, and 200 hPa in vertical, as shown in Fig. 32. Forward and backward trajectories were calculated from  $T = 24$  h.

Trajectories for the extreme OJ case are shown in Fig. 33(a). The streams which originated west of the upper trough came downward west of the cyclone (brown lines), cyclonic circulations associated with the upper trough were located over surface cyclone center (purple lines). Southern jet stream confluent southwest of cyclone (green lines), and low-level air rose around the cold front to the northeast of the cyclone center (blue lines). These features

were consistent with the structure described in section 5. Since moist air over the northwestern Pacific Ocean rose around the cold front which was south of the cyclone (blue lines), the effect of latent heat release in the updraft did not contribute much to deepen the cyclone center.

The result of trajectory analysis for the PO-L cyclone displayed characteristic structure of the PO-L cyclone (Fig. 33(b)). Zonal flow was dominant (green and pink lines) in the upper level and downdrafts associated with upper short-wave trough appeared northwest of cyclone (brown lines). Updrafts were located around the cyclone center, but they stretched eastward because of strong upper- and mid-level zonal flows (blue lines). These results reveal that precipitation produced in updraft spread eastward and cannot concentrate near the cyclone center due to strong zonal flows.

For the extreme PO-O cyclone, trajectory analysis shows that stronger updrafts occurred around the cyclone center and lifted air parcels flowed out at upper level at the north of the surface cyclone where strong winds appeared in Fig. 28 (blue lines in Fig. 33(c)). The region was between the cyclonic circulation associated with the short-wave trough (red lines) and the southern jetstream (pink lines). Although downdrafts from west of the upper trough appeared northeast of cyclone, they were weaker than the OJ and PO-L cyclones (brown lines). These results reveal that strong updraft associated with precipitation near the cyclone center contributes to the cyclogenesis.

These results of trajectory analyses showed the characteristic stream structures for the three types and the structures corresponded with the features shown by composite analyses in section 4 and 5. Especially, updrafts near the cyclone center indicated the characteristics of the three types, reflected larger scale environment and were related to precipitation distributions. In the next section, the influences of updrafts and latent heat release are focused.

## **6.4 Sensitivity experiments**

As discussed in section 5, contribution rate of latent heat release was one of the most characteristic factors among the three types. The results of trajectory analyses and numerical simu-

lations also showed that updrafts and precipitation production were characteristics in the three types. However, it has not been clarified how latent heat release affects cyclone evolution and deepening. In this section, to understand the effect of latent heat release, a sensitivity experiment was conducted. The simulations were conducted in the same conditions without the latent heat release during water vapor condensation in previous section.

The results for no-latent heat release simulation (DRY) of the extreme OJ cyclone are shown in Figs. 34 and 35, and the maximum deepening rates at  $T = 24$  h (1200 UTC 27 February 1999) are listed in Table 3. Compared with CNTL run in Figs. 24 and 25, the structure of the cyclone and the upper trough in DRY run were not so different each other. However, amount of vertically integrated rain water and precipitable water around the cold front decreased and upper jet streak northeastward extension became smaller. To understand the effect of latent heat release near the cyclone center, updrafts were focused. Figures 36 and 37 show trajectories which lifted up within updraft region near the cyclone center in CNTL and DRY runs, respectively. The vertical cross section in the lower panel shows the trajectories projected on the plane (A-B) the upper panel. In CNTL run, air parcels flowed from southwest and southeast into the cyclone center, and rose suddenly near the cyclone center up to 7000 m in height which corresponded to the tropopause. Horizontal trajectories seem to be the same in DRY run as those in CNTL run. However, vertical structures were different from CNTL run. Air parcels rose slowly and were lifted up at about 5000 m in height, did not reach at the tropopause level. There were not rain water in either of CNTL and DRY runs. The development rate in DRY run was 0.97 Bergeron at  $T = 24$  h and it was smaller than that in CNTL run (Fig. 31(a) and Table 3). Figure 30(a) shows cyclone tracks of GANAL, CNTL, and DRY runs for the extreme OJ case. The cyclone track was not so different between CNTL and DRY runs (Fig. 30(a)).

The result of DRY run for the extreme PO-L cyclone is shown in Figs. 38 and 39. The most different points appeared in precipitation and moist distribution. Large amount of vertically integrated rain water spread over warm sector in DRY run, while it concentrated frontal zone in CNTL run. The amount of precipitable water in warm sector also decreased compared with

CNTL run. Additionally, upper vorticity field did not fluctuate in DRY, although the downstream ridge amplified and a jet stream divided to two jet streaks in CNTL run. Rising trajectories near the cyclone center in CNTL run are shown in Fig. 40. Air parcels rapidly rose up to 7000 m in height and moved eastward associated with some amount of rain water. The number of rising air parcels decreased in DRY (Fig. 41) and upward velocity was slower than that in CNTL run. However, the highest level was not so different from that in CNTL. This reveals that large-scale forcing associated with strong upper-level zonal jet stream, may be dominant in this case. Thus, potential vorticity distribution did not almost change between CNTL and DRY. In result, deepening rate of DRY PO-L case decreased and it was 0.72 Bergeron at  $T = 24$  h (1800 UTC 10 February 1998, Fig. 31(d)). Cyclone tracks show in Fig. 30(b) that propagation speed was slower than that in CNTL run. This may be the result of decrease of vertical connection between the upper level disturbance and the surface cyclone due to no latent heat release.

The DRY simulation of extreme PO-O case showed the largest difference from the CNTL run in the three cases. Vertically integrated rain water distribution spread over the warm sector as same as the extreme PO-L case, and the amounts of it and precipitable water remarkably decreased than those in CNTL run (Figs. 29 and 43). The northern jet streak disappeared at upper level, so that vorticity maximum was not intensified and modified (Fig. 42). Trajectories rising near the cyclone center clarified the difference between CNTL and DRY runs. Rising air parcels concentrated around the cyclone center in the CNTL run (Fig. 44) rapidly rose and rain water concentrated. They reached up to 10000 m in height and moved eastward. The air flow diverged in the upper level of the northeast of cyclone and produced the northern strong wind region. the number of rising air parcels was almost the same in DRY run (Fig. 45) as that in CNTL run in contrast with the PO-L case. However, updraft was much weaker and air parcels reached up to 7000 m in height at the maximum. Therefore upper-level northeastern strong wind did not appear. As a result, deepening rate dramatically decreased from 2.86 Bergeron in CNTL run to 0.71 Bergeron at  $T = 24$  h in DRY run (Fig. 31), movement speed was also slower and finally the cyclone separated into two cyclones (Figs. 30 and 43(c)).

These results reveal that the effect of latent heat release are different between cyclone types. The distributions of vertically integrated rain water are decided by combination between dynamic upward forcing and amount of moisture. In the extreme OJ case, the amount of vertically integrated rain water was larger near the cold front over the northwestern Pacific Ocean, while it was smaller near th cyclone center, because more moisture existed over the northwestern Pacific Ocean than the Sea of Japan and Sea of Okhotsk. In the extreme PO-L case, latent heat release sharpened the front and it did not contribute to deepen the cyclone center. In the extreme PO-O case, the updraft at the exit of the upper jet streak and moisture distribution made good combination to promote explosive cyclogenesis. Therefore, the PO-O cyclones are driven by latent heat release mainly, and the cyclones could not developed explosively without latent heat release.

## 7 Discussion

### 7.1 Comparison with explosive cyclones in the north Atlantic region

As mentioned in section 1, the North Atlantic region is another region where explosive cyclones most frequently occur in the northern hemisphere (Sanders and Gyakum 1980; Roebber 1984; Sinclair 1997) and many investigators have studied. Explosive cyclones in the northwestern Pacific region will be compared with those in the North Atlantic region in this section.

As shown in sections 3 and 4, the tracks of explosive cyclones in the northwestern Pacific region show a seasonal variation due to the effect of the continental cold air mass extension. Blender et al. (1997) classified cyclone tracks into the zonal, the north-westward and stationary clusters over the North Atlantic Ocean, and reported that most of rapidly deepening cyclones was classified as the north-westward tracks. Although Ueno (1993), Sickmüller et al. (2000) and Geng and Sugi (2001) reported that the several years variability of cyclone tracks in the region was related to the North Atlantic Oscillation (NAO) and SST variation, any seasonal variation of storm track had not been described in the North Atlantic region,

To compare seasonal variation in the northwestern Pacific region with that in North Atlantic region, monthly averaged fields in the North Atlantic region between 1996 and 1999 are shown in Figs. 46 and 47. Figure 46 shows the upper-level conditions (300 hPa) and Figure 47 shows the lower level conditions (850 hPa). In general, the upper-level vorticity in the North Atlantic region is weaker than that in the northwestern Pacific region (refer to Fig. 9) and no remarkable seasonal variation can be found. This may reveal that upper conditions have large variability in the Atlantic region. Monthly averaged fields of 850 hPa potential temperature and its horizontal gradient show a clear seasonal variation. A baroclinic zone begins to form along the east coast of the North American continent in November. The baroclinic zone intensifies and another baroclinic zone extended along the border between U.S. and Canada in December. Baroclinic zones maximize and northern one extends to Greenland in January. After this month, the baroclinic zones weaken with month. These results reveal that in the North Atlantic region the lower baroclinicity is more dominant than the northwestern Pacific region. Lackmann et al.

(1996) reported on planetary- and synoptic-scale characteristics of explosive cyclones over the northwestern Atlantic Ocean. When explosive cyclogenesis occurred over the northwestern Atlantic Ocean, an upper trough, associated with strong vorticity maximum and a jet streak, extended from eastern Canada to the eastern U.S., and a cold air anomaly was located over the eastern half of the North America continent in the lower level. This situation resembles to the atmospheric environment of OJ cyclones and averaged field in January. Sanders and Davis (1988) suggested that, when ST ( $> 1.8$  Bergeron) explosive cyclones developed over the northwestern Atlantic Ocean, a colder air mass spread over the north American continent in the lower level, a cold air anomaly dominated in the middle latitude over the North Atlantic region and a warm air anomaly was located in the polar latitude. Thus stronger westerly thermal wind appeared over the explosive cyclogenesis region. In contrast, WE ( $< 1.3$  Bergeron) explosive cyclones occurred with weaker cold air mass than ST cyclones, a cold air anomaly appeared in polar latitudes, warm anomaly was located in the middle latitude. Therefore, thermal wind was weaker than that in ST cyclones in the cyclogenesis region. This variation looks like the similar difference between PO-L and PO-O cyclones. These previous studies and monthly averaged field reveal a possibility of cyclone track classification in the North Atlantic region, because there are some differences of larger scale environment for the explosive cyclogenesis as shown in the northwestern Pacific region. However, it may be difficult to find seasonal variation of the cyclone track because the two low-level baroclinic zones, one is located over the continent and another is located along the east coast of the continent, appeared simultaneously, and upper-level seasonal variation is ambiguous.

Cyclone structure and relative contributions of physical development processes were different in northwestern Pacific region depending on cyclone track, and affected to the maximum deepening rate. Wang and Rogers (2001) classified the explosive cyclones developed over the northwestern Atlantic Ocean (NWA) and over the northeastern Atlantic Ocean (NEA), and then analyzed cyclone structures. For configuration of an upper jet streak and a surface cyclone center, the NWA cyclones are resemble to the PO-O cyclones which developed under polarward

exit of jet streak, while the NWA cyclones have strong baroclinicity at lower level that is an feature of OJ cyclones. Most of case studies and numerical simulations of explosive cyclones over the northwestern Atlantic Ocean suggested that latent heat release was significantly important during rapidly developing (Gyakum 1983a,b; Anthes et al. 1983; Huo et al. 1995; Rausch and Smith 1996; Thorsteinsson et al. 1999; Wernli et al. 2002), which is the same characteristic as the PO-O cyclones. However, as Kuo and Low-Nam (1990) suggested, relative contributions of several physical development processes were different case by case in the Atlantic region. For example, Rogers and Bosart (1991) reported a case study mainly developed due to the contribution of the upper-level trough, like OJ cyclones. The case developed over north of the Gulf Stream where SST was colder. On the other hand, Giordani and Caniaux (2001) reported that a cyclone, which observed during FASTEX IOP 15, explosively developed due to interaction between an occluded front and a local SST gradient.

Present study and previous studies suggest that cyclone structure and contribution rate of cyclogenesis processes depend on the larger scale environmental condition. In the North Atlantic region, ST category cyclones are more popular than the northwestern Pacific region (Sanders and Gyakum 1980; Chen et al. 1992). The fact may also be a result from the difference of the environmental structures between two regions. Namely, cyclones may develop more rapidly due to strong baroclinicity with much moisture in the north Atlantic region, PO-O cyclones may develop more explosively due to much moisture in northwestern Pacific region and OJ cyclones, which may develop due to strong upper vorticity advection and strong baroclinicity in the small amount of moisture, tend to have weaker deepening rate.

## **7.2 Contributions to the global energy and water transportation**

Extratropical cyclones play a role to transport energy between lower and higher latitudes. Since explosive cyclones tend to become larger and deeper than non explosively developing cyclones (Gyakum et al. 1989), their contribution to energy transport may be more important. Additionally, Zhu and Newell (1994, 1998) suggested that most part of water transport in winter

may attribute to explosive cyclones and they may constitute “Atmospheric river.” Moisture and energy transports in the northwestern Pacific region by the three types of explosive cyclones are discussed in this section.

To estimate moisture transport, the moisture budget analysis was conducted. The moisture budget is computed by considering the local tendency of the amount of moisture in the air column above the ground as a water vapor budget of the precipitation and evaporation on the ground (P–E), where P is the amount of precipitation and E is the amount of evaporation. The moisture budget may be written as:

$$P - E = -\frac{\partial}{\partial t} \left( \frac{1}{g} \int_{p_t}^{p_b} q dp \right) - \frac{1}{g} \int_{p_t}^{p_b} \nabla \cdot (q\mathbf{v}) dp, \quad (17)$$

where  $g$  is gravitational acceleration,  $q$  is specific humidity,  $p$  is pressure,  $p_t$  is the upper boundary of the air column (=300 hPa),  $p_b$  is sea-level pressure,  $\mathbf{v}$  is the horizontal wind vector.

Figure 48 shows fixed cyclone center composite charts for moderate explosive cyclones where moisture analysis was completed at the maximum deepening rate. When OJ cyclones developed explosively, the vertically integrated horizontal vapor flux was larger over the southeastern quadrant, which corresponds to the northwestern Pacific Ocean. The amount of moisture advection into the cyclone center was relatively small. As a result, the amount of P–E was smaller, and latent heat release may not have contributed strongly to cyclone development. In the case of PO-L cyclones, water vapor was transported from the south and southwest toward the northeast, and converged along the eastern flank of the cyclone center, which corresponded to a warm front. As PO-L cyclones had a zonally stretched strong upper- and mid-level jet, moisture tended to be transported toward the east of the cyclone. Thus the moisture convergence zone was spread over eastward and the net budget was larger than that of OJ cyclones but smaller than that of PO-O cyclones. For PO-O cyclones, most of the southern part of the cyclone contained precipitable water over 20mm. Stronger vapor flux toward the cyclone center existed, and the amount of P–E was greatest. Case studies of cyclones over the northwestern Pacific Ocean and the East China Sea (Chen et al. 1985; Chang et al. 1987; Liou and Elsberry 1987) suggested that latent heat release at lower levels is an important factor for the rapid cyclogenesis.

It is also important for global energy and water transport to understand water vapor transportation route. To clarify water vapor transport path for each type of the explosive cyclone and consider net budget during cyclone lifetime, a geographically fixed composite analysis was conducted for values averaged between formation and minimum central sea-level pressure. Composite charts of vertical integrated vapor flux and its divergence are shown in Fig. 49. When OJ cyclones occurred, divergence zone was located over the Yellow Sea and Sea of Japan, from which vapor flux directed northeastward over Japan and converged south of the Kamchatka peninsula and the Bering Sea. For PO-L cyclones, divergence centered over the south coast of Japan, vapor flux directed eastward from the East China Sea and converged over northeastern Pacific Ocean. For PO-O cyclones, divergence zone spread over the Sea of Japan and tropical region, and larger convergence occurred over the central North Pacific Ocean.

These results reveal that explosive cyclones transported large amount of water from around Japan to Kamchatka and Bering Sea for OJ cyclones, to northeastern Pacific Ocean for PO-L cyclones, and to center of the North Pacific Ocean for PO-O cyclones. Chen et al. (1995) analyzed global water vapor transport, suggested that the area around south of Japan was large moisture source in winter. Moisture budget analysis suggest that explosive cyclones may contribute to the divergence of water vapor over the northwestern Pacific region. Unfortunately, the moisture budget analysis cannot estimate precipitation and evaporation because GANAL data set does not contain precipitation amount and surface vertical flux data. To estimate precipitation, the average using positive value of  $P-E$  can be considered as the amount of precipitation. Figure 50 shows composite chart of average using positive value of  $P-E$ . Amount of precipitation was much over offshore east of Japan for OJ cyclones. Precipitation amount concentrated along  $40^{\circ}\text{N}$  line over the northern Pacific Ocean for PO-L cyclones. Precipitation zone extended from just southeast of Japan to the central northern Pacific Ocean for PO-O cyclones. Compared with Fig. 49, the amount of precipitation over the northwestern Pacific Ocean was larger. Since the net budget was approximately zero over the region, precipitation by cyclones may evaporate into dry air mass behind cyclones.

As discussed in section 5 and 6, latent heat release helps the rapid deepening of cyclones, and a tendency existed for cyclones with larger maximum deepening rates to have larger contributions from latent heat release. The distribution of moisture budgets was influenced by environmental wind and moisture, and contributed to cyclone deepening. As the OJ cyclones traveled over land at high latitudes, moved over the sea and quickly developed, they exhibited a smaller amount of P–E, the smaller contribution of the latent heat release for the rapid deepening. The PO-O cyclones were born at relatively lower latitudes over the ocean, traveled toward the north and developed in the higher latitudes, therefore, exhibiting a larger amount of P–E and larger contributions from latent heat release to development. Additionally, intensification of cyclone by latent heat release leads to increase of moisture transport. Explosively developing cyclones not only transport pre-existed moisture in atmosphere but also promote vertical transport from the sea surface to the atmosphere by horizontal advection of dry air from the Asian continent to the ocean. Through these processes, the cyclones achieved large transport of moisture, which may contribute to the global energy circulation.

## 8 Conclusions

To better understand explosively developing extratropical cyclones in the northwestern Pacific region, formation and maximum deepening positions, tracks, and atmospheric conditions were analyzed using GANAL data set provided by JMA. Explosively deepening cyclones were classified into three types by birth locations and rapid development locations. OJ cyclones appeared over the east Asian continent and developed over the Sea of Okhotsk and the Sea of Japan. PO-L cyclones were also formed over the eastern Asian continent, traveled eastward and developed over the northwestern Pacific Ocean. PO-O cyclones were formed over the ocean near the East China Sea, traveled northeastward and developed over the northwestern Pacific Ocean at higher latitudes. During five cold seasons, from 1994 to 1999, there were 224 cases of explosive cyclones in total, with approximately 49% (110 cases) of them PO-O cyclones, PO-L cyclones accounted for 22% (50 cases) and OJ cyclones accounted for 19% (42 cases). A relationship between the maximum deepening rate and cyclone types was found. PO-O cyclones had the strongest deepening rate, followed by PO-L cyclones, with OJ cyclones the weakest. OJ cyclones frequently occurred in late autumn (November), PO-L cyclones occurred in early and late winter (December and February), and PO-O cyclones occurred in mid-winter (January).

Larger scale atmospheric conditions and cyclone structures were examined using composite analyses. As a summary of these analyses, schematic illustrations of explosive developing cyclones are shown in Fig. 51. OJ cyclones develop in the presence of a relatively small upper-level trough over the northeastern China with a short jet streak. As the cold air mass outbreak is still weak, a baroclinic zone forms over the Sea of Japan and the Sea of Okhotsk where OJ cyclones develop explosively. Analyses of the mechanism of development reveal large contributions from low-level temperature advection and upper-level vorticity advection, and smaller contributions from latent heat release. The magnitude of the deepening rate is the smallest of the three. PO-L cyclones develop in early and late winter, and have a zonally stretched jet stream over southern Japan and the northwestern Pacific Ocean in the upper level. A cold air mass forms over the northern Asian continent, extends over the Pacific Ocean, and a baroclinic

zone forms over the southern part of Japan toward east of Japan, where PO-L cyclones develop. PO-L cyclones are mainly developed by temperature advection. PO-O cyclones develop in mid-winter. A cold air mass over the Asian continent extends largely over the northwestern Pacific Ocean with a long fetch. A strong jet streak associated with the upper-level short-wave trough is present west of the cyclone. A jet stream exit can be seen near the cyclone center. Upper-level forcing induces a strong updraft near the cyclone center and a large amount of latent heat release intensified the updraft. The latent heat release is an important contributor to the explosive development and results in a stronger deepening rate.

Numerical experiments were conducted to understand the effect of latent heat release on cyclone development. The PO-O case hardly develop without latent heat release, while the other cases somewhat developed, although deepening rate decreased. The structures of PO-O case were drastically modified without latent heat release and that of other cases did not change so much.

Comparison with explosively developing cyclones in the North Atlantic region suggested that seasonal variations of cyclone tracks may be an unique characteristic in the northwestern Pacific region. Moisture budget analysis suggested that explosive cyclones in the northwestern Pacific region transported water vapor from the south of Japan to the Kamchatka and Bering Sea by OJ cyclones, to the northeastern Pacific region by PO-L cyclones, and to the central northern Pacific region by PO-O cyclones, respectively.

We have reported statistical and composite analyses on the explosively developing cyclones in the northwestern Pacific region in the present study, and have suggested that tracks, structures and developing mechanisms changed to reflect the presence and extension of a cold air mass over the continent and moisture distribution over the ocean. Extreme case studies using numerical simulations have also suggested the characteristics of the detailed structure of cyclones and role of latent heat release. Extratropical cyclones also play an important role in energy and water exchange between lower and higher latitudes on a global scale. Therefore, cyclone activities impact regional climate, whereas global climate affects cyclone activities. Chen et al. (1992)

pointed out positive correlation between El Nino and the frequency of explosive cyclone over the northwestern Pacific region, and some studies of global warming experiments using general circulation models suggested that the number of stronger extratropical cyclones may increase if the amount of CO<sub>2</sub> increases (Geng and Sugi 2003). Clarifying the interaction between cyclone activity and the climate may be one of the most important topics in future research works.

## **Acknowledgments**

The author would like to express his thanks to Dr. Y. Asuma, Division of Earth and Planetary Sciences, Graduate School of Science, Hokkaido University for his continuous encouragement and invaluable suggestions during present study. He would also like to express his thanks to Prof. Y.-Y. Hayashi and Prof. S. Watanabe, Division of Earth and Planetary Sciences, Graduate School of Science, Hokkaido University, and Prof. K. Yamazaki, Graduate School of Environmental Earth Science, Hokkaido University, for their inspiring suggestions and fruitful discussions. Thanks are extended to Prof. K. Kikuchi, Department of Biological Environment, Faculty of Bioresource Sciences, Akita Prefectural University and Prof. H. Uyeda, Hydrospheric Atmospheric Research Center, Nagoya University, for paying continuous attention to this study. The author wishes to express his gratitude to Mr. M. Kato, Division of Earth and Planetary Sciences, Graduate School of Science, Hokkaido University for his technical assistance of the analyses and also encouraging author's research work.

Several of the figures were drafted by GMT (the Generic Mapping Tools) data processing and display software package and several numerical calculations were helped by GrADS (the Grid Analysis and Display System).

## References

- Anthes, R. A., Y.-H. Kuo, and J. R. Gyakum, 1983: Numerical simulations of a case of explosive marine cyclogenesis. *Mon. Wea. Rev.*, **111**, 1174–1188.
- Blender, R., K. Fraedrich, and F. Lunkeit, 1997: Identification of cyclone-track regimes in the North Atlantic. *Quart. J. R. Meteor. Soc.*, **123**, 727–741.
- Bullock, T. A., and J. R. Gyakum, 1993: A diagnostic study of cyclogenesis in the western North Pacific Ocean. *Mon. Wea. Rev.*, **121**, 65–75.
- Chang, C.-B., D. J. Perkey, and W.-D. Chen, 1987: Observed dynamic structure of an intense oceanic cyclone. *Mon. Wea. Rev.*, **115**, 1127–1139.
- Chen, S.-J., and L. Dell’Osso, 1987: A numerical case study of east Asian coastal cyclogenesis. *Mon. Wea. Rev.*, **115**, 477–487.
- Chen, T.-C., C.-B. Chang, and D. J. Perkey, 1985: Synoptic study of a medium-scale oceanic cyclone during AMTEX ’75. *Mon. Wea. Rev.*, **113**, 349–361.
- Chen, S.-J., Y.-H. Kuo, P.-Z. Zhang, and Q.-F. Bai, 1991: Synoptic climatology of cyclogenesis over east Asia, 1958-1987. *Mon. Wea. Rev.*, **119**, 1407–1418.
- , ———, ———, and ———, 1992: Climatology of explosive cyclones off the east Asian coast. *Mon. Wea. Rev.*, **120**, 3029–3035.
- Chen, T.-C., J.-M. Chen, and J. Pfaendtner, 1995: Low-frequency variations in the atmospheric branch of the global hydrological cycle. *J. Climate*, **8**, 92–107.
- Dudhia, J., 1989: Numerical study of convection observed during the winter monsoon experiment using a mesoscale two-dimensional model. *J. Atmos. Sci.*, **46**, 3077–3107.
- Edmon, H. J., Jr., and D. G. Vincent, 1976: An application of two tropical parameterization schemes of convective latent heat release in middle latitudes. *Mon. Wea. Rev.*, **104**, 1141–1153.
- Geng, Q., and M. Sugi, 2001: Variability of the North Atlantic cyclone activity in winter analyzed from NCEP-NCAR reanalysis data. *J. Climate*, **14**, 3863–3873.
- , and ———, 2003: Possible change of extratropical cyclone activity due to enhanced greenhouse gases and sulfate aerosols—study with a high-resolution AGCM. *J. Climate*, **16**, 2262–

2274.

- Giordani, H., and G. Caniaux, 2001: Sensitivity of cyclogenesis to sea surface temperature in the northwestern Atlantic. *Mon. Wea. Rev.*, **129**, 1273–1295.
- Grell, G. A., 1993: Prognostic evaluation of assumptions used by cumulus parameterizations. *Mon. Wea. Rev.*, **121**, 764–787.
- , J. Dudhia, and D. R. Stauffer, 1995: A description of the fifth-generation Penn State/NCAR Mesoscale Model (MM5). NCAR Tech. Note NCAR/TN-398+STR, 122pp.
- Gyakum, J. R., 1983a: On the evolution of the QE II storm. I: Synoptic aspects. *Mon. Wea. Rev.*, **111**, 1137–1155.
- , 1983b: On the evolution of the QE II storm. II: Dynamic and thermodynamic structure. *Mon. Wea. Rev.*, **111**, 1156–1173.
- , and R. E. Danielson, 2000: Analysis of meteorological precursors to ordinary and explosive cyclogenesis in the western North Pacific. *Mon. Wea. Rev.*, **128**, 851–863.
- , J. R. Anderson, R. H. Grumm, and E. L. Gruner, 1989: North Pacific cold-season surface cyclone activity: 1975-1983. *Mon. Wea. Rev.*, **117**, 1141–1155.
- Hadlock, R., and C. W. Kreitzberg, 1988: The Experiment on Rapidly Intensifying Cyclones over the Atlantic (ERICA) field study: Objectives and plans. *Bull. Amer. Meteor. Soc.*, **69**, 1309–1320.
- Hoskins, B. J., and P. J. Valdes, 1990: On the existence of storm-tracks. *J. Atmos. Sci.*, **47**, 1854–1865.
- Huo, Z., D.-L. Zhang, and J. Gyakum, 1995: A diagnostic analysis of the Superstorm of March 1993. *Mon. Wea. Rev.*, **123**, 1740–1761.
- Joly, A., D. Jorgensen, M. A. Shapiro, A. Thorpe, P. Bessemoulin, K. A. Browning, J.-P. Cammas, J.-P. Chalon, S. A. Clough, K. A. Emanuel, L. Eymard, R. Gall, P. H. Hildebrand, R. H. Langland, Y. Lemaitre, P. Lynch, J. A. Moore, P. O. G. Persson, C. Snyder, and R. M. Wakimoto, 1997: The Fronts and Atlantic Storm-Track Experiment (FASTEX): Scientific objectives and experimental design. *Bull. Amer. Meteor. Soc.*, **78**, 1917–1940.
- Kelly, R. W. P., J. R. Gyakum, D.-L. Zhang, and P. J. Roebber, 1994: A diagnostic study of the

- early phases of sixteen western North-Pacific cyclones. *J. Meteor. Soc. Japan*, **72**, 515–530.
- Krishnamurti, T. N., and W. J. Moxim, 1971: On parameterization of convective and nonconvective latent heat release. *J. Appl. Meteor.*, **10**, 3–13.
- Kuo, H. L., 1965: On formation and intensification of tropical cyclones through latent heat release by cumulus convection. *J. Atmos. Sci.*, **22**, 40–63.
- , 1974: Further studies of the parameterization of the influence of cumulus convection on a large-scale flow. *J. Atmos. Sci.*, **31**, 1232–1240.
- Kuo, Y.-H., and S. Low-Nam, 1990: Prediction of nine explosive cyclones over the western Atlantic Ocean with a regional model. *Mon. Wea. Rev.*, **118**, 3–25.
- Lackmann, G. M., L. F. Bosart, and D. Keyser, 1996: Planetary- and synoptic-scale characteristics of explosive wintertime cyclogenesis over the western North Atlantic Ocean. *Mon. Wea. Rev.*, **124**, 2672–2702.
- Lin, S. C., and P. J. Smith, 1979: Diabatic heating and generation of available potential energy in a tornado-producing extratropical cyclone. *Mon. Wea. Rev.*, **107**, 1169–1183.
- Lindzen, R. S., and B. Farrell, 1980: A simple approximate result for the maximum growth rate of baroclinic instabilities. *J. Atmos. Sci.*, **37**, 1648–1654.
- Liou, C.-S., and R. L. Elsberry, 1987: Heat budgets of analyses and forecasts of an explosively deepening maritime cyclone. *Mon. Wea. Rev.*, **115**, 1809–1824.
- Liu, C.-H., R. M. Wakimoto, and F. Roux, 1997: Observations of mesoscale circulations within extratropical cyclones over the North Atlantic Ocean during ERICA. *Mon. Wea. Rev.*, **125**, 341–364.
- Lupo, A. R., P. J. Smith, and P. Zwack, 1992: A diagnosis of the explosive development of two extratropical cyclones. *Mon. Wea. Rev.*, **120**, 1490–1523.
- Manobianco, J., 1989: Explosive east coast cyclogenesis over the west-central North Atlantic Ocean: A composite study derived from ECMWF operational analyses. *Mon. Wea. Rev.*, **117**, 2365–2383.
- Neiman, P. J., and M. A. Shapiro, 1993: The life cycle of an extratropical marine cyclone. Part I: Frontal-cyclone evolution and thermodynamic air-sea interaction. *Mon. Wea. Rev.*, **121**,

- 2153–2175.
- , ——, and L. S. Fedor, 1993: The life cycle of an extratropical marine cyclone. Part II: Mesoscale structure and diagnostics. *Mon. Wea. Rev.*, **121**, 2177–2199.
- Nitta, T., and J. Yamamoto, 1972: A statistical survey on frequency of the cyclogenesis of the intermediate scale disturbance near Japan, its vicinity and the southeast Asia. *J. Meteor. Soc. Japan*, **50**, 234–237.
- , and ——, 1974: On the observational characteristics of intermediate scale disturbances generated near Japan and the vicinity. *J. Meteor. Soc. Japan*, **52**, 11–31.
- O'Brien, J. J., 1970: Alternative solutions to the classical vertical velocity problem. *J. Appl. Meteor.*, **9**, 197–203.
- Paciorek, C. J., J. S. Risbey, V. Ventura, and R. D. Rosen, 2002: Multiple indices of northern hemisphere cyclone activity, winters 1949-99. *J. Climate*, **15**, 1573–1590.
- Rausch, R. L. M., and P. J. Smith, 1996: A diagnosis of a model-simulated explosively developing extratropical cyclone. *Mon. Wea. Rev.*, **124**, 875–904.
- Reisner, J. R., J. Rasmussen, and R. T. Brintjes, 1998: Explicit forecasting of supercooled liquid water in winter storm using the MM5 mesoscale model. *Quart. J. Roy. Meteor. Soc.*, **124B**, 1071–1107.
- Roebber, P. J., 1984: Statistical analysis and updated climatology of explosive cyclones. *Mon. Wea. Rev.*, **112**, 1577–1589.
- Rogers, E., and L. F. Bosart, 1991: A diagnostic study of two intense oceanic cyclones. *Mon. Wea. Rev.*, **119**, 965–996.
- Saito, N., 1977: On the structure of medium-scale depressions over the East China Sea during AMTEX'75. *J. Meteor. Soc. Japan*, **55**, 286–300.
- Sanders, F., 1986: Explosive cyclogenesis in the west-central North Atlantic Ocean, 1981-1984. Part I: Composite structure and mean behavior. *Mon. Wea. Rev.*, **114**, 1781–1794.
- , and C. A. Davis, 1988: Patterns of thickness anomaly for explosive cyclogenesis over the west-central North Atlantic Ocean. *Mon. Wea. Rev.*, **116**, 2725–2730.
- , and J. R. Gyakum, 1980: Synoptic-dynamic climatology of the “bomb”. *Mon. Wea. Rev.*,

**108**, 1589–1606.

- Schultz, D. M., D. Keyser, and L. F. Bosart, 1998: The effect of large-scale flow on low-level frontal structure and evolution in midlatitude cyclones. *Mon. Wea. Rev.*, **126**, 1767–1791.
- Shapiro, M., H. Wernli, J.-W. Bao, J. Methven, X. Zou, J. Doyle, T. Holt, E. Donall-Grell, and P. Neiman, 1999: A planetary-scale to mesoscale perspective of the life cycles of extratropical cyclones: The bridge between theory and observations. *The Life Cycles of Extratropical Cyclones*, Shapiro, M, and S. Gronas, Eds., Amer. Meteor. Soc., 139–186.
- Shapiro, R., 1970: Smoothing, filtering, and boundary effects. *Rev. Geophys. Space. Phys.*, **8**, 359–387.
- Sickmüller, M., R. Blender, and K. Fraedrich, 2000: Observed winter cyclone tracks in the northern hemisphere in re-analyzed ECMWF data. *Quart. J. R. Meteor. Soc.*, **126**, 591–620.
- Sinclair, M. R., 1997: Objective identification of cyclones and their circulation intensity, and climatology. *Wea. Forecasting*, **12**, 595–612.
- , and M. J. Revell, 2000: Classification and composite diagnosis of extratropical cyclogenesis events in the southwest Pacific. *Mon. Wea. Rev.*, **128**, 1089–1105.
- Smith, P. J., P. M. Dare, and S.-J. Lin, 1984: The impact of latent heat release on synoptic scale vertical motions and development of an extratropical cyclone system. *Mon. Wea. Rev.*, **112**, 2421–2430.
- Thorsteinsson, S., J. E. Kristjánsson, B. Røsting, V. Erlingsson, and G. F. Ulfarsson, 1999: A diagnostic study of the Flateyri avalanche cyclone, 24–26 October 1995, using potential vorticity inversion. *Mon. Wea. Rev.*, **127**, 1074–1088.
- Ueno, K., 1993: Inter-annual variability of surface cyclone track, atmospheric circulation patterns, and precipitation patterns, in winter. *J. Meteor. Soc. Japan*, **71**, 655–671.
- Vincent, D. G., G. B. Pant, and H. J. Edmon, Jr., 1977: Generation of available potential energy of an extratropical cyclone system. *Mon. Wea. Rev.*, **105**, 1252–1265.
- Wang, C.-C., and J. C. Rogers, 2001: A composite study of explosive cyclogenesis in different sectors of the North Atlantic. Part I: Cyclone structure and evolution. *Mon. Wea. Rev.*, **129**, 1481–1499.

- Wernli, H., S. Dirren, M. A. Liniger, and M. Zillig, 2002: Dynamical aspects of the life cycle of the winter storm 'Lothar'. *Quart. J. Roy. Meteor. Soc.*, **128**, 405–429.
- Zhu, Y., and R. E. Newell, 1994: Atmospheric rivers and bombs. *Geophys. Res. Lett.*, **21**, 1999–2002.
- , and ——, 1998: A proposed algorithm for moisture fluxes from atmospheric rivers. *Mon. Wea. Rev.*, **126**, 725–735.
- Zwack, P., and B. Okossi, 1986: A new method for solving the quasigeostrophic omega equation by incorporating surface pressure tendency data. *Mon. Wea. Rev.*, **114**, 655–666.

## **Tables and Figures**

Table 1. The number of explosive cyclone events.

	OJ	PO-L	PO-O	Others	Total
Strong (ST)	3	8	20	0	31
Moderate (MO)	15	24	47	6	92
Weak (WE)	24	18	43	16	101
Total	42	50	110	22	224

Table 2. Monthly frequency of explosive cyclones in each of five cold seasons from October 1994 to March 1999. (a) All explosive cyclones, (b) OJ, (c) PO-L, and (d) PO-O cyclones.

(a) ALL

Year	Oct	Nov	Dec	Jan	Feb	Mar	Total
94/95	1	7	9	9	5	5	36
95/96	4	4	9	8	9	8	42
96/97	4	8	8	9	7	5	41
97/98	2	5	9	12	9	6	43
98/99	3	7	7	8	9	6	40
Total	14	31	42	46	39	30	202

(b) OKHOTSK-JAPAN SEA

Year	Oct	Nov	Dec	Jan	Feb	Mar	Total
94/95	1	4	1	1	0	2	9
95/96	1	4	2	2	3	0	12
96/97	2	2	2	3	0	2	11
97/98	1	2	0	1	1	0	5
98/99	0	2	1	0	1	1	5
Total	5	14	6	7	5	5	42

(c) PACIFIC OCEAN-LAND

Year	Oct	Nov	Dec	Jan	Feb	Mar	Total
94/95	0	1	4	2	1	1	9
95/96	2	0	2	1	1	4	10
96/97	0	1	1	0	2	2	6
97/98	1	2	3	4	4	2	16
98/99	0	2	2	1	3	1	9
Total	3	6	12	8	11	10	50

(d) PACIFIC OCEAN-OCEAN

Year	Oct	Nov	Dec	Jan	Feb	Mar	Total
94/95	0	2	4	6	4	2	18
95/96	1	0	5	5	5	4	20
96/97	2	5	5	6	5	1	24
97/98	0	1	6	7	4	4	22
98/99	3	3	4	7	5	4	26
Total	6	11	24	31	23	15	110

Table 3. Maximum deepening rate (unit of Bergeron) at  $T = 24$  h of typical cases for GANAL analysis, CNTL run, and DRY run.

Type	Maximum deepening rate		
	GANAL	CNTL	DRY
OJ	1.84	1.55	0.97
PO-L	2.54	1.24	0.72
PO-O	2.96	2.38	0.71

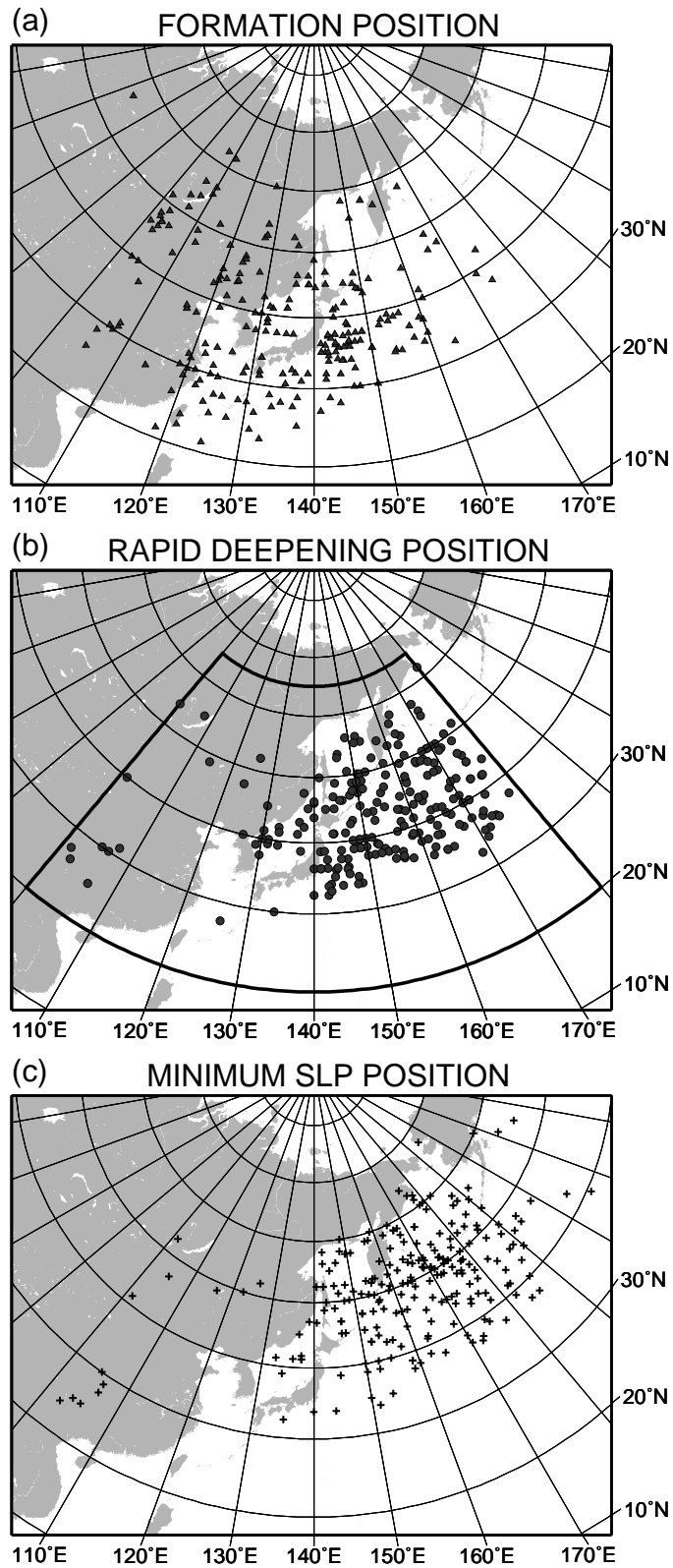


Figure 1. Geographic distributions of (a) formation, (b) maximum deepening rate and (c) minimum center sea level pressure. The outlined region in (b) shows the analysis area.

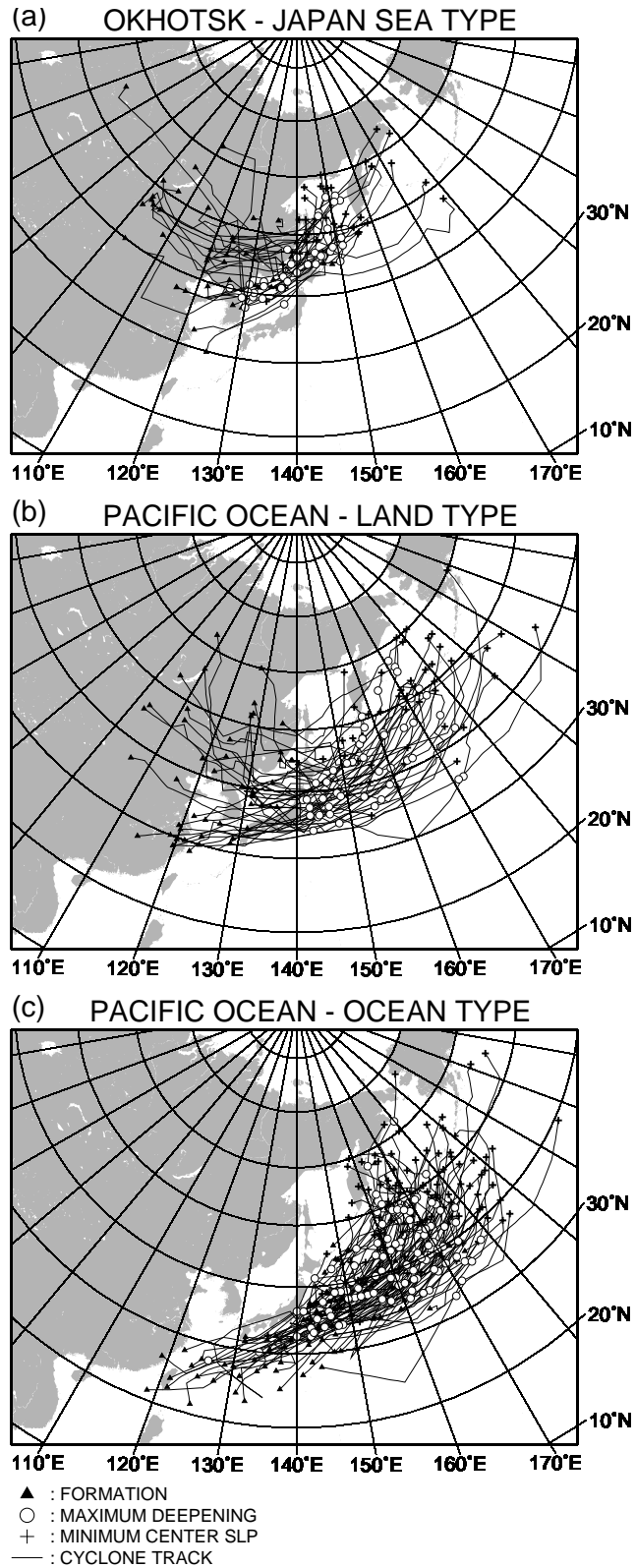


Figure 2. Cyclone tracks of (a) Okhotsk-Japan Sea (OJ), (b) Pacific Ocean-Land (PO-L) and (c) Pacific Ocean-Ocean (PO-O) cyclones. Triangles show positions of formation, circles show positions of maximum deepening and crosses show positions of minimum center sea level pressure.

## DEEPENING RATE FREQUENCY

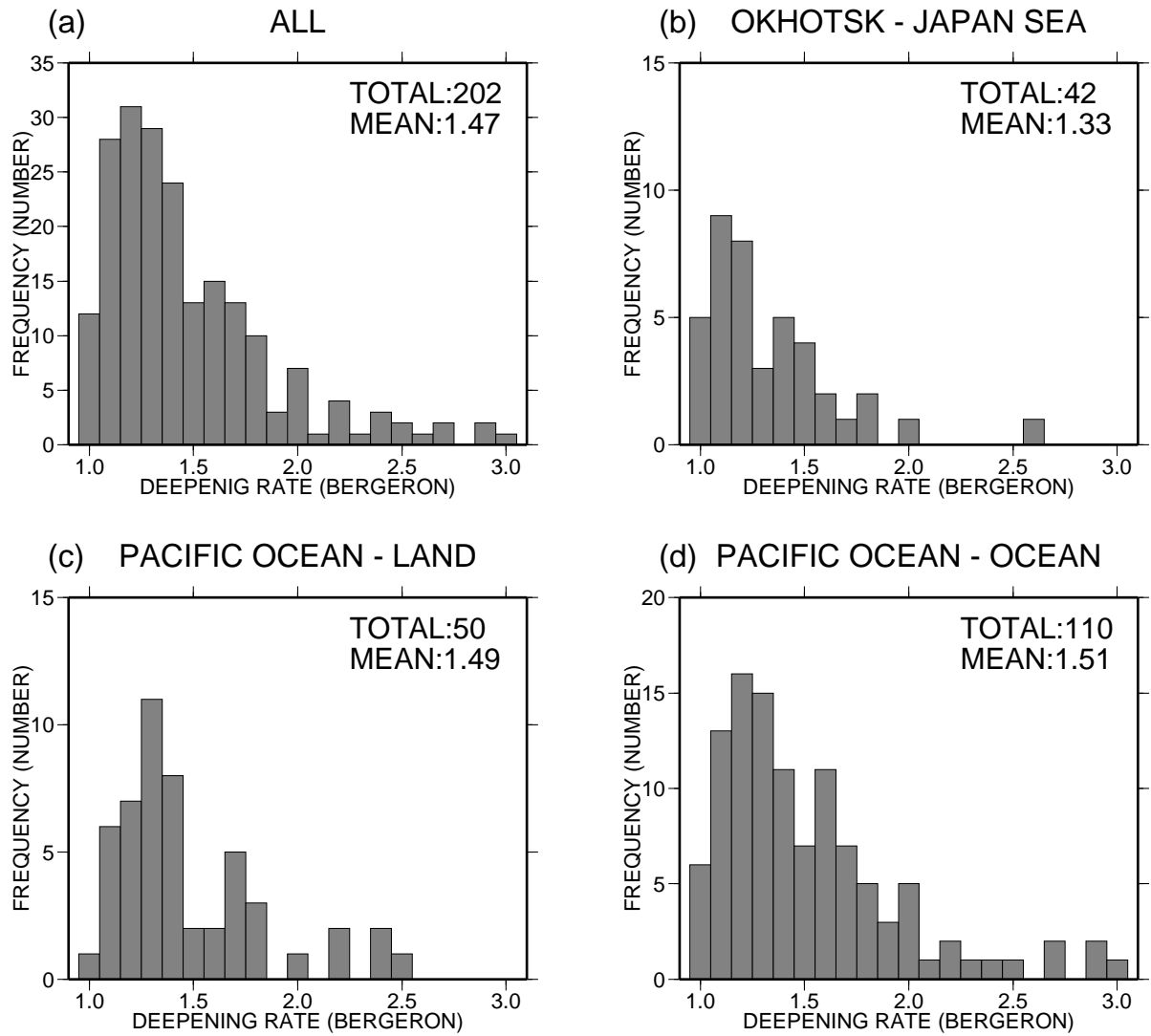


Figure 3. Maximum deepening rate histograms. (a) All explosively developing cyclones, (b) OJ, (c) PO-L, and (d) PO-O cyclones.

## MONTHLY FREQUENCY

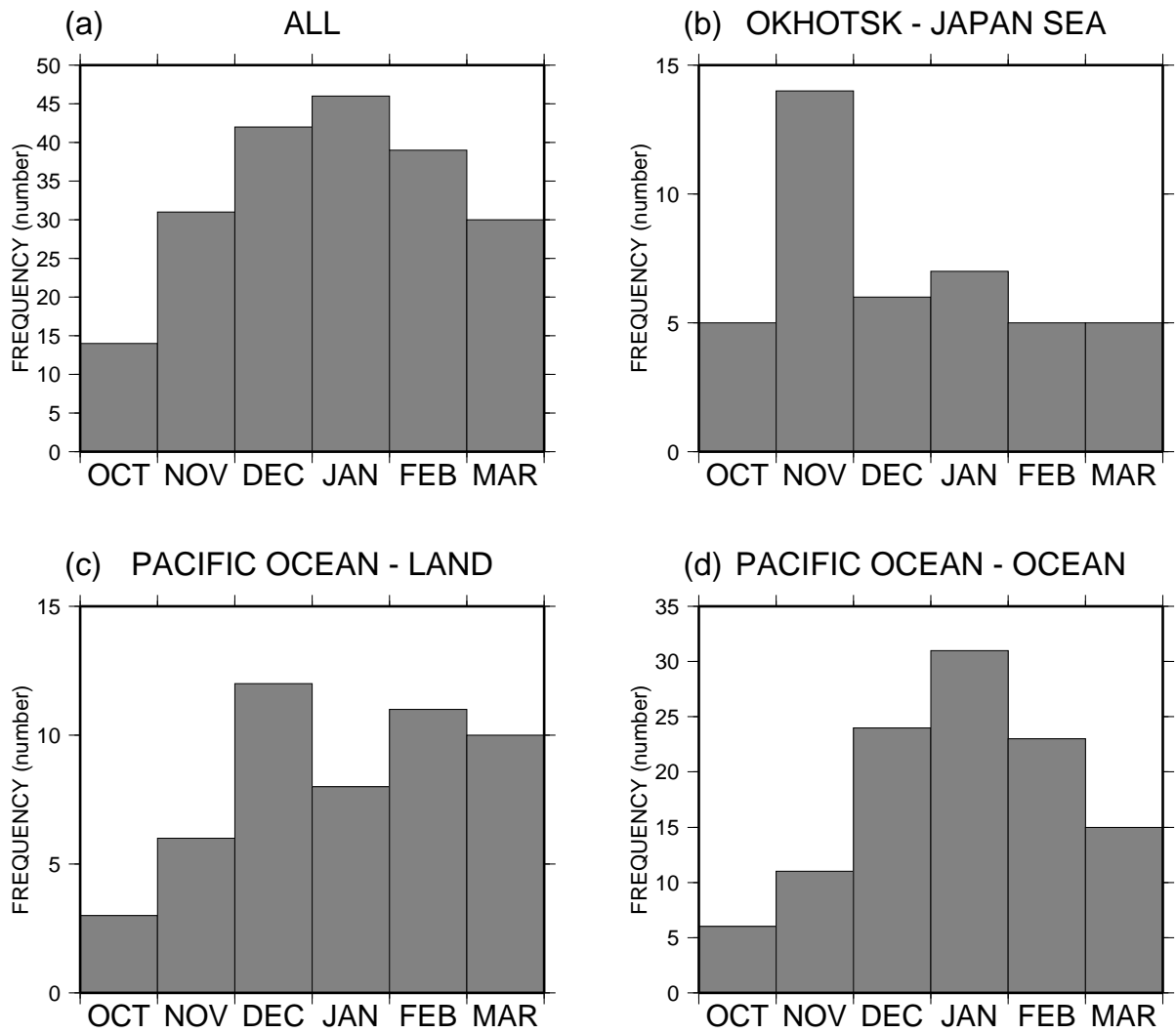


Figure 4. Monthly frequency of explosive cyclones. (a) All explosive cyclones, (b) OJ, (c) PO-L, and (d) PO-O cyclones.

# OKHOTSK - JAPAN SEA

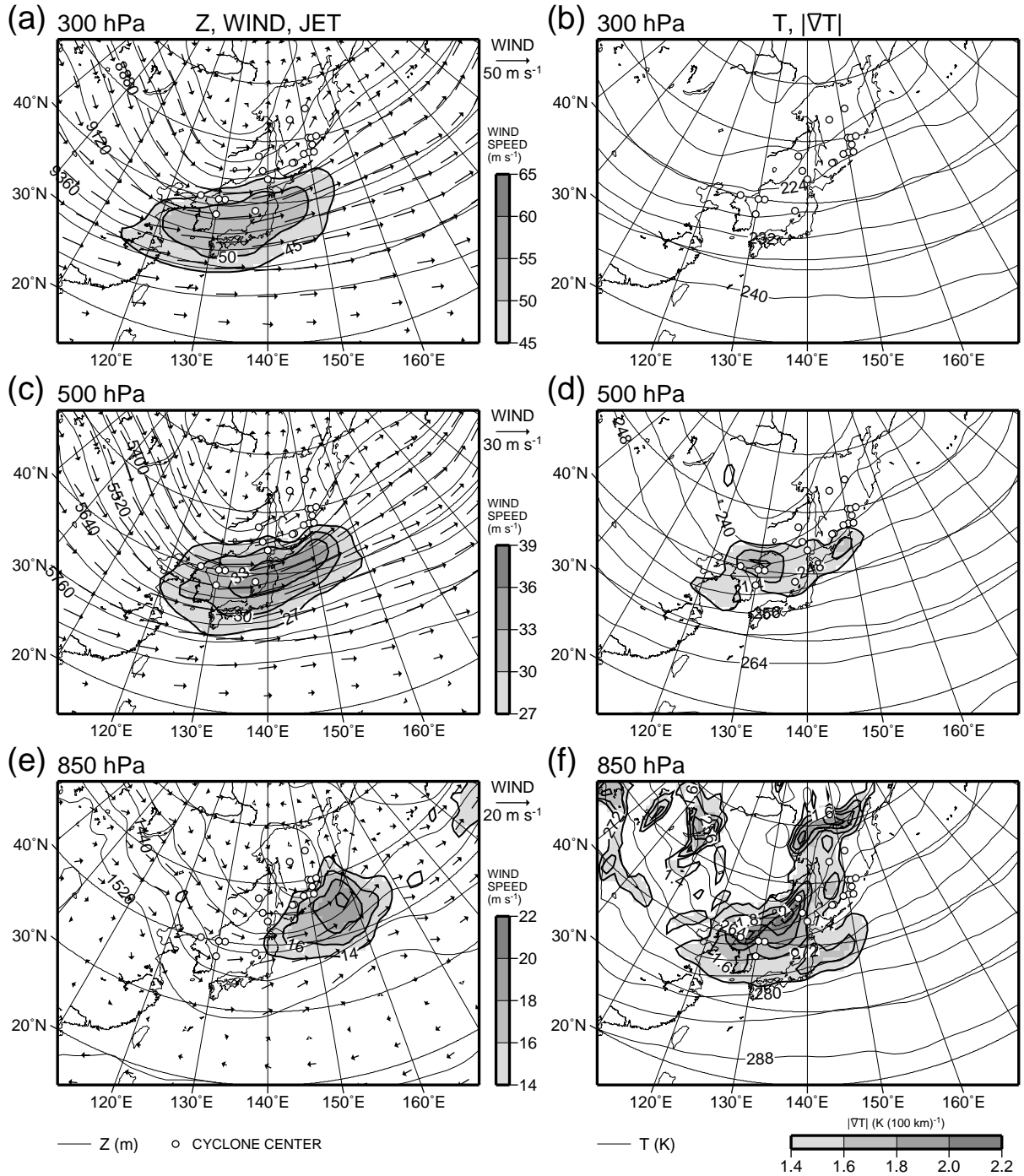


Figure 5. Composite charts for OJ cyclones at maximum deepening rate. In left column, the geopotential height (thin solid line, unit of m, contour intervals are 120 m at 300 hPa, 60 m at 500 hPa and 40 m at 850 hPa), the horizontal wind vector (arrow), and wind velocity (bold solid line and shade) (a) at 300 hPa; (c) 500 hPa; and (e) 850 hPa are shown. In right column, the temperature (thin solid line, unit of K, contour intervals are 4 K) and the horizontal temperature gradient (bold solid line and shade) (b) at 300 hPa, (d) 500 hPa, and (f) 850 hPa are shown. Circles show cyclone centers.

# PACIFIC OCEAN - LAND

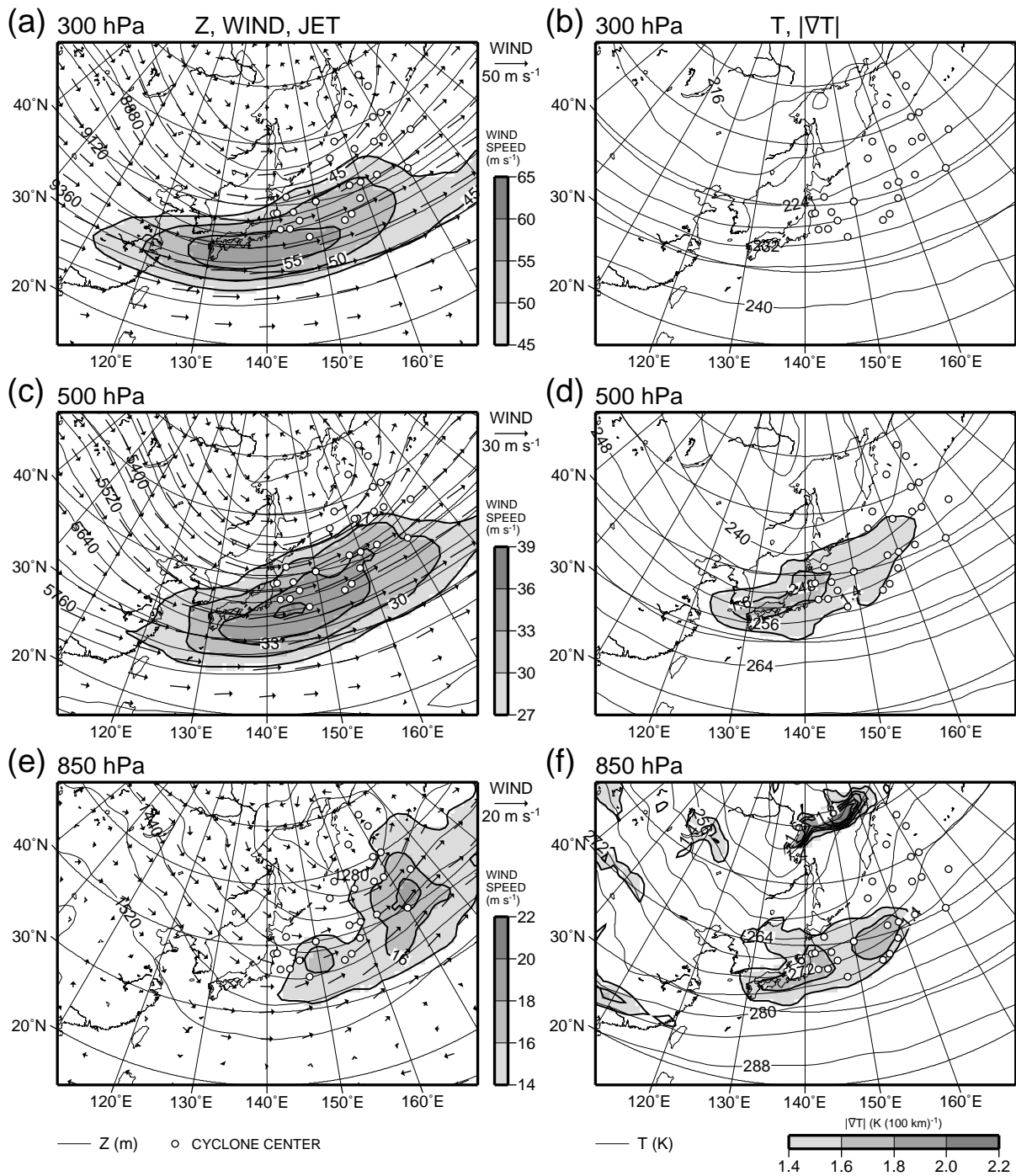


Figure 6. Same as Fig. 5, but for PO-L cyclones.

# PACIFIC OCEAN - OCEAN

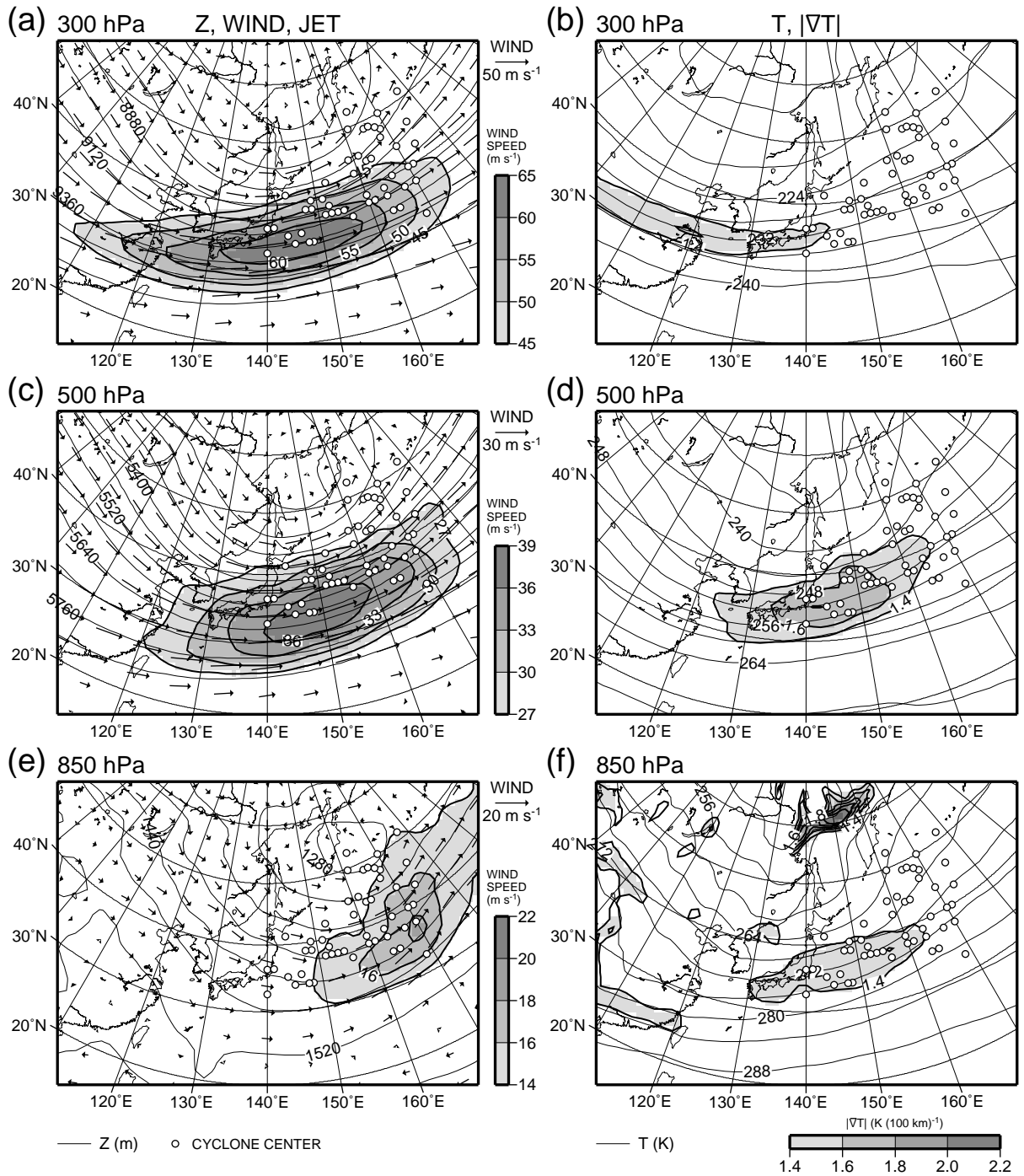


Figure 7. Same as Fig. 5, but for PO-O cyclones

## DIFFERENCE FIELD (PO-L - PO-O)

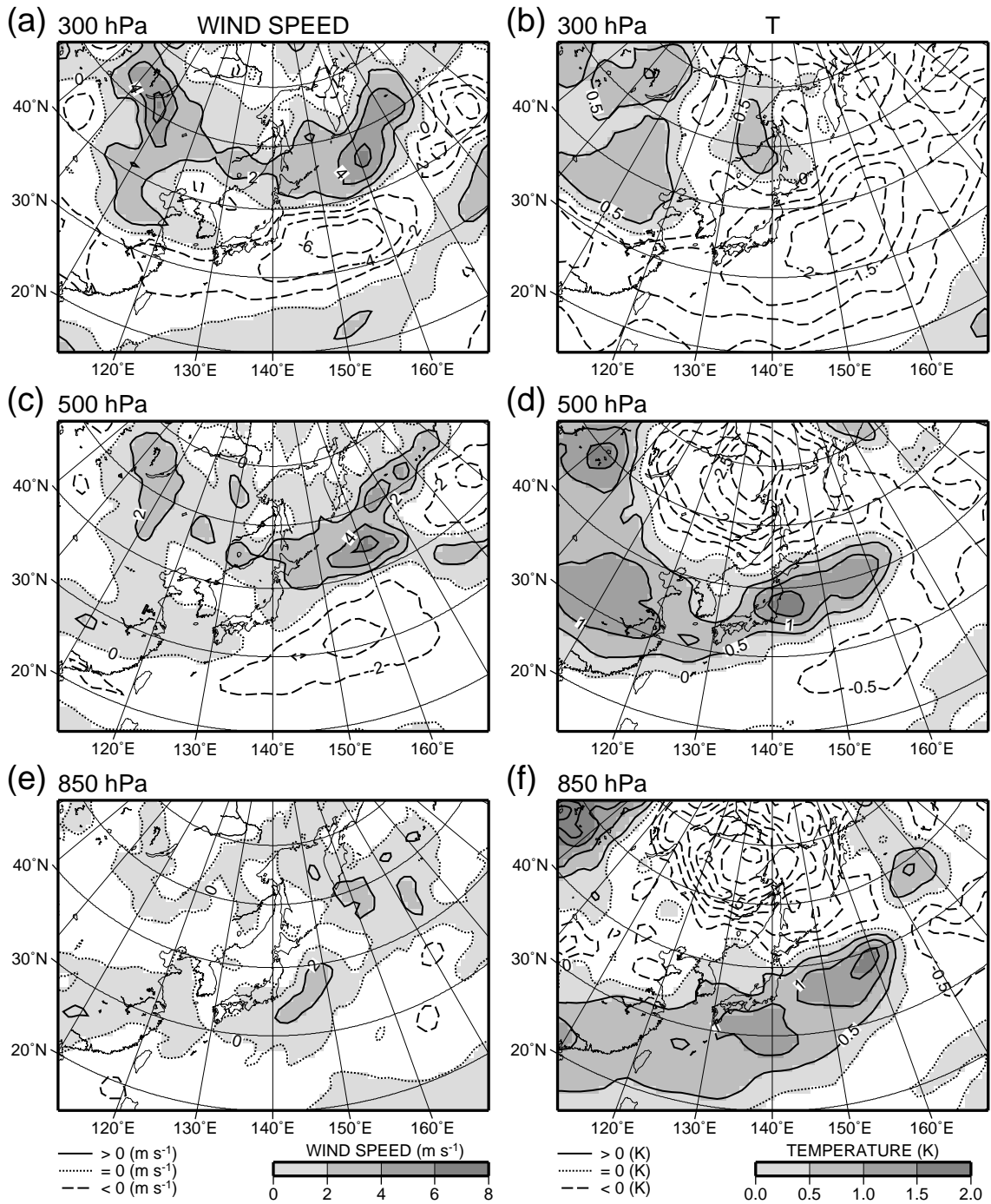


Figure 8. The difference fields between PO-L cyclones and PO-O cyclones (PO-L field minus PO-O field). In left column, the wind velocity (thin solid lines and shadings show positive, thin broken lines show negative and dotted line shows zero): (a) at 300 hPa; (c) 500 hPa; and (e) 850 hPa. In right column, the temperature (thin solid lines and shadings show positive, thin broken lines show negative and dotted line shows zero) (b) at 300 hPa, (d) 500 hPa and (f) 850 hPa.

MONTHLY AVERAGED FIELDS IN THE NORTHWESTERN PACIFIC REGION  
300 hPa Z,  $\zeta$

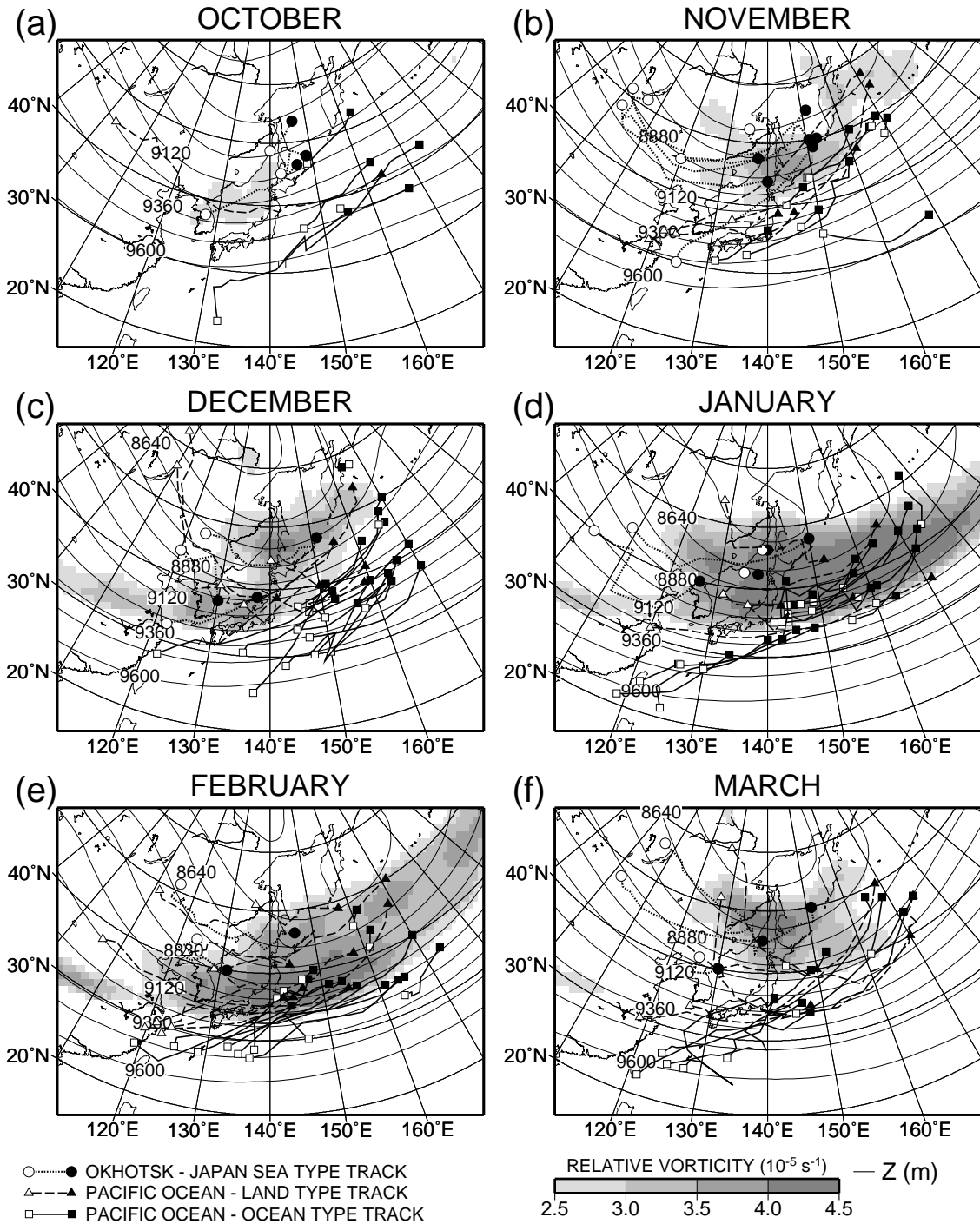


Figure 9. Monthly average from October 1996 to March 1999 at 300 hPa of geopotential heights (thin solid lines in m, contour interval is 60 m), relative vorticity (shade in  $10^{-5} \text{ s}^{-1}$ ), and cyclone tracks from formation (open symbols) to maximum deepening rate (closed symbols) for OJ (dotted line, circle), PO-L (broken line, triangle), and PO-O (bold solid line, square) cyclones in (a) October, (b) November, (c) December, (d) January, (e) February, and (f) March.

MONTHLY AVERAGED FIELDS IN THE NORTHWESTERN PACIFIC REGION  
850 hPa  $\theta$ ,  $|\nabla\theta|$

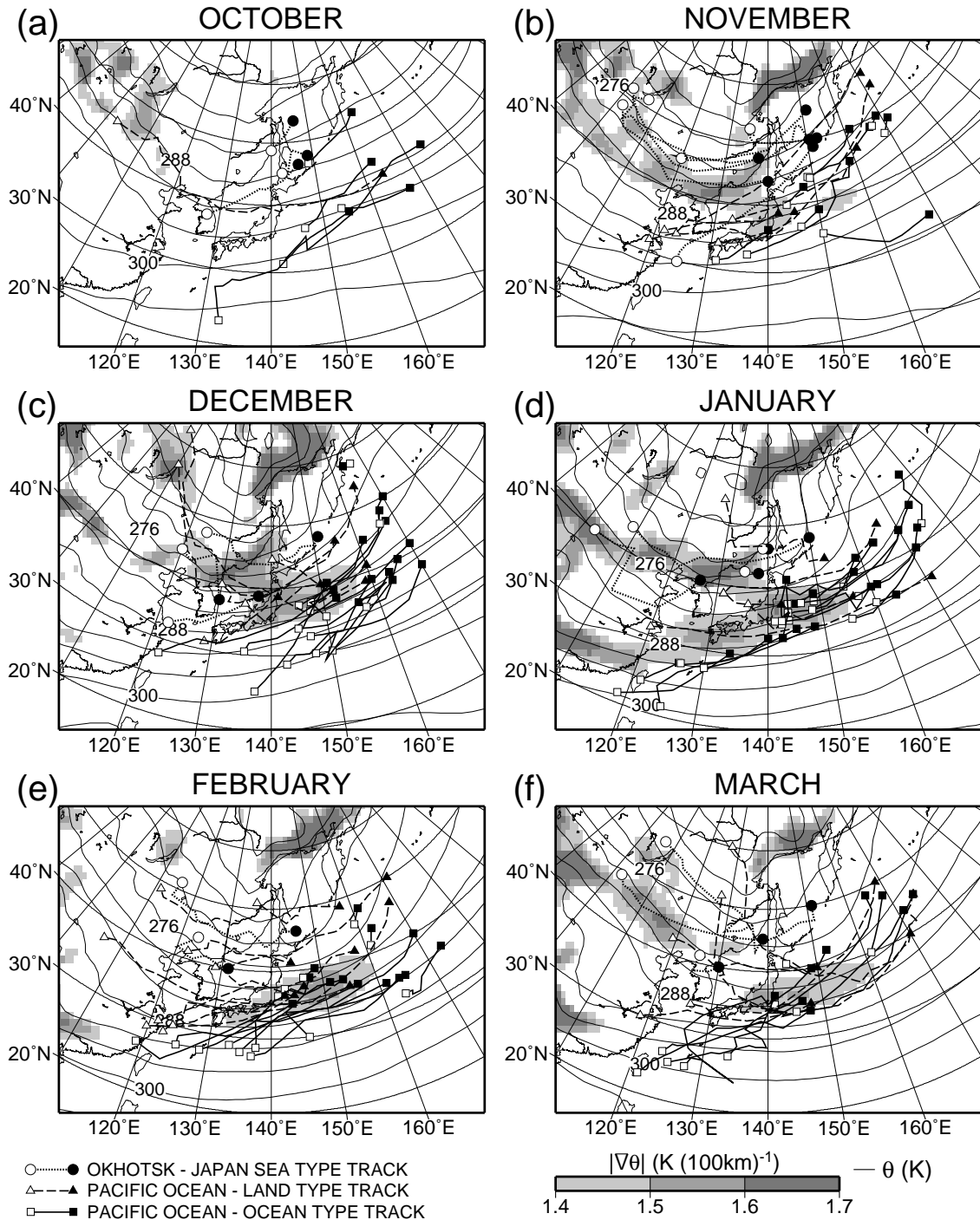


Figure 10. Monthly average from October 1996 to March 1999 at 850 hPa of potential temperature (thin solid lines in K, contour interval is 4 K), horizontal gradients (shade in K (100 km)<sup>-1</sup>), and cyclone tracks from formation (open symbols) to maximum deepening rate (closed symbols) for OJ (dotted line, circle), PO-L (broken line, triangle), and PO-O (bold solid line, square) cyclones in (a) October, (b) November, (c) December, (d) January, (e) February, and (f) March.

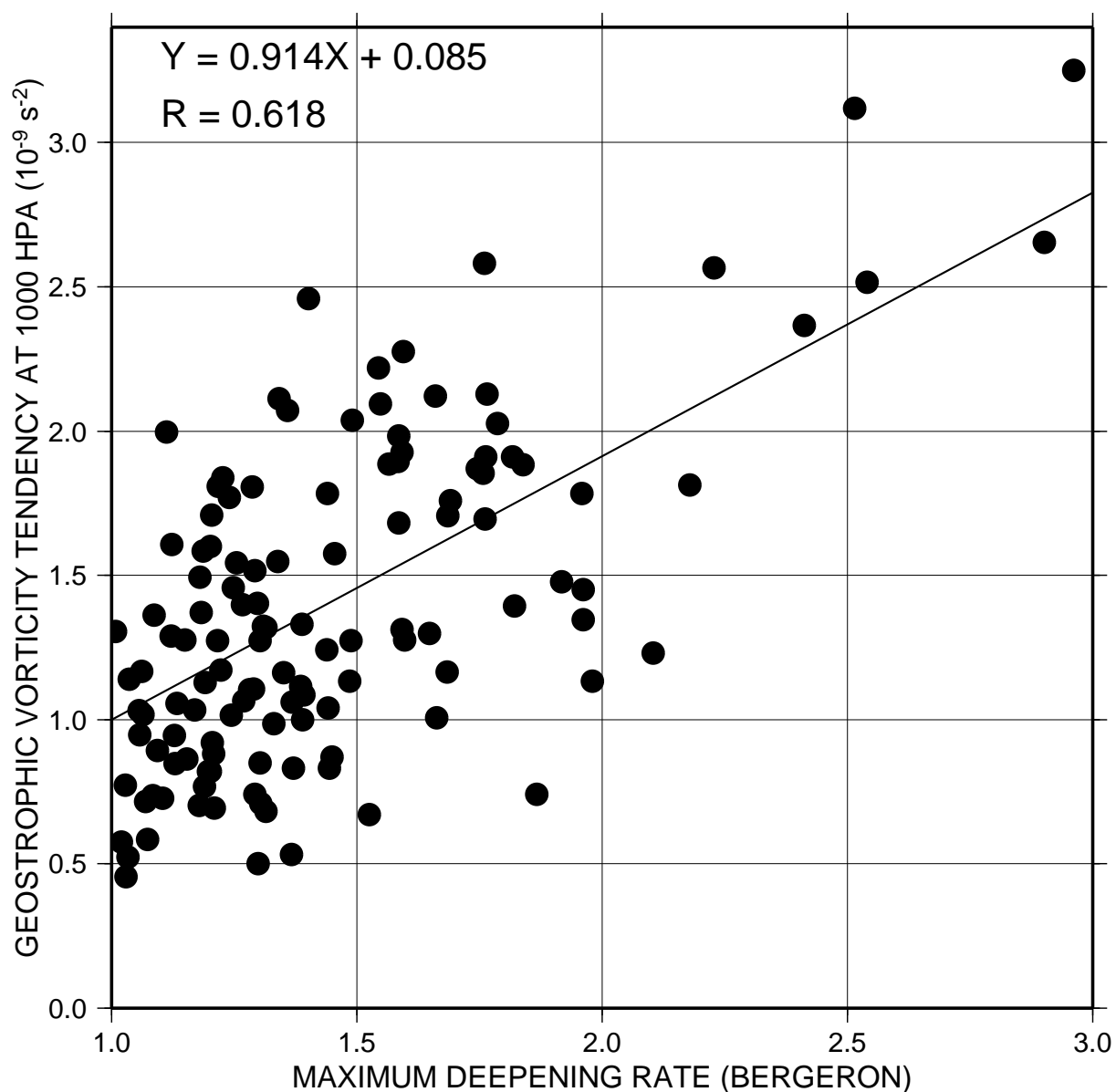


Figure 11. Scatter diagram between the cyclone maximum deepening rate (unit in Bergeron, horizontal axis) and the geostrophic relative vorticity tendency at 1000 hPa (L.H.S. in Eq. (2) by finite-difference method) averaged over an area within 500 km of the surface cyclone center 6 hours after observing the maximum deepening rate (unit in  $10^{-9} \text{ s}^{-2}$ , vertical axis). A solid line shows a regression line.

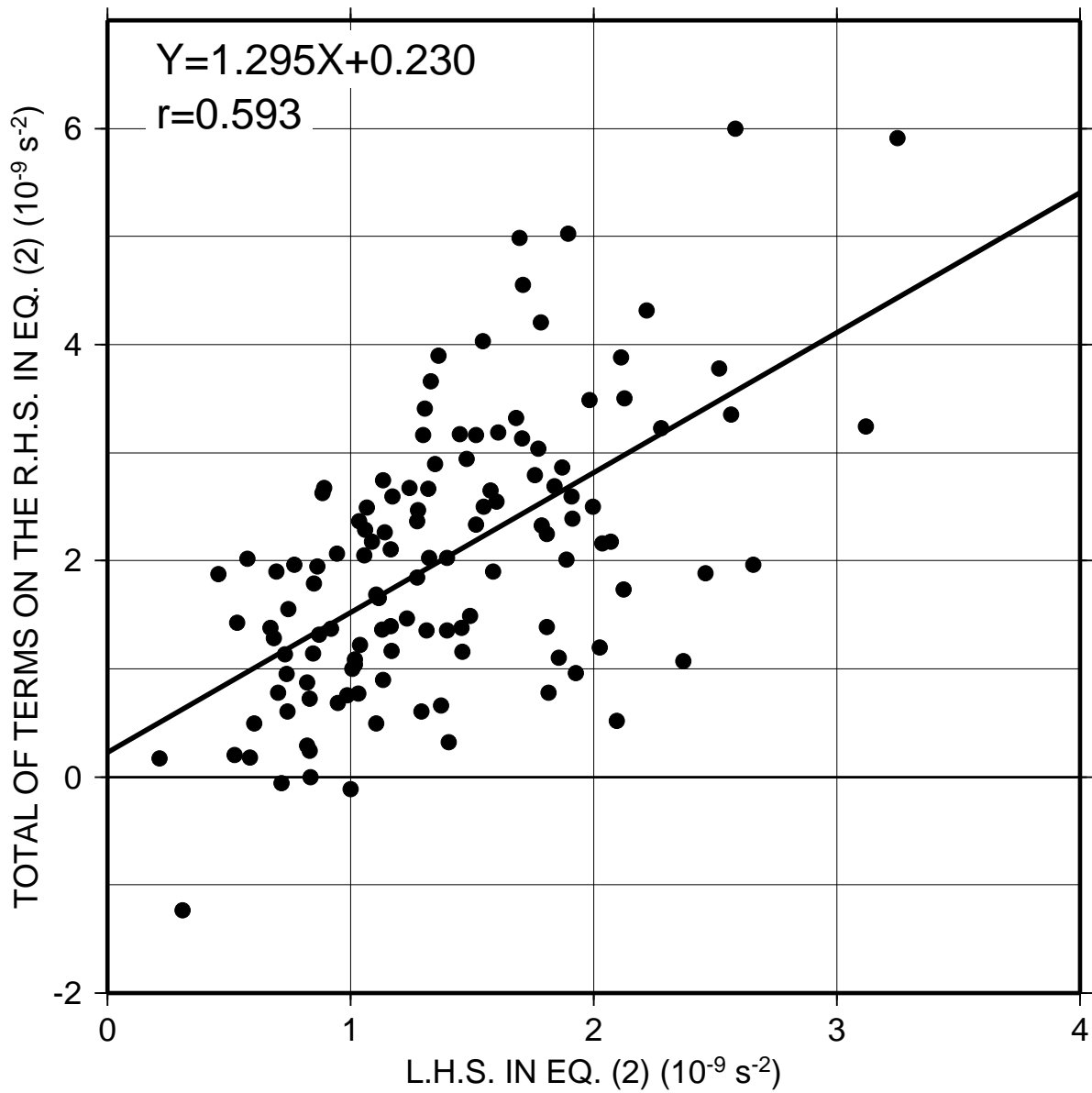


Figure 12. Scatter diagram between the geostrophic relative vorticity tendency at 1000 hPa (L.H.S. in Eq. (2) by finite-difference method, horizontal axis) and the total of terms on the R.H.S in Eq. (2) (vertical axis) averaged in the area within 500 km around surface cyclone center 6 hours after observing the maximum deepening rate. Units are in  $10^{-9} \text{ s}^{-2}$ . Bold line shows the regression line.

Z, HORIZONTAL WIND, JET, W

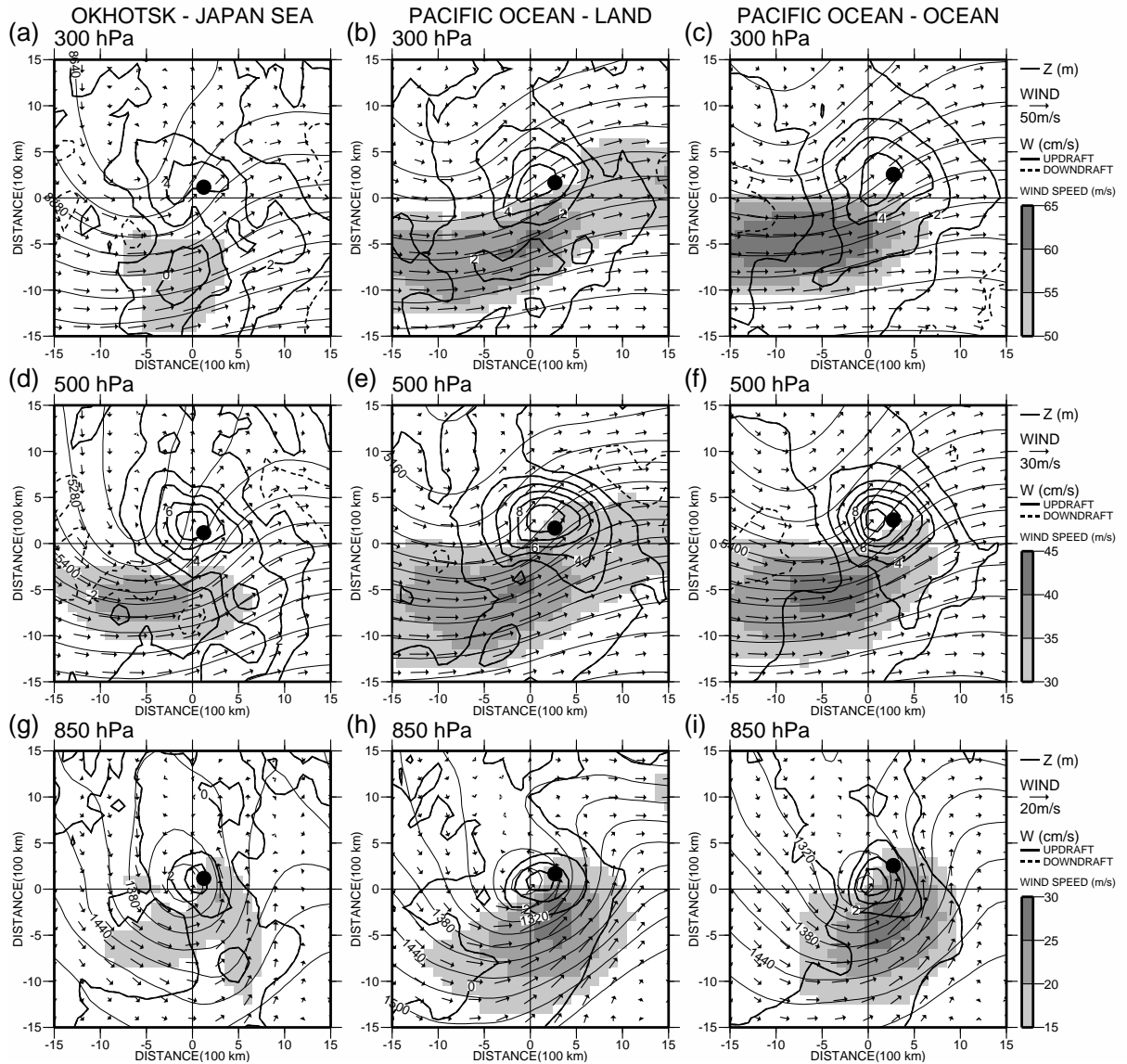


Figure 13. Composite maps at the maximum deepening rate at 300 hPa ((a) - (c)), 500 hPa ((d) - (f)), and 850 hPa ((g) - (i)) for the OJ (left column), PO-L (center column), and PO-O (right column) cyclones of geopotential heights (thin solid lines in m, contour intervals are 120 m at 300 hPa, 60 m at 500 hPa, and 30 m at 850 hPa), horizontal winds (arrows), vertical winds (bold solid lines are updrafts, bold broken lines are downdrafts in  $\text{cm s}^{-1}$ , contour interval is  $2 \text{ cm s}^{-1}$ ), wind speed (shade). Closed circles show the position of the surface cyclone center 6 hours after observing the maximum deepening rate and a center of each panel shows the surface cyclone center.

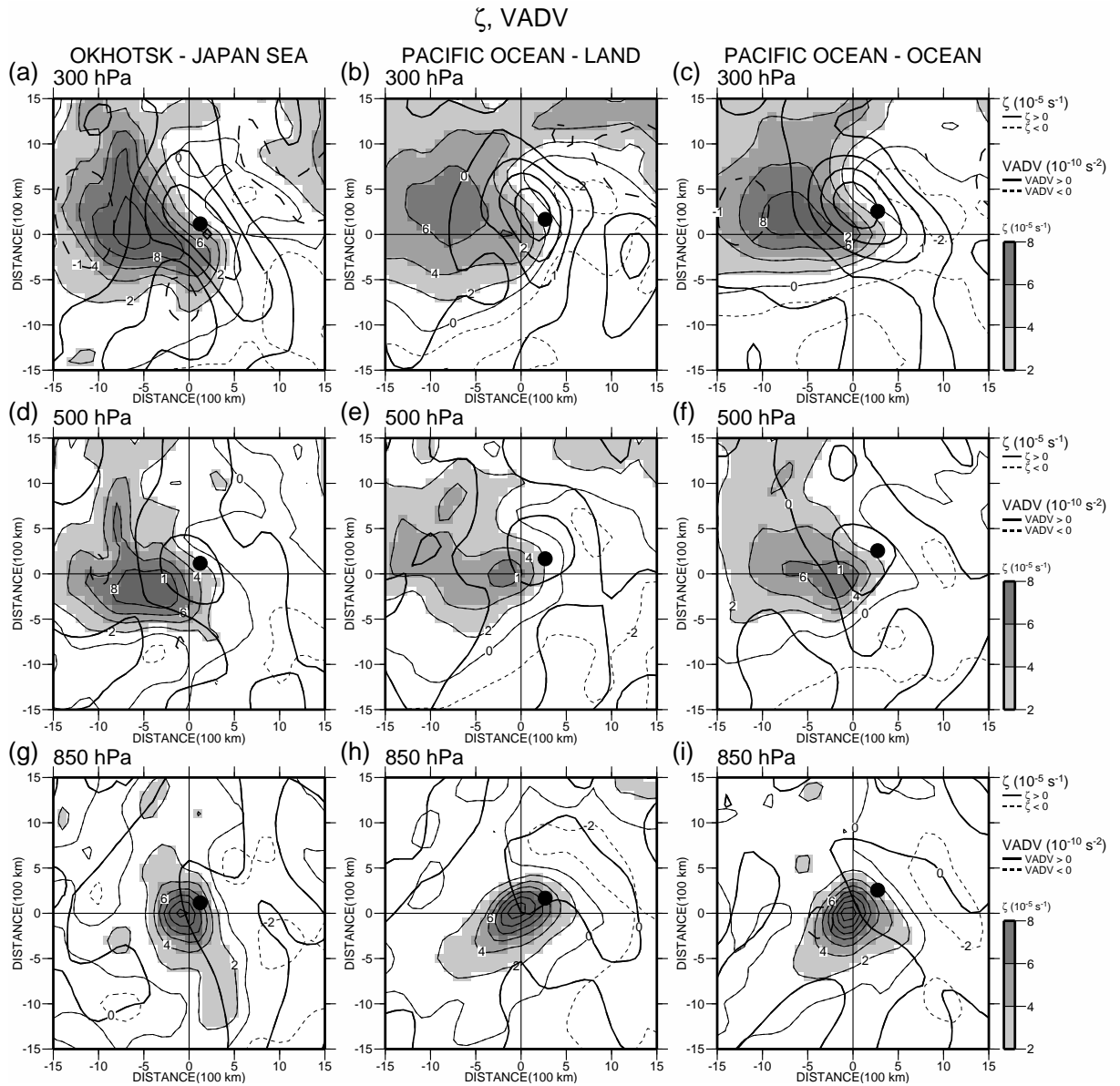


Figure 14. Composite maps at the maximum deepening rate at 300 hPa ((a) - (c)), 500 hPa ((d) - (f)), and 850 hPa ((g) - (i)) for the OJ (left column), PO-L (center column), and PO-O (right column) cyclones of relative vorticity (thin solid lines are positive, thin broken lines are negative, the contour line interval is  $2 \times 10^{-5} \text{ s}^{-1}$ , area greater than  $2 \times 10^{-5} \text{ s}^{-1}$  is shaded) and VADV term (bold solid lines are positive, bold broken lines are negative in  $10^{-10} \text{ s}^{-2}$ , contour interval is  $1 \times 10^{-10} \text{ s}^{-2}$ ). Closed circles show the position of the surface cyclone center 6 hours after maximum deepening rate and a center of each panel shows the surface cyclone center.

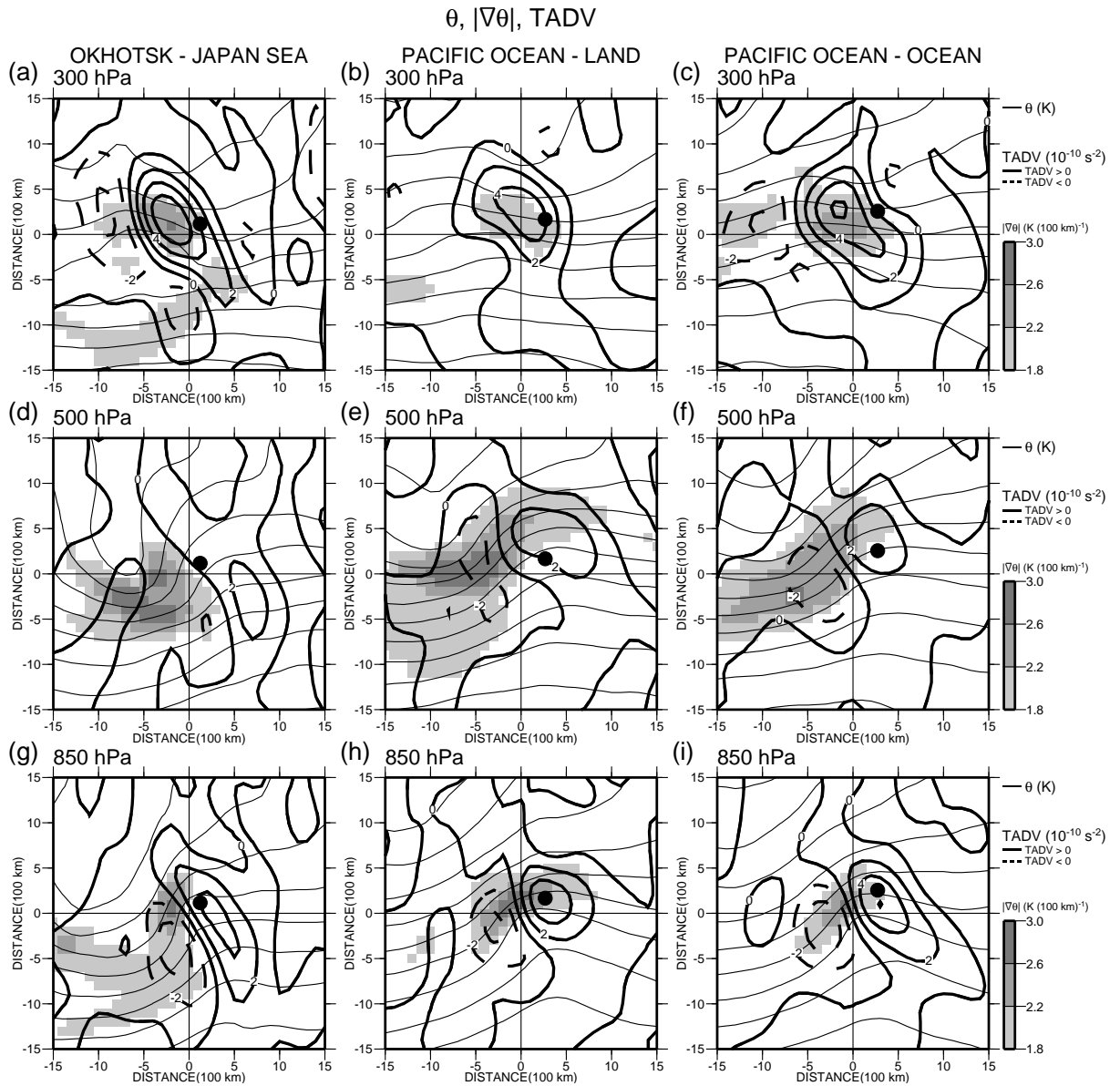


Figure 15. Composite maps at the maximum deepening rate at 300 hPa ((a) - (c)), 500 hPa ((d) - (f)), and 850 hPa ((g) - (i)) for the OJ (left column), PO-L (center column), and PO-O (right column) cyclones of potential temperature (thin lines in K, contour interval is 4 K), TADV term (bold solid lines are positive, bold broken lines are negative in  $10^{-10} \text{ s}^{-2}$ , the contour interval is  $2 \times 10^{-10} \text{ s}^{-2}$ ) and horizontal gradients of potential temperature (shade in  $\text{K (100 km)}^{-1}$ ). Closed circles show the position of the surface cyclone center 6 hours after observing the maximum deepening rate and a center of each panel shows the surface cyclone center.

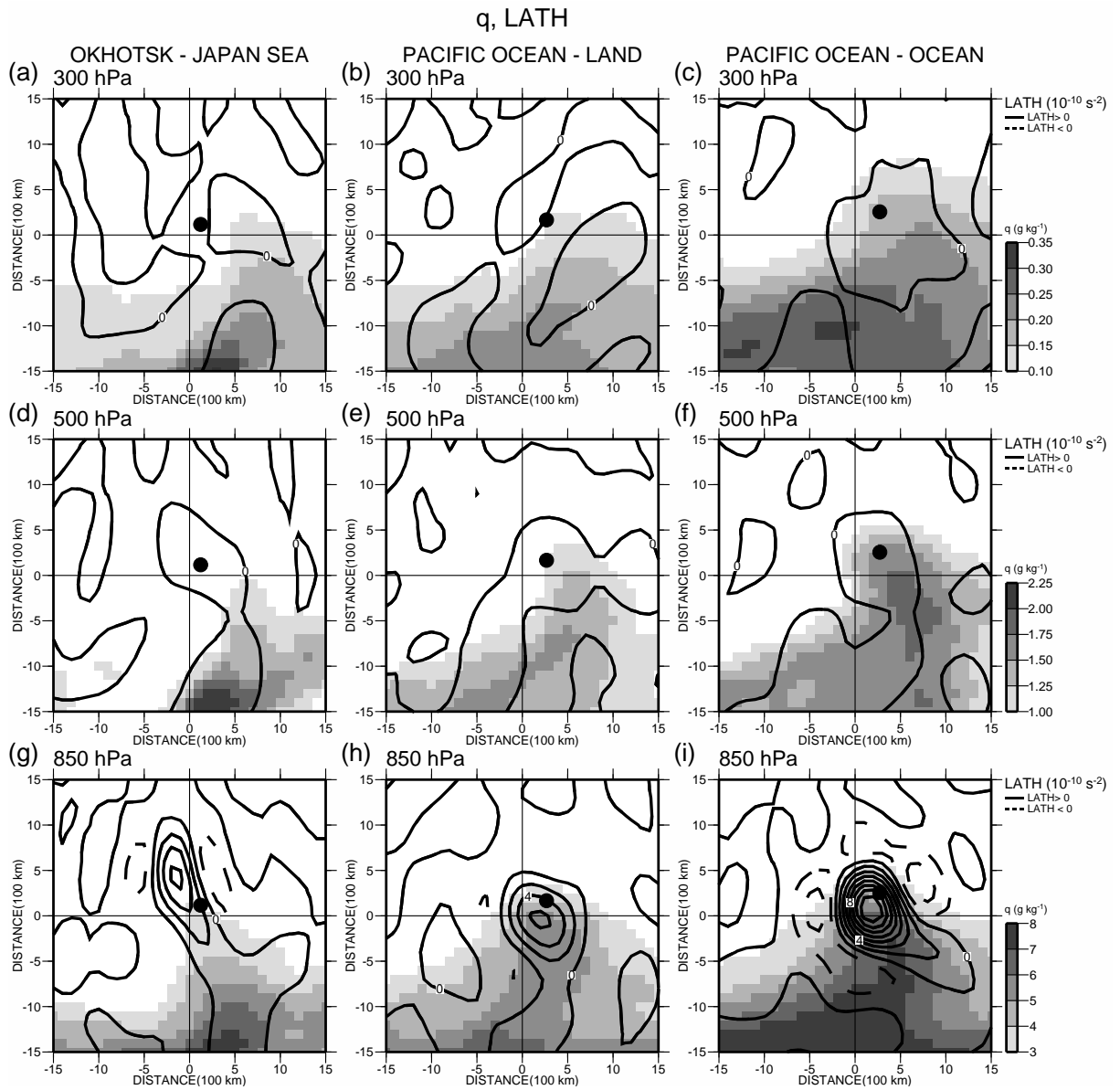


Figure 16. Composite maps at the maximum deepening rate at 300 hPa ((a) - (c)), 500 hPa ((d) - (f)), and 850 hPa ((g) - (i)) for the OJ (left column), PO-L (center column), and PO-O (right column) cyclones of specific humidity (shade in  $\text{g kg}^{-1}$ ) and LATH term (solid lines are positive, broken lines are negative in  $10^{-10} \text{ s}^{-2}$ , contour interval is  $2 \times 10^{-10} \text{ s}^{-2}$ ). Closed circles show the position of the surface cyclone center 6 hours after observing the maximum deepening rate and a center of each panel shows the surface cyclone center.

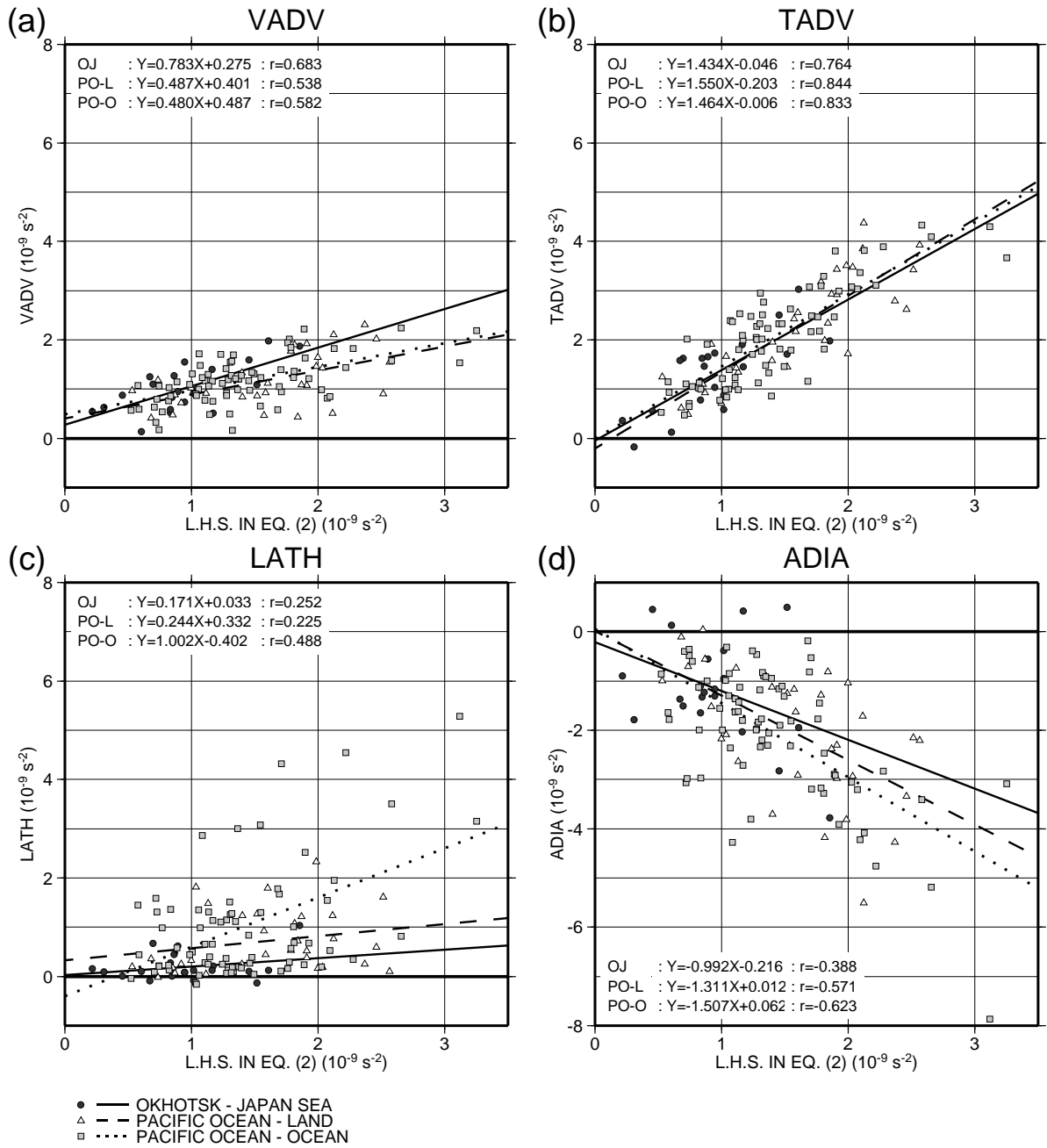


Figure 17. Scatter diagrams between the geostrophic vorticity tendency at 1000 hPa (L.H.S. in Eq. (2) by finite-difference method, horizontal axis) and each term on R.H.S. in Eq. (2) (vertical axis), i.e., (a) VADV, (b) TADV, (c) LATH and (d) ADIA. for OJ cyclones (closed circles and solid line shows a regression line), PO-L cyclones (triangles and broken line shows a regression line) and PO-O cyclones (squares and dotted line shows a regression line). Value were averaged in the area within 500 km near the surface cyclone center 6 hours after observing the maximum deepening rate.

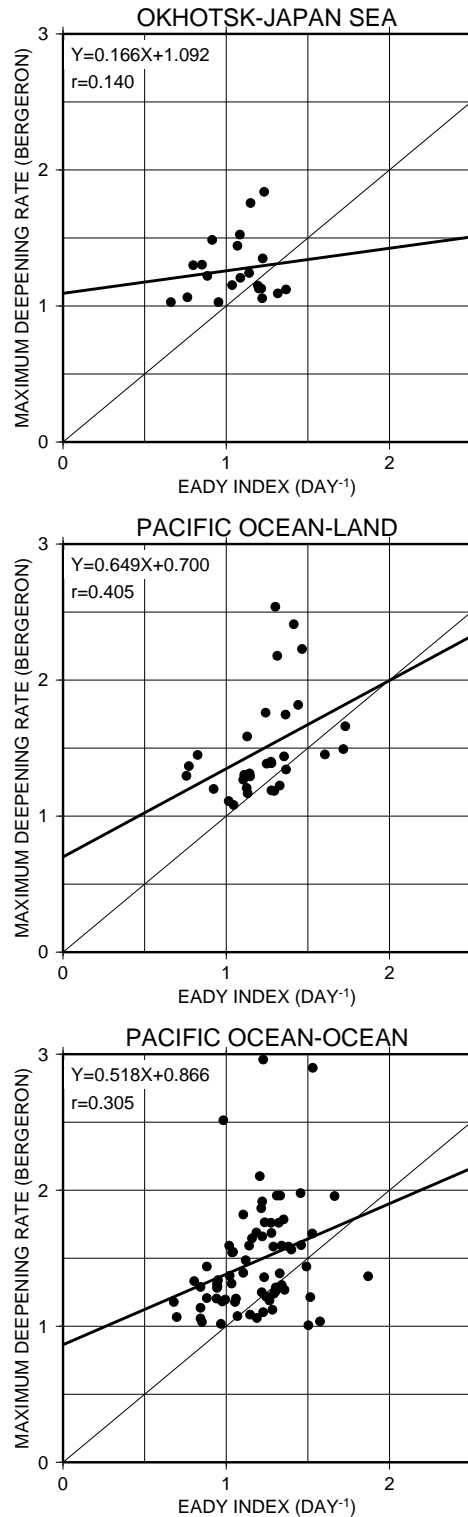


Figure 18. Scatter diagrams between the Eady index estimated by 300- and 1000-hPa horizontal winds and potential temperatures (horizontal axis) averaged over an area within 500 km around cyclone center when observing the maximum deepening rate and maximum deepening rate (vertical axis) for (a) OJ, (b) PO-L, and (c) PO-O cyclones. Solid lines show regression lines corresponding with equations with correlation coefficient ( $r$ ) at upper left in panels.

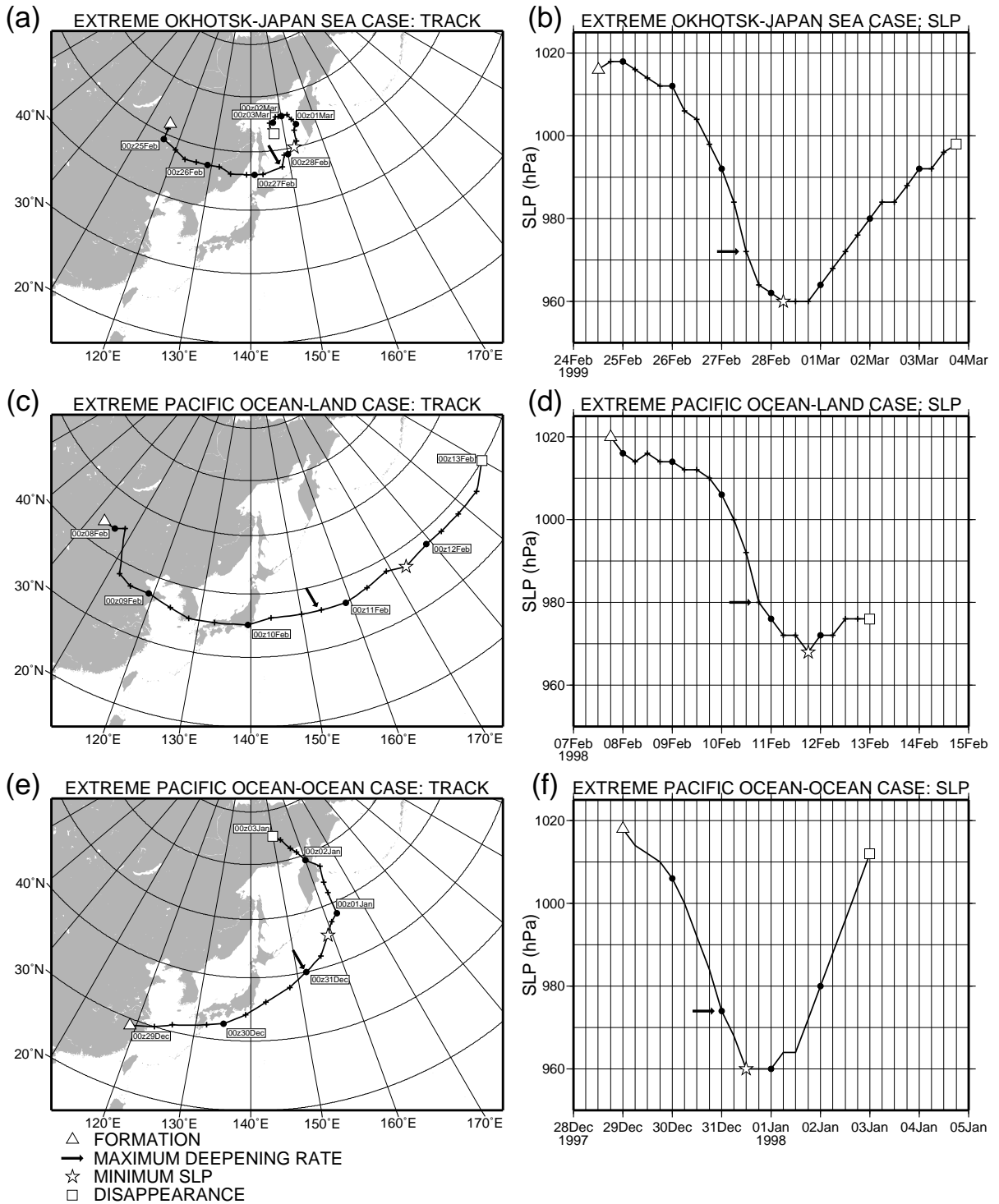
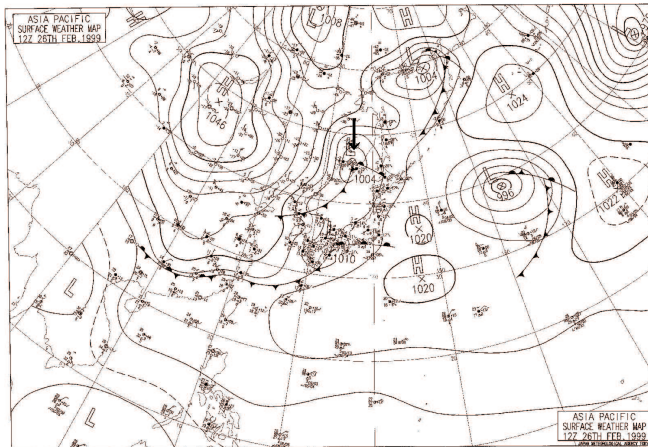


Figure 19. Surface cyclone tracks (lines, cross shows 6 hour interval position, closed circle shows position at every 0000 UTC) in left column and time series of central sea level pressure in right column for (a) and (b) extreme OJ, (c) and (d) extreme PO-L, and (e) and (f) extreme PO-O cases between the formation (triangle) and the disappearance (square) by surface weather map provided by JMA. Star shows the minimum sea-level pressure. Arrow shows the maximum deepening rate determined by GANAL analysis.

### EXTREME OKHOTSK-JAPAN SEA CASE

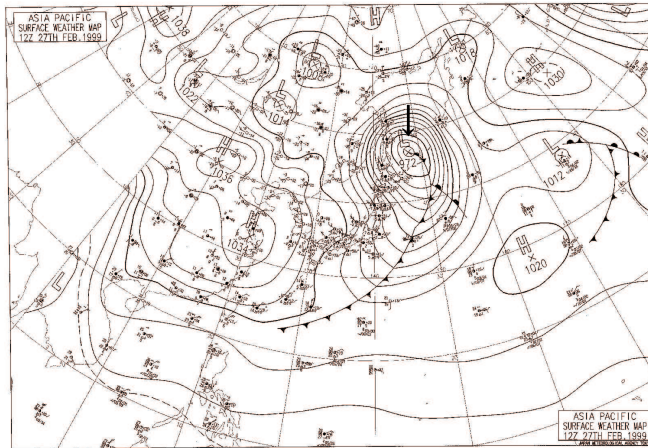
(a)

1200 UTC 26 FEBRUARY 1999 (T-24 hour)



(b)

1200 UTC 27 FEBRUARY 1999 (T=0 hour)



(c)

1200 UTC 28 FEBRUARY 1999 (T+24 hour)

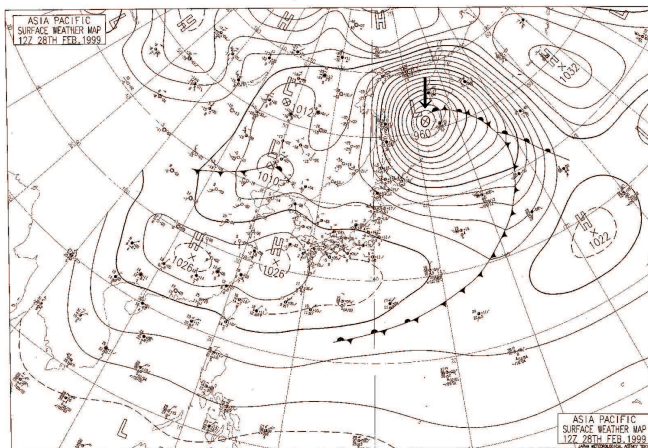
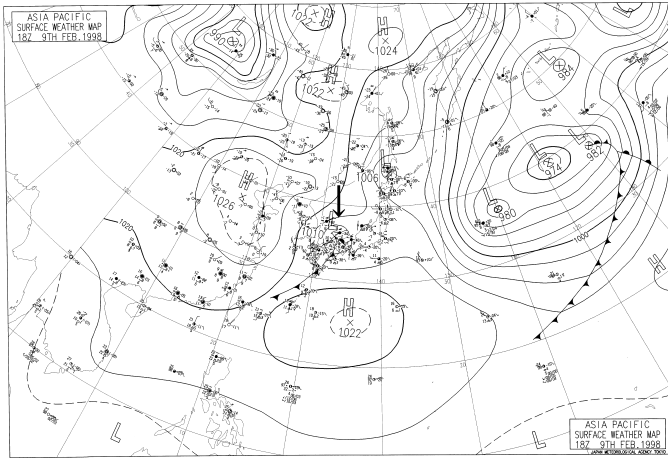


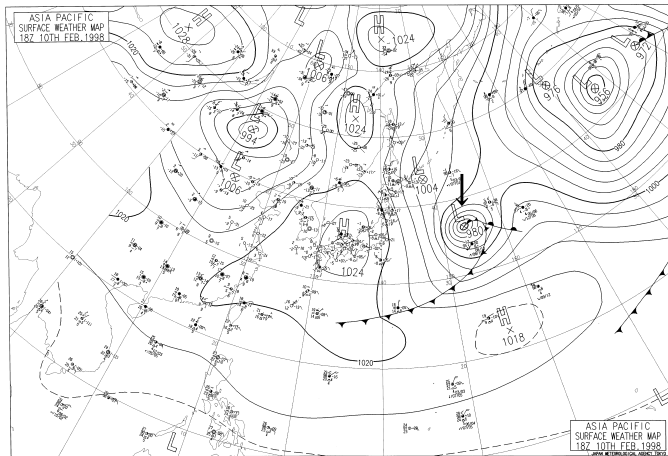
Figure 20. Time series of surface weather map provided by JMA for the extreme OJ case (marked by arrow) at (a) 1200 UTC 26 February 1999, (b) 1200 UTC 27 February 1999, and (c) 1200 UTC 28 February 1999. Solid line shows sea level pressure (unit of hPa, contour interval is 4 hPa). Surface fronts and surface weather reports are described by conventional notation.

# EXTREME PACIFIC OCEAN-LAND CASE

(a) 1800 UTC 9 FEBRUARY 1998 (T-24 hour)



(b) 1800 UTC 10 FEBRUARY 1998 (T=0 hour)



(c) 1800 UTC 11 FEBRUARY 1998 (T+24 hour)

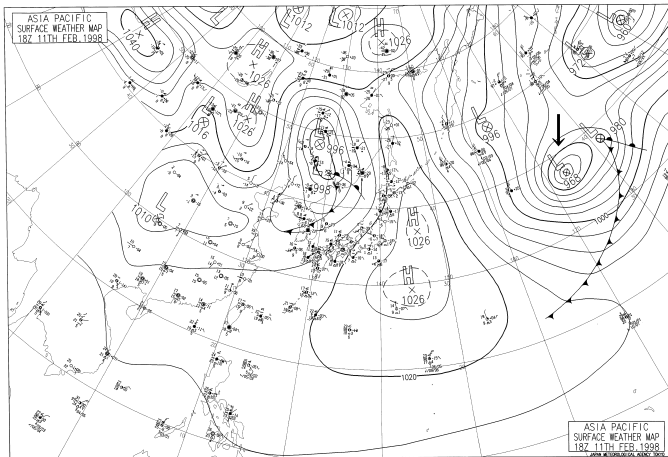
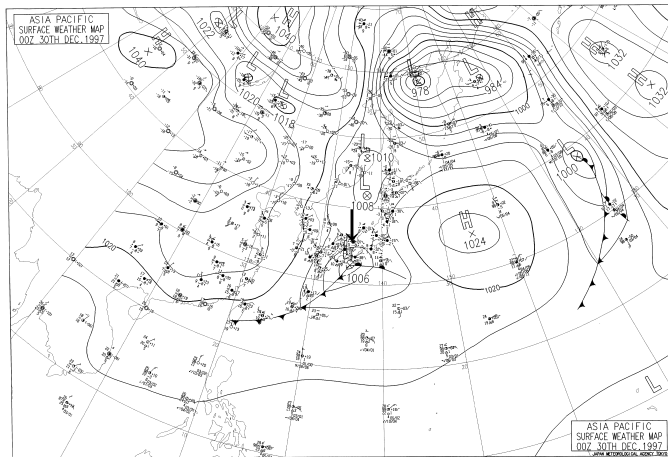
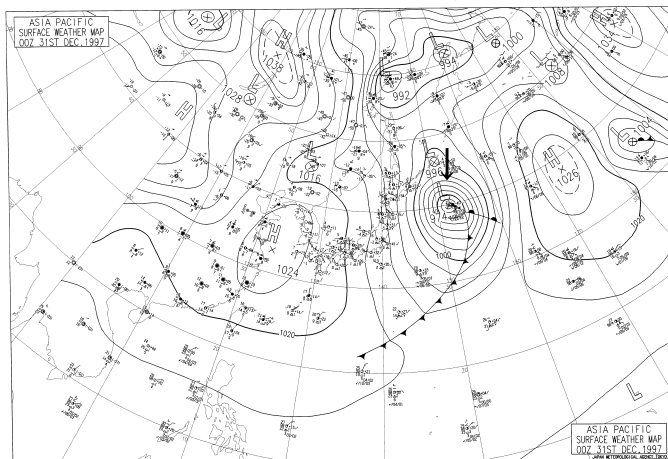


Figure 21. Same as Fig. 20, but for the extreme PO-L case at (a) 1800 UTC 9 February 1998, (b) 1800 UTC 10 February 1998, and (c) 1800 UTC 11 February 1998.

**EXTREME PACIFIC OCEAN-OCEAN CASE**  
**(a) 0000 UTC 30 DECEMBER 1997 (T-24 hour)**



**(b) 0000 UTC 31 DECEMBER 1997 (T=0 hour)**



**(c) 0000 UTC 1 JANUARY 1998 (T+24 hour)**

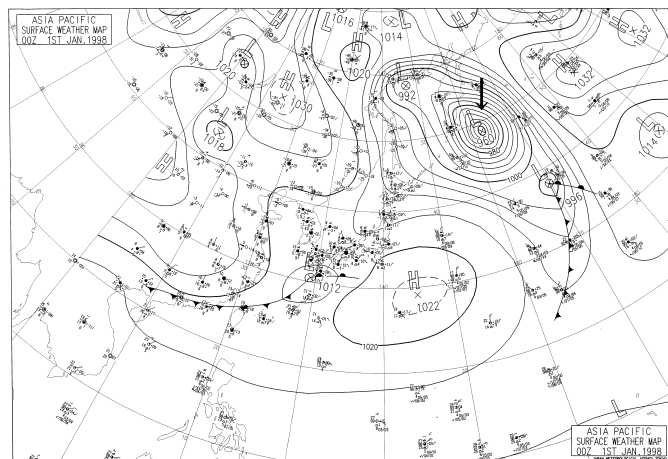


Figure 22. Same as Fig. 20, but for the extreme PO-O case at (a) 0000 UTC 30 December 1997, (b) 0000 UTC 31 December 1997, and (c) 0000 UTC 1 January 1998.

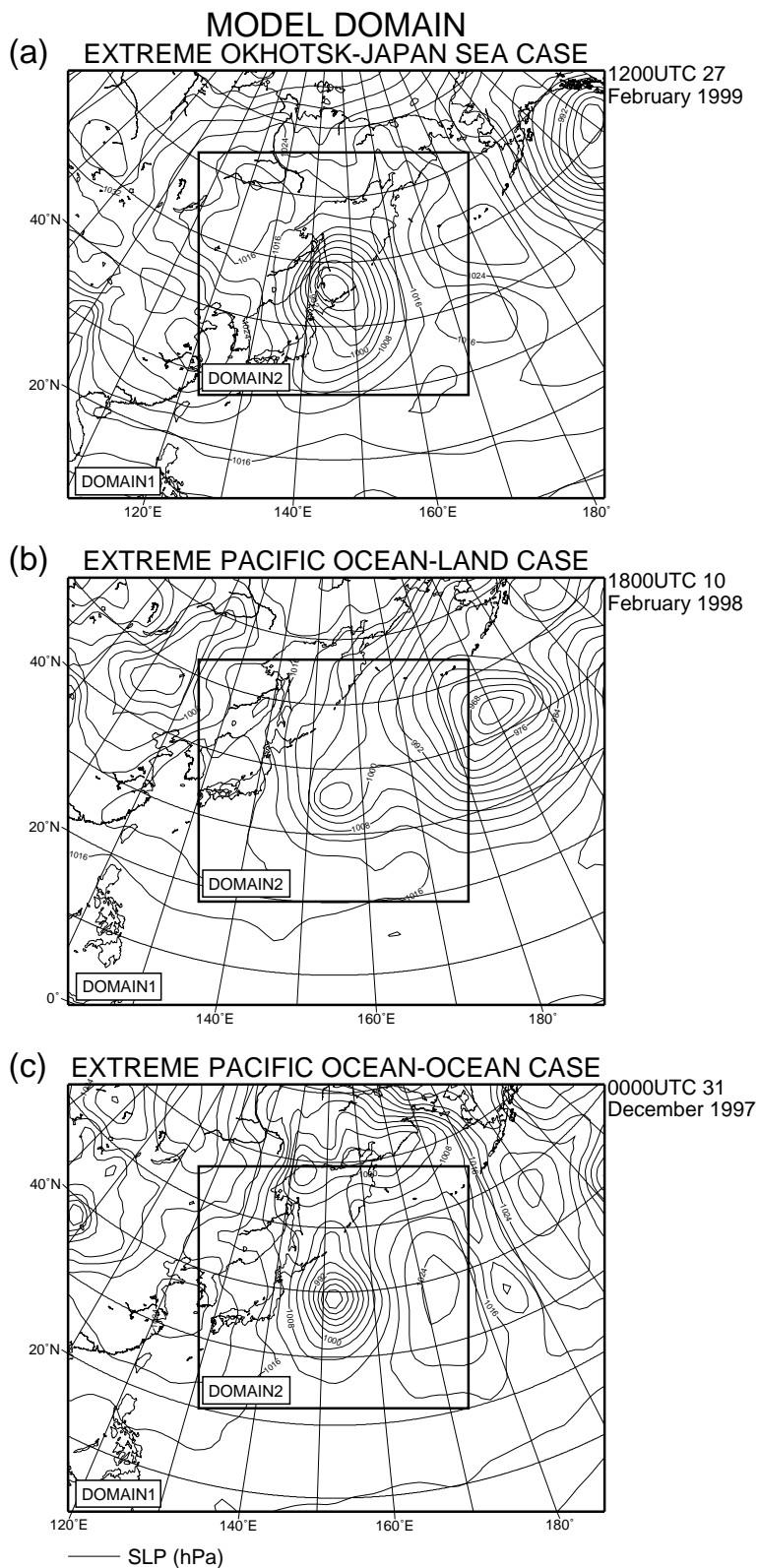


Figure 23. Model domains and sea-level pressure in GANAL analysis (solid line, unit of hPa, contour interval is 4 hPa) (a) at 1200 UTC 27 February 1999 for the extreme OJ case, (b) 1800 UTC 10 February 1998 for the extreme PO-L case, and (c) 0000 UTC 31 December 1997 for the extreme PO-O case.

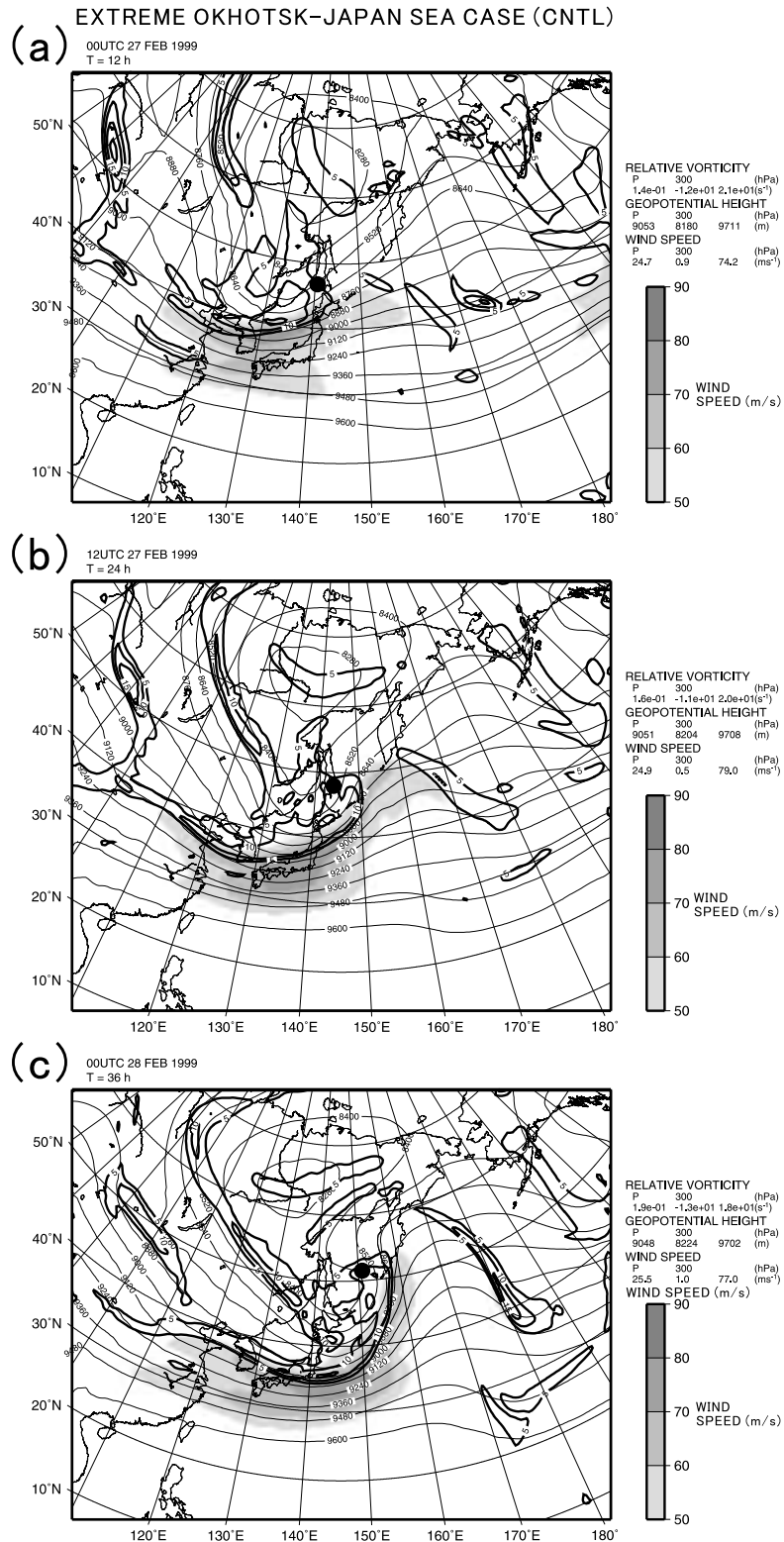


Figure 24. Geopotential height (thin solid line, unit of m, contour interval is 120 m), positive relative vorticity (bold solid line, unit of  $10^{-5} s^{-1}$ , contour interval is  $5 \cdot 10^{-5} s^{-1}$ ), and horizontal wind speed (shade, unit of  $m s^{-1}$ ) at 300 hPa at (a) T = 12 h, (b) T = 24 h, and (c) T = 36 h of the extreme OJ CNTL. Closed circle is the position of surface cyclone center.

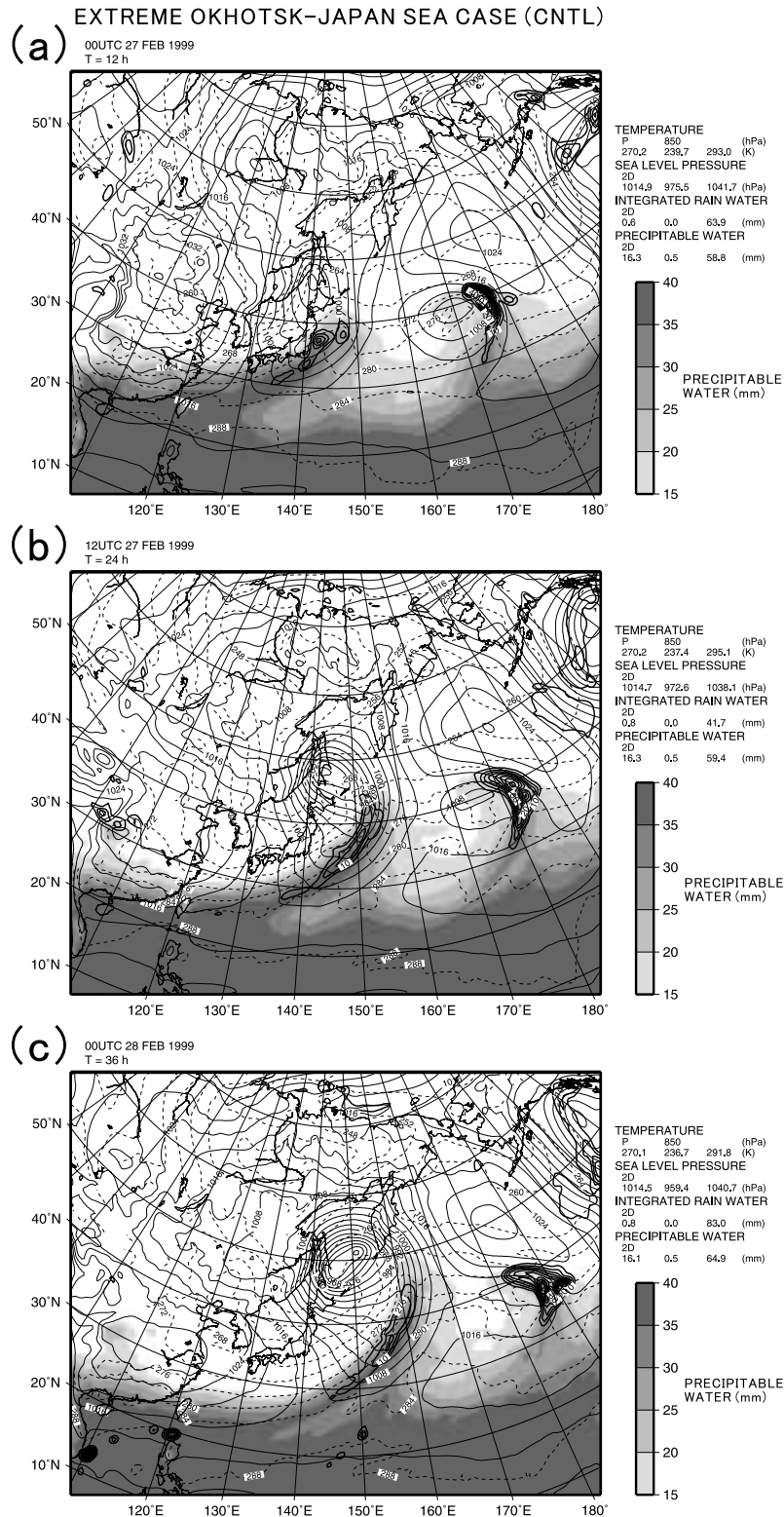


Figure 25. Sea-level pressure (thin solid line, unit of hPa, contour interval is 4 hPa), vertical integrated rain water (bold solid line, unit of mm, contour interval is 5 mm), precipitable water (shade, unit of mm), and temperature at 850 hPa (broken line, unit of K, contour interval is 4 K) at (a) T = 12 h, (b) T = 24 h and (c) T = 36 h of the extreme OJ CNTL.

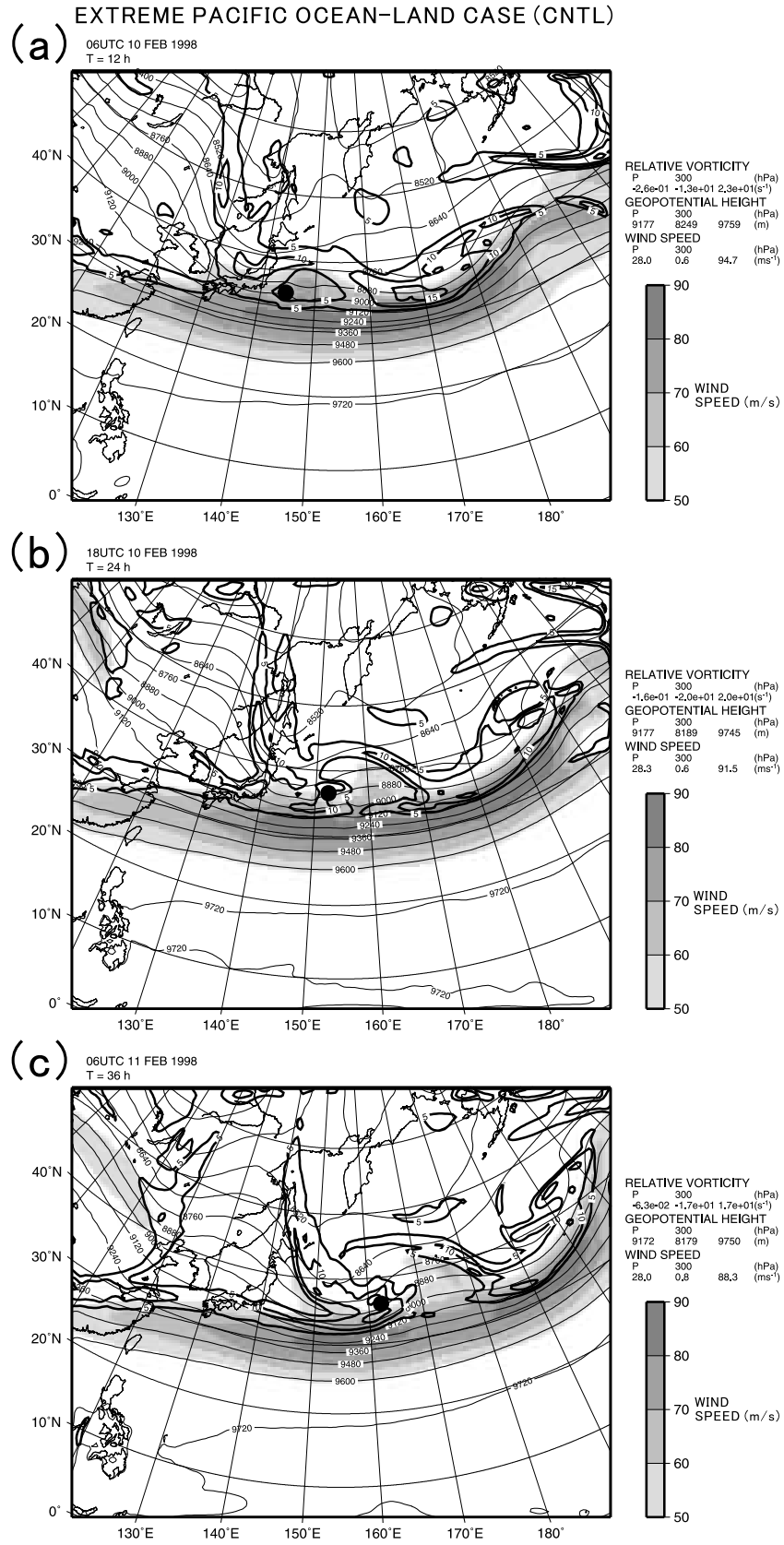
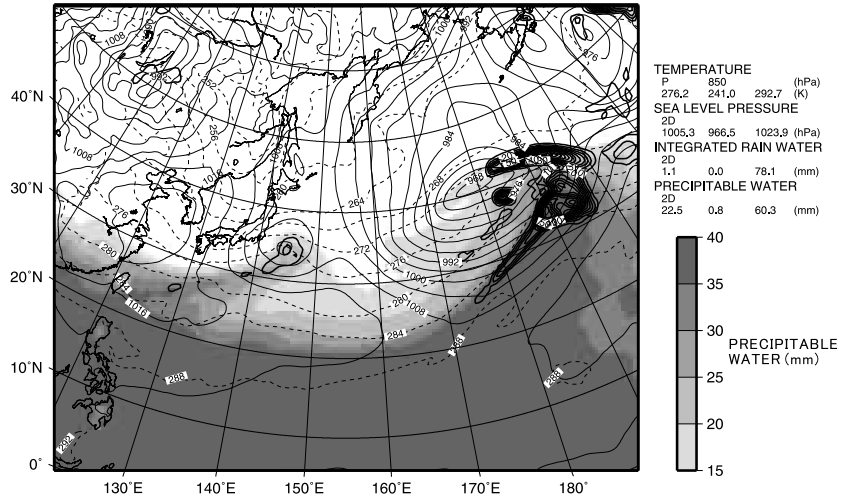
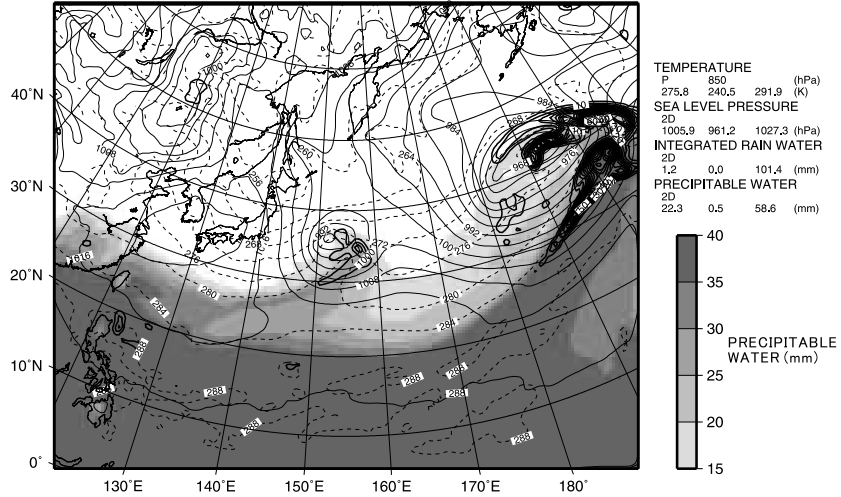


Figure 26. Same as Fig. 24, but of the extreme PO-L CNTL.

**(a)** EXTREME PACIFIC OCEAN-LAND CASE (CNTL)  
 06UTC 10 FEB 1998  
 T = 12 h



**(b)** 18UTC 10 FEB 1998  
 T = 24 h



**(c)** 06UTC 11 FEB 1998  
 T = 36 h

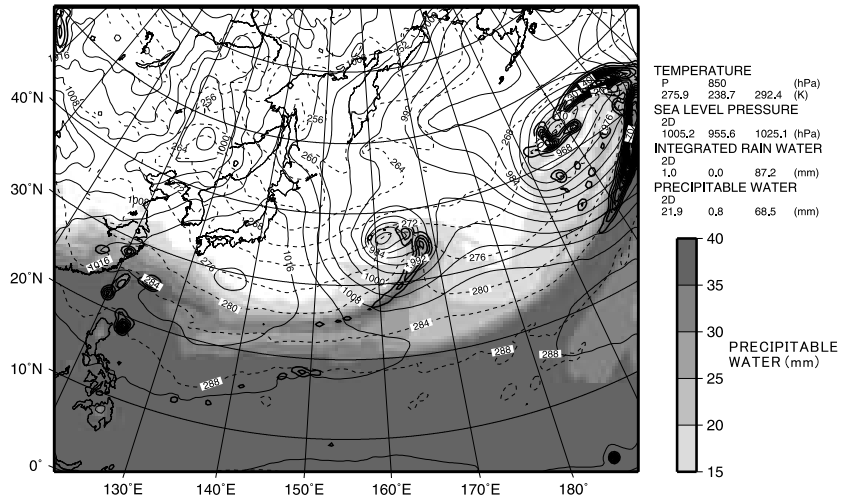


Figure 27. Same as Fig. 25, but of the extreme PO-L CNTL.

EXTREME PACIFIC OCEAN-OCEAN CASE (CNTL)

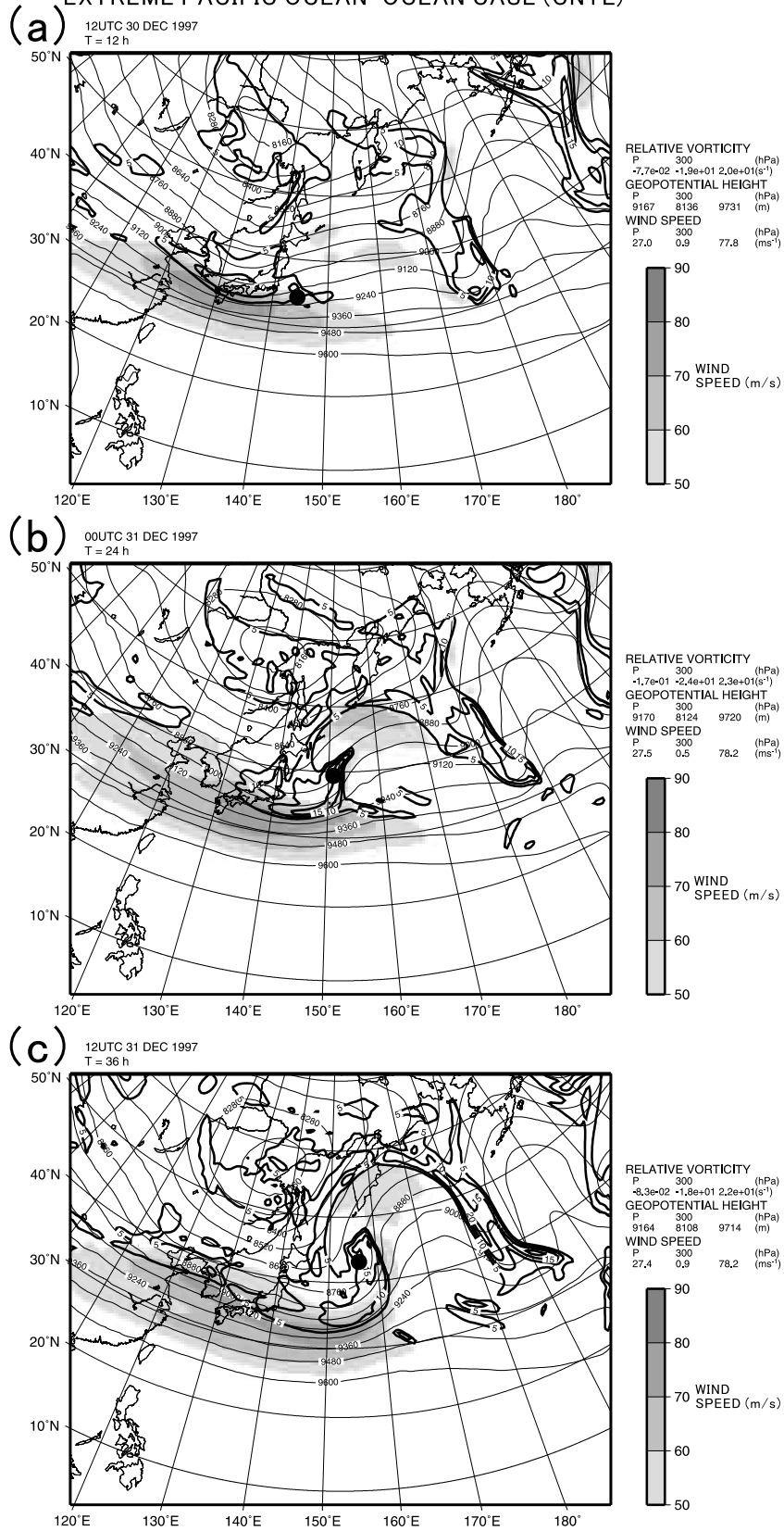


Figure 28. Same as Fig. 24, but of the extreme PO-O CNTL.

EXTREME PACIFIC OCEAN-OCEAN CASE (CNTL)

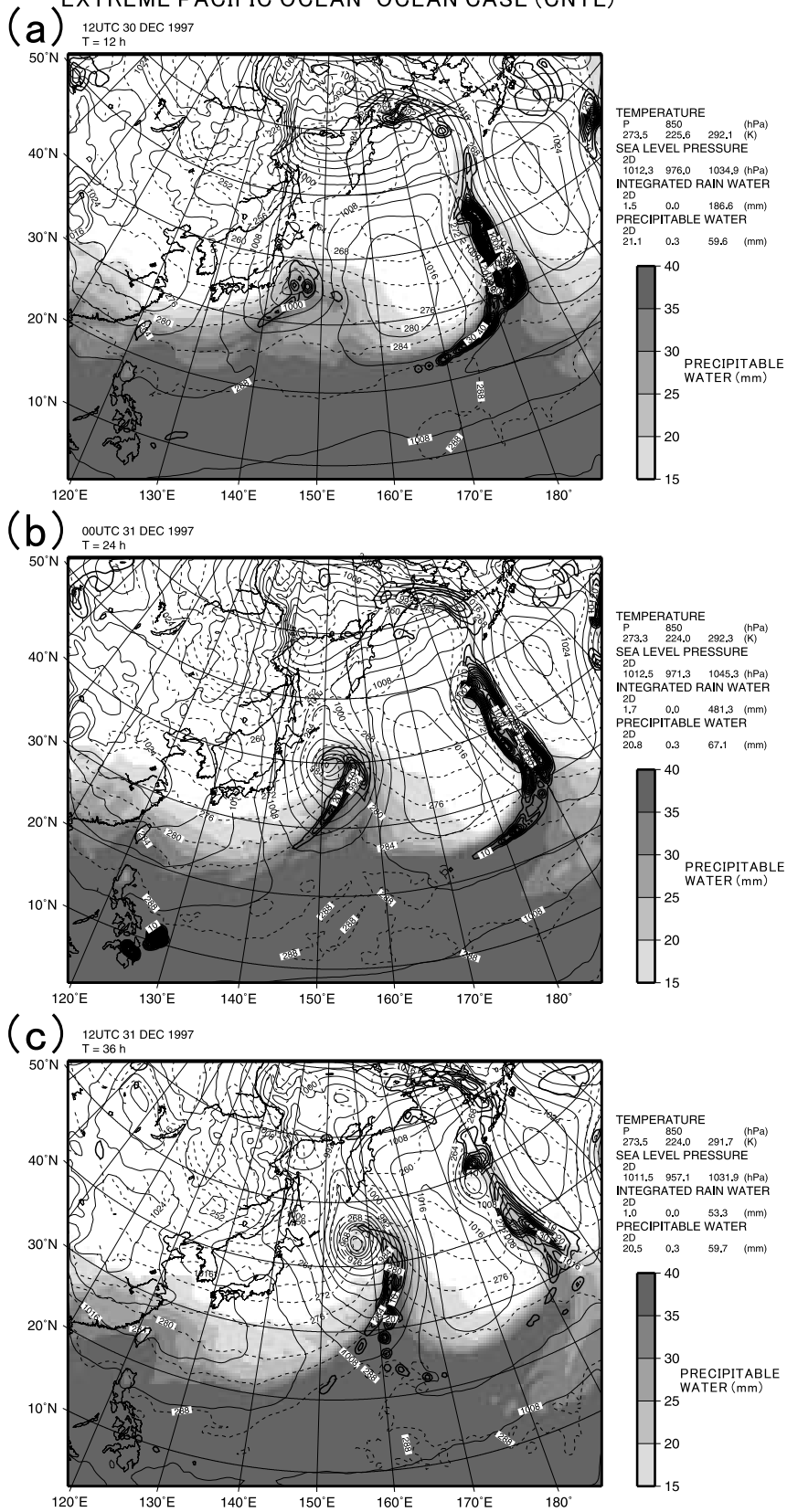


Figure 29. Same as Fig. 25, but of the extreme PO-O CNTL.

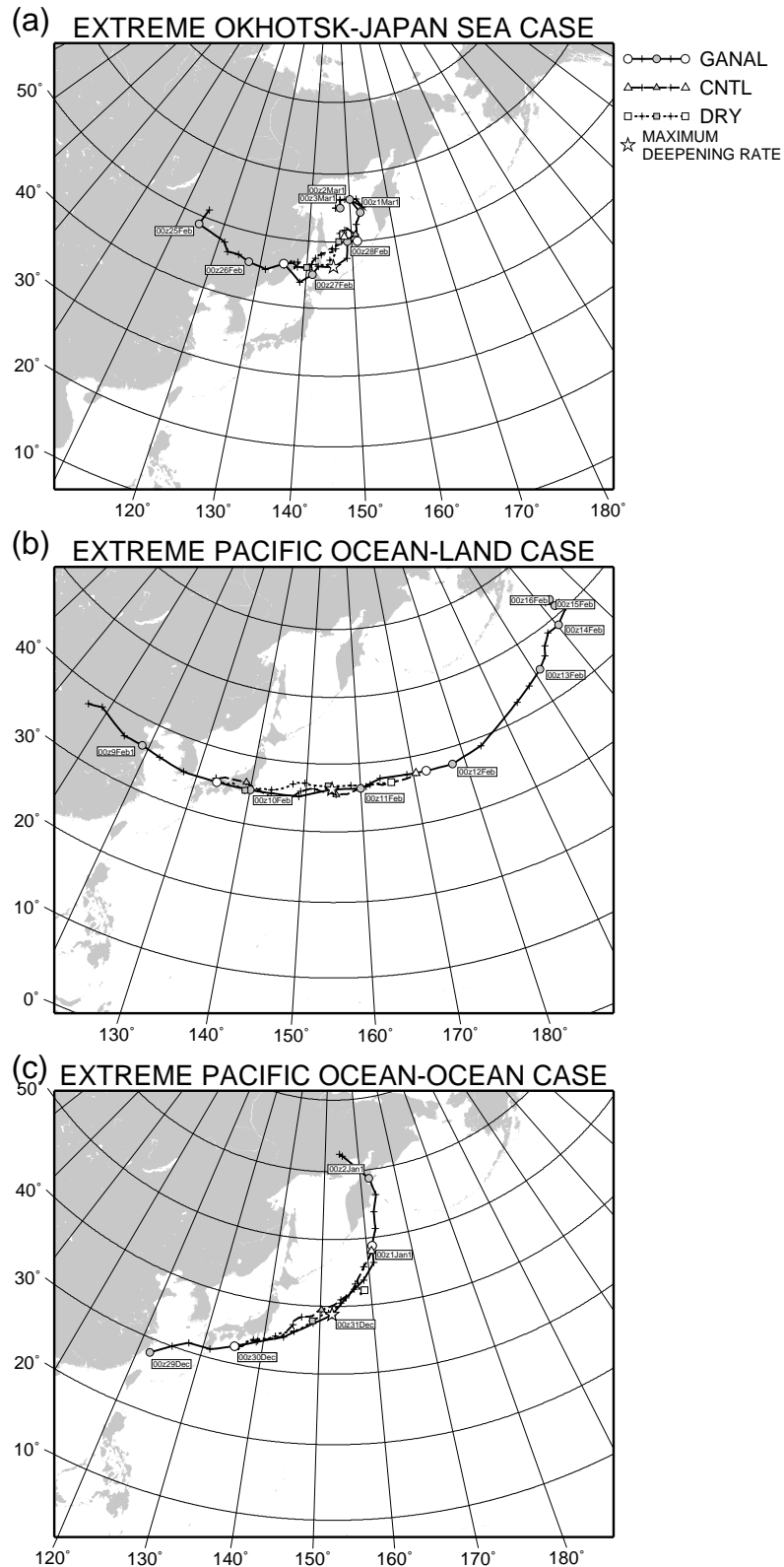


Figure 30. Surface cyclone tracks (lines, cross shows 6 hour interval position, gray mark shows position at every 0000 UTC) for (a) extreme OJ, (b) extreme PO-L, and (c) extreme PO-O cases. Solid line with circle is GANAL analysis, broken line with triangle is CNTL run, and dotted line with square is DRY run. Star shows the maximum deepening rate for GANAL analysis.

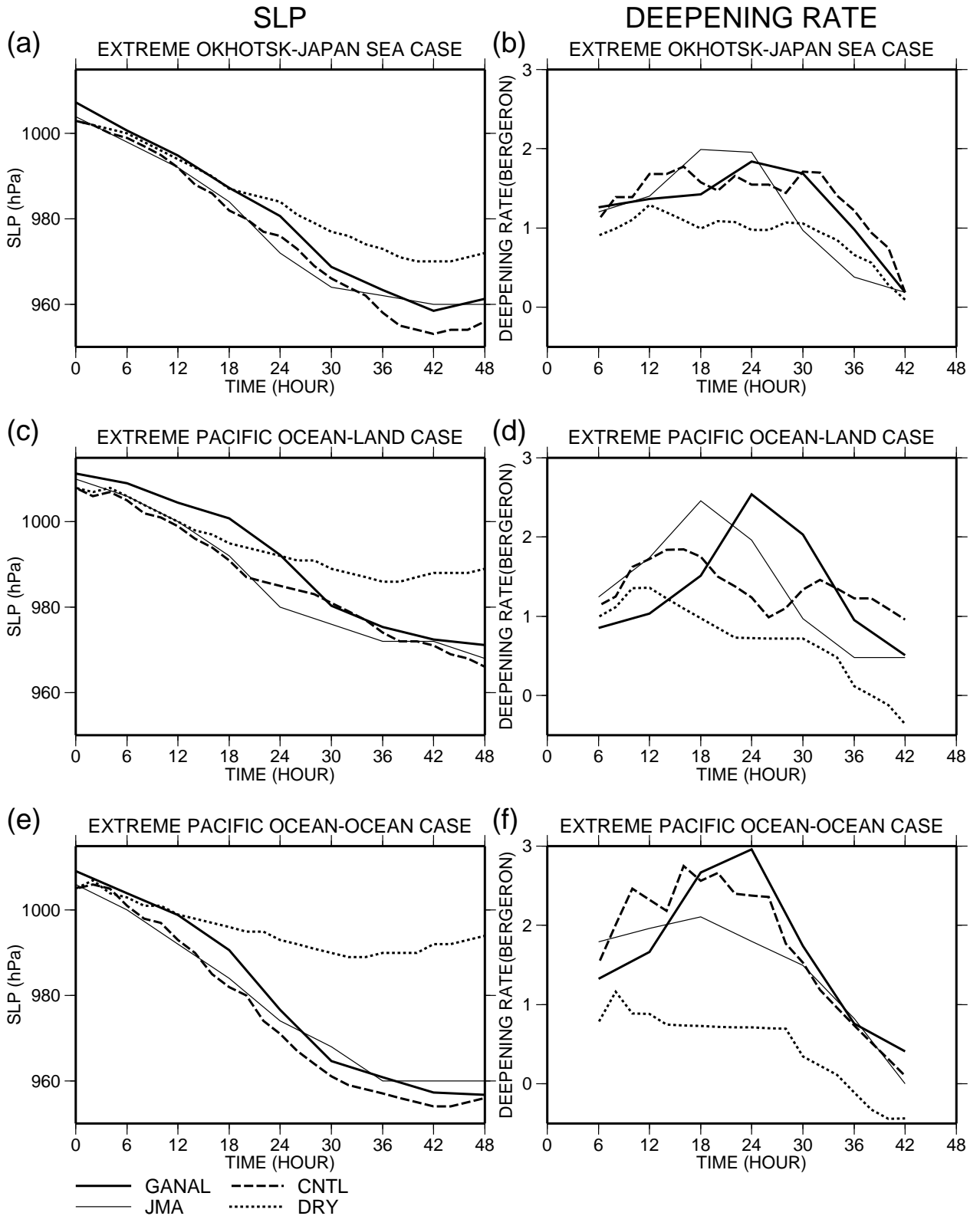


Figure 31. Temporal variation of the central sea level pressure (left column) and deepening rate (right column) during the simulated term for (a) and (b) extreme OJ, (c) and (d) extreme PO-L, and (e) and (f) extreme PO-O cases, Bold solid line is GANAL analysis, thin solid line is JMA analysis, broken line is CNTL run and dotted line is DRY run.

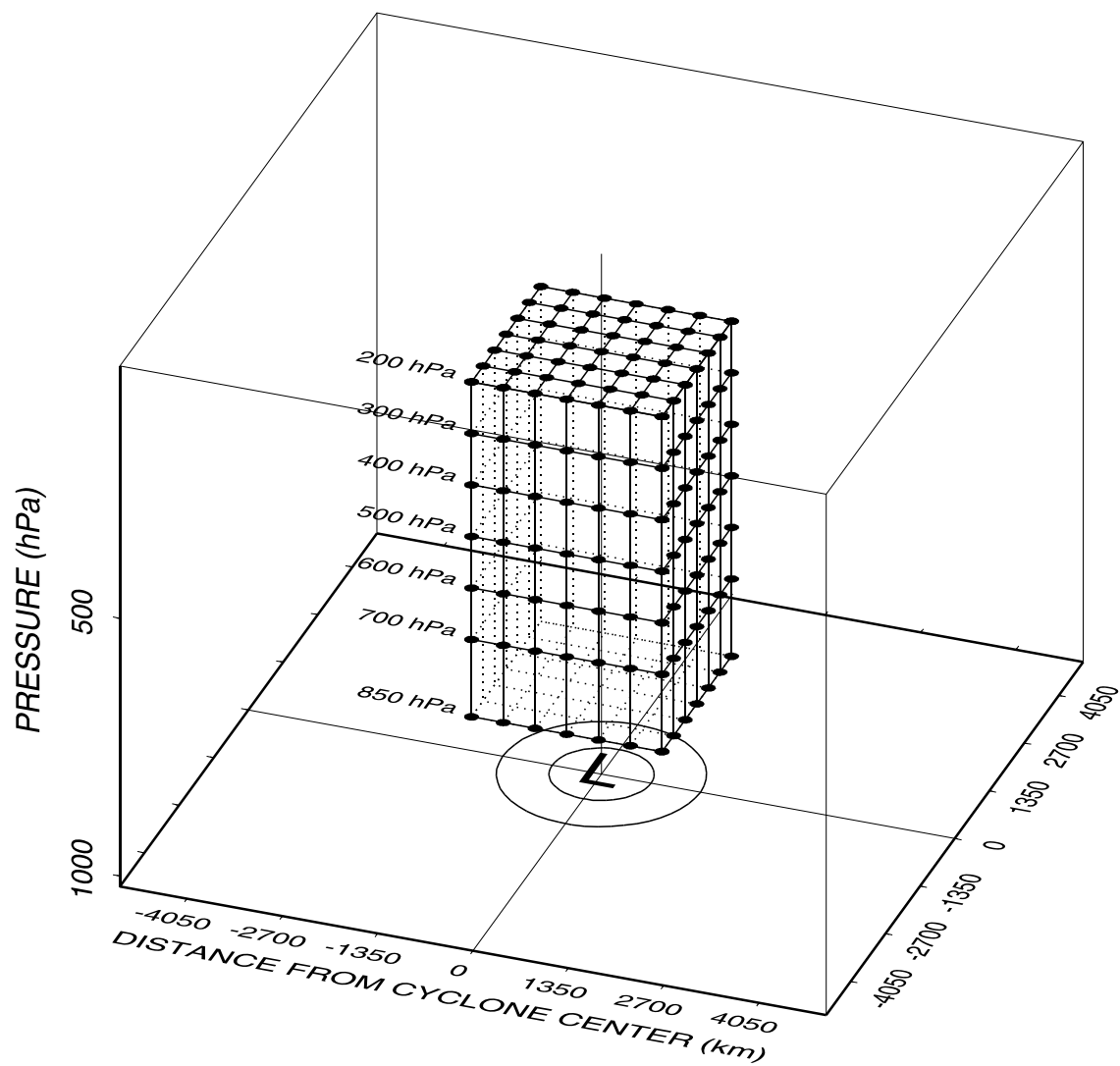
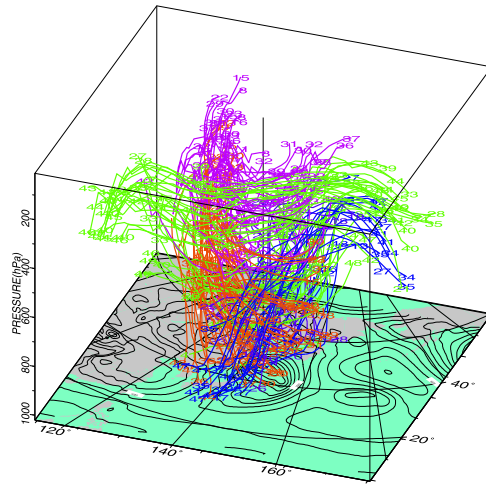
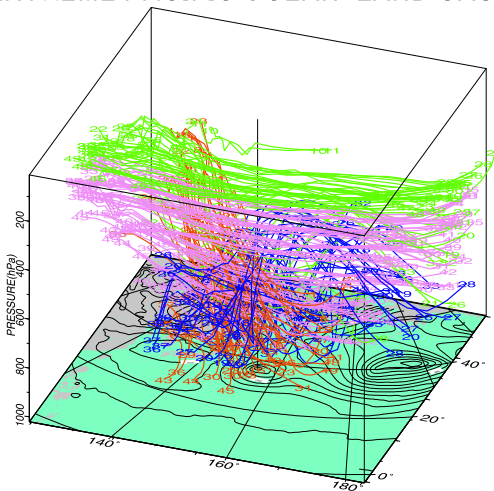


Figure 32. Schematic illustration of the initial arrangement of air parcels for trajectory analysis. L shows the surface cyclone center at the maximum deepening rate.

TRAJECTORY NEAR THE CYCLONE CENTER  
 (a) EXTREME OKHOTSK–JAPAN SEA CASE



(b) EXTREME PACIFIC OCEAN–LAND CASE



(c) EXTREME PACIFIC OCEAN–OCEAN CASE

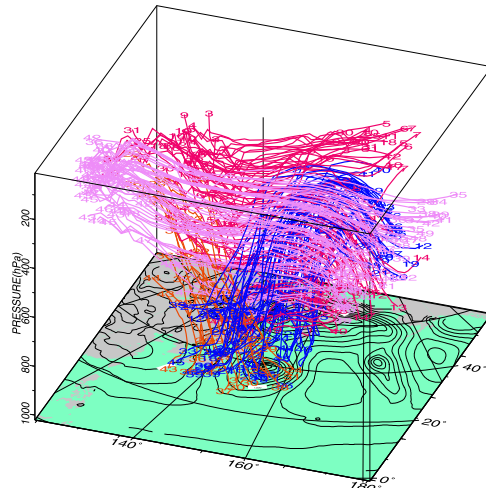


Figure 33. Trajectory analysis for (a) the extreme OJ CNTL, (b) extreme PO-L CNTL, and (c) extreme PO-O CNTL. Sea-level pressure (thin solid line, unit of hPa, contour interval is 4 hPa) at the maximum deepening rate in GANAL analysis is shown in bottom.

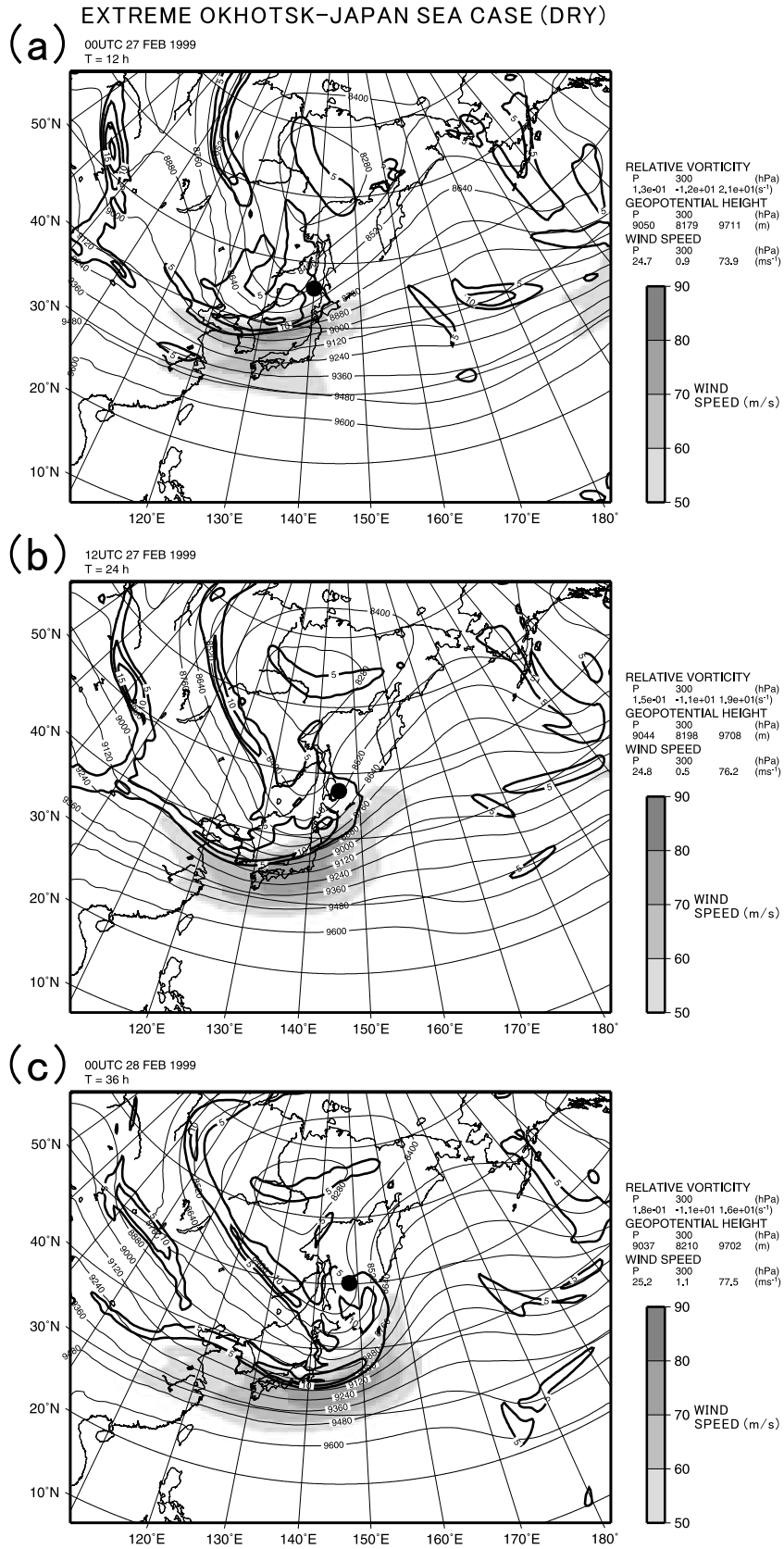
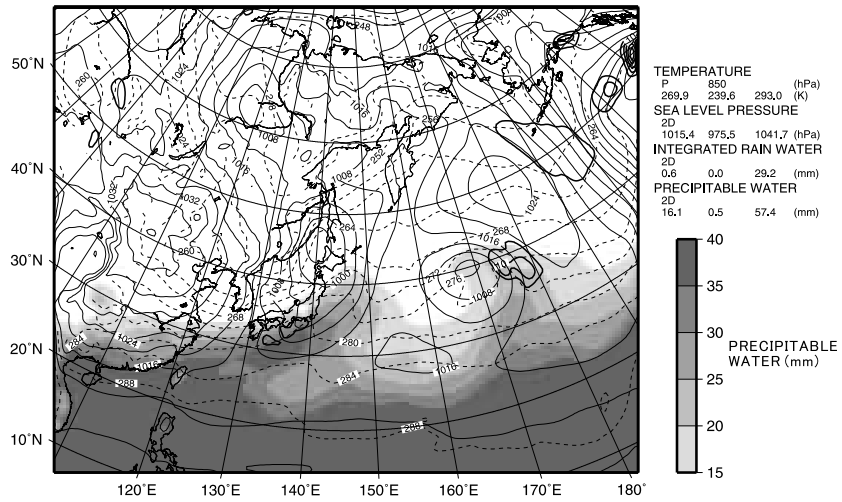
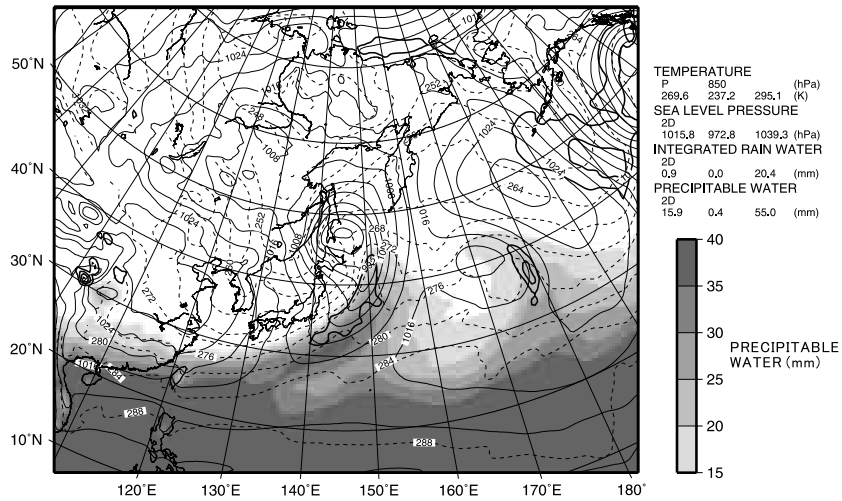


Figure 34. Same as Fig. 24, but of the extreme OJ DRY.

**(a)** EXTREME OKHOTSK-JAPAN SEA CASE (DRY)  
 00UTC 27 FEB 1999  
 T = 12 h



**(b)** 12UTC 27 FEB 1999  
 T = 24 h



**(c)** 00UTC 28 FEB 1999  
 T = 36 h

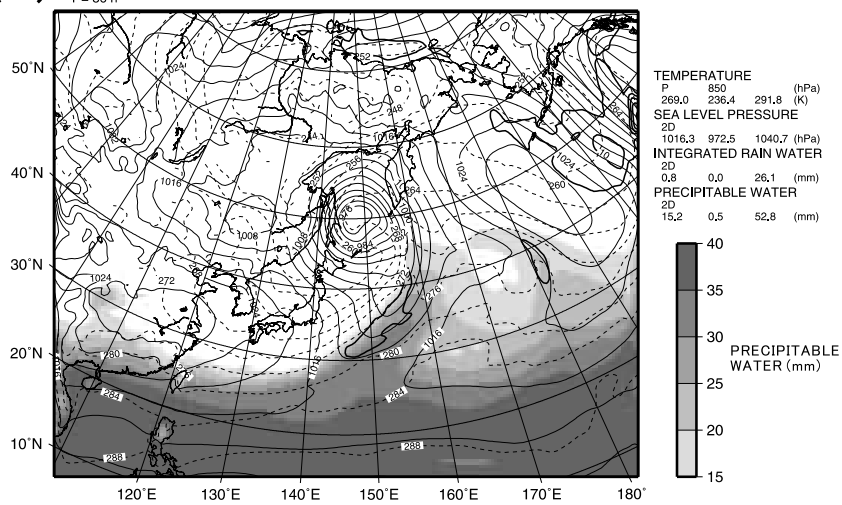


Figure 35. Same as Fig. 25, but of the extreme OJ DRY.

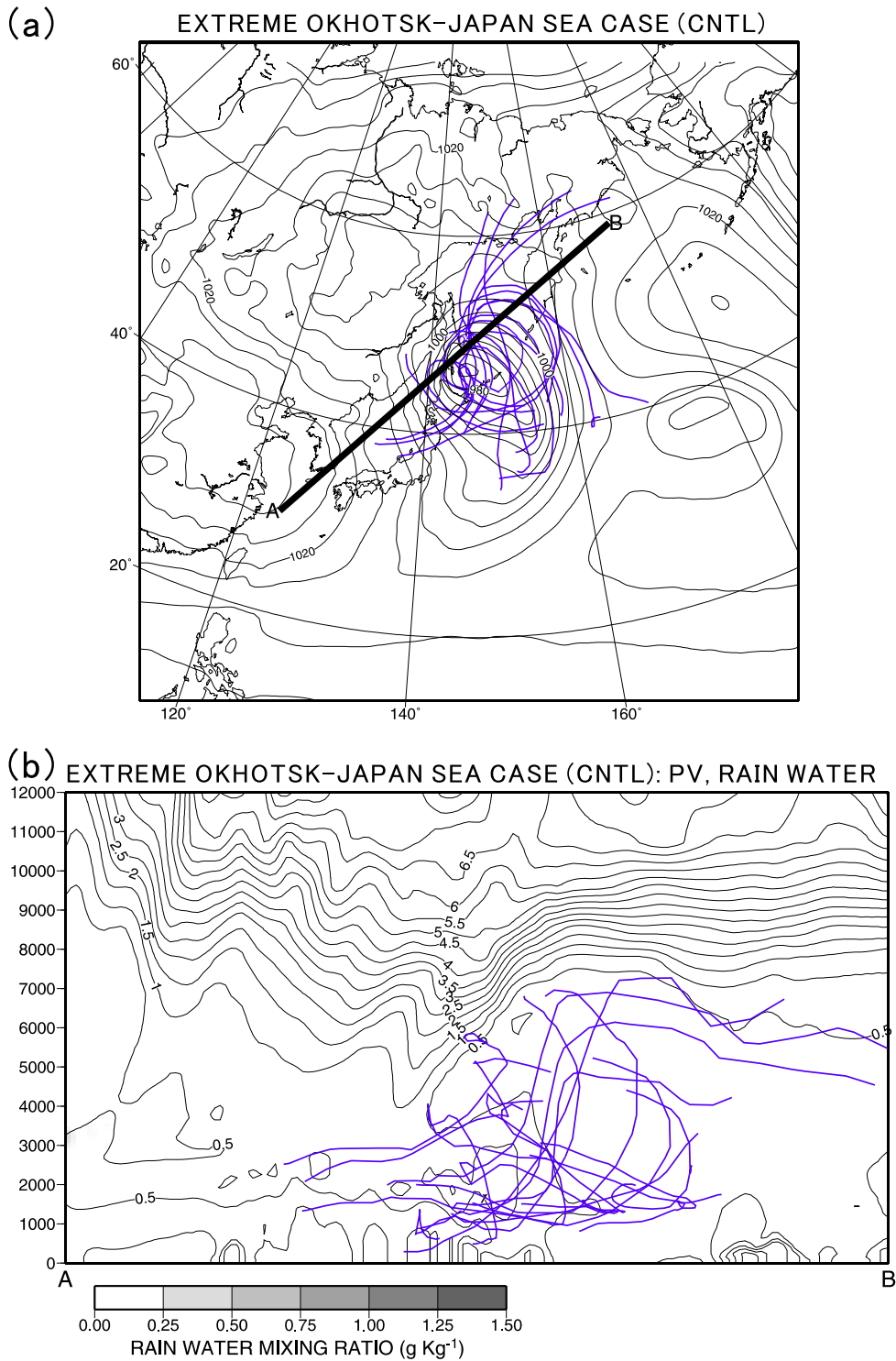


Figure 36. Trajectories rising near the surface cyclone center (medium bold solid line) and sea level pressure (thin solid line) of the extreme OJ CNTL. (b) Cross section of projected trajectories rising near the surface cyclone center (bold solid line), potential vorticity (thin solid line, unit of PVU ( $= 10^{-6} \text{ m}^{-2} \text{ s}^{-1} \text{ K kg}^{-1}$ ), contour interval is 0.5 PVU), rain water mixing ratio averaged during simulation term (shade, unit of  $\text{g kg}^{-1}$ ) along A-B line in (a).

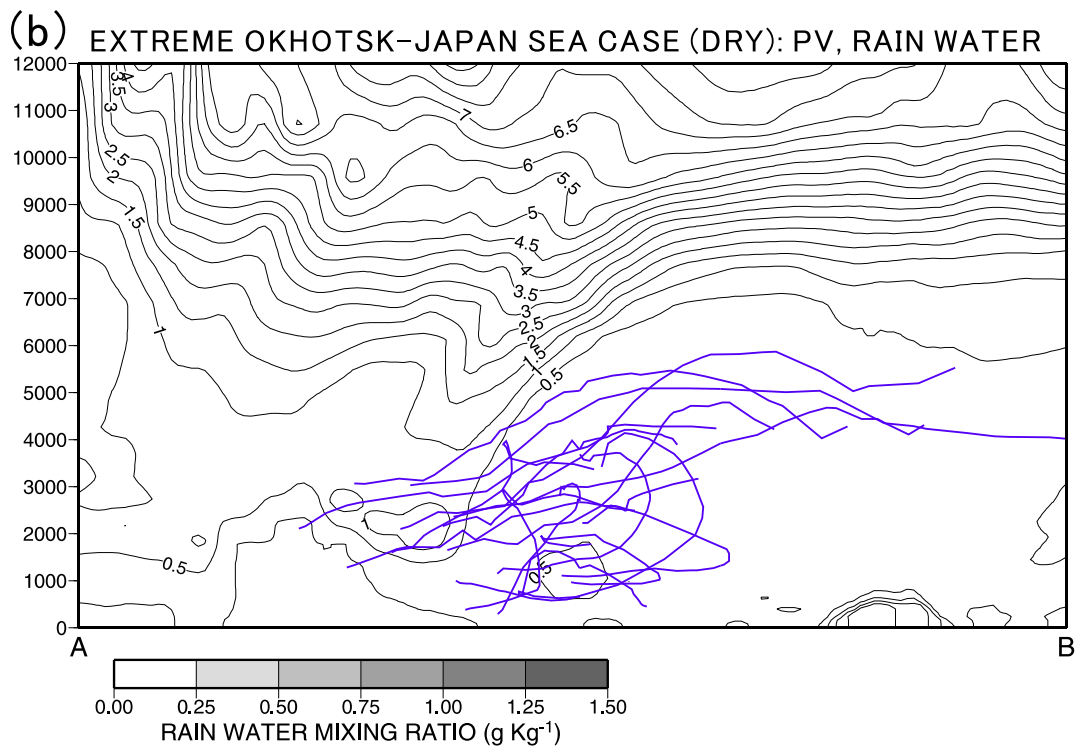
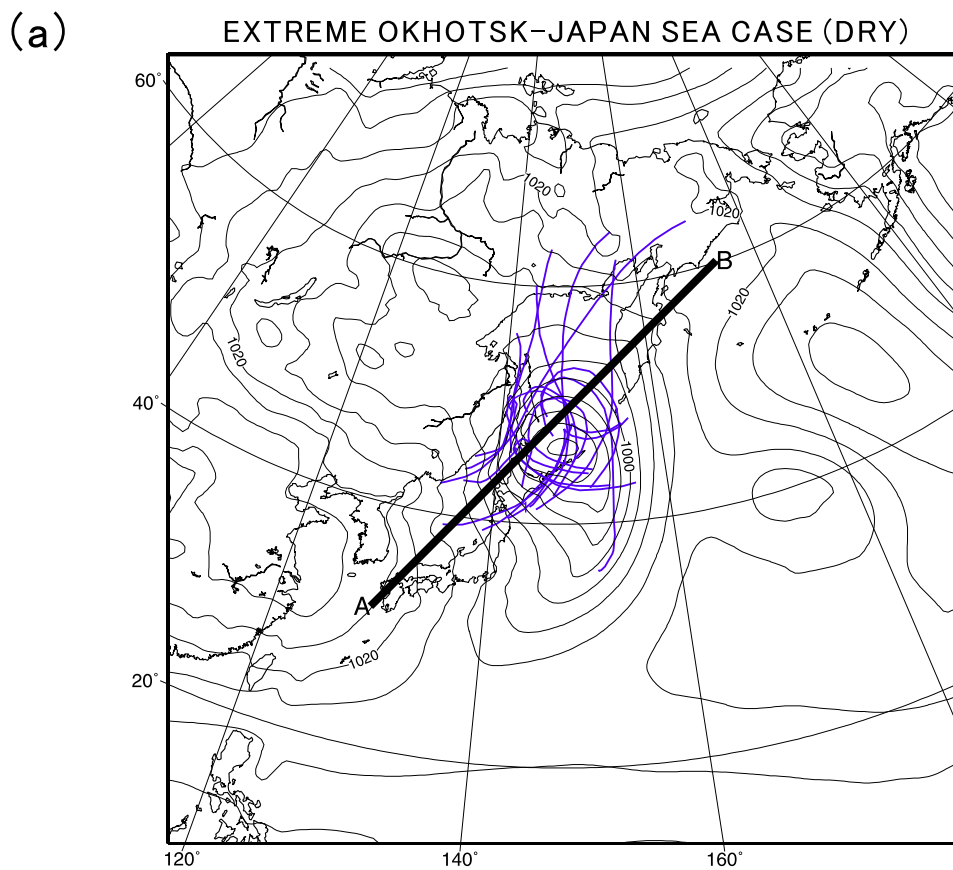


Figure 37. Same as Fig. 36, but of the extreme OJ DRY.

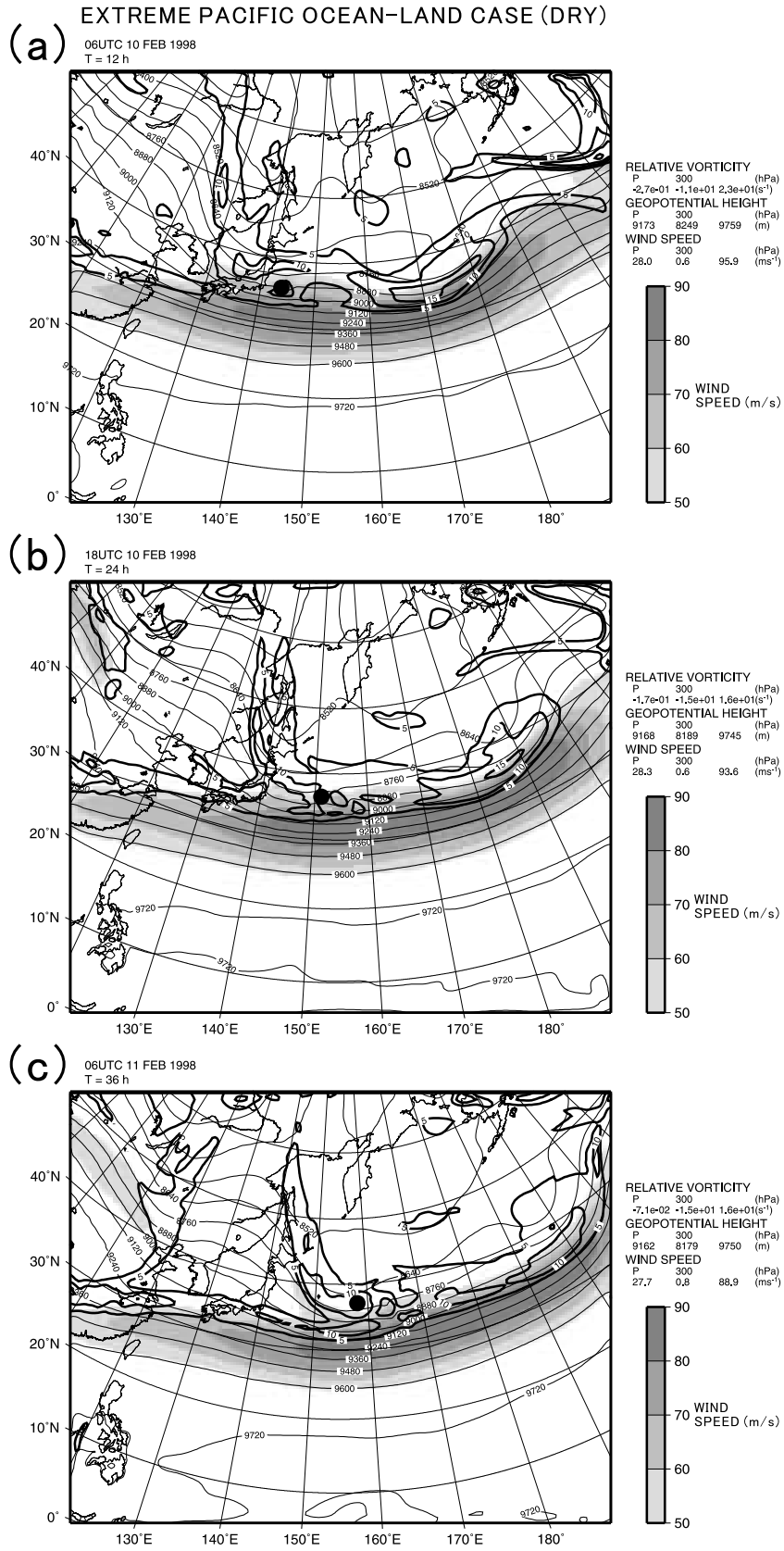


Figure 38. Same as Fig. 24, but of the extreme PO-L DRY.

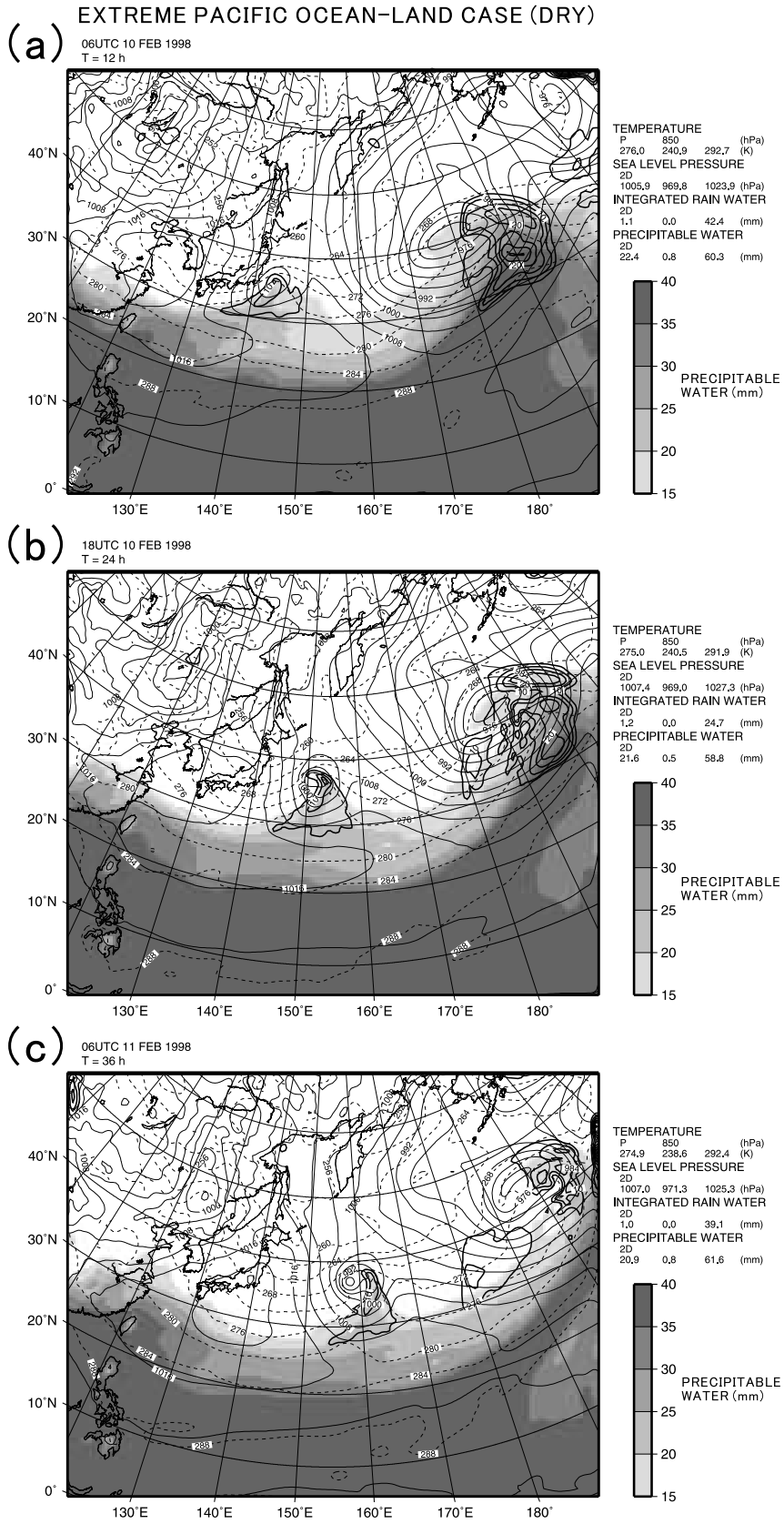


Figure 39. Same as Fig. 25, but of the extreme PO-L DRY.

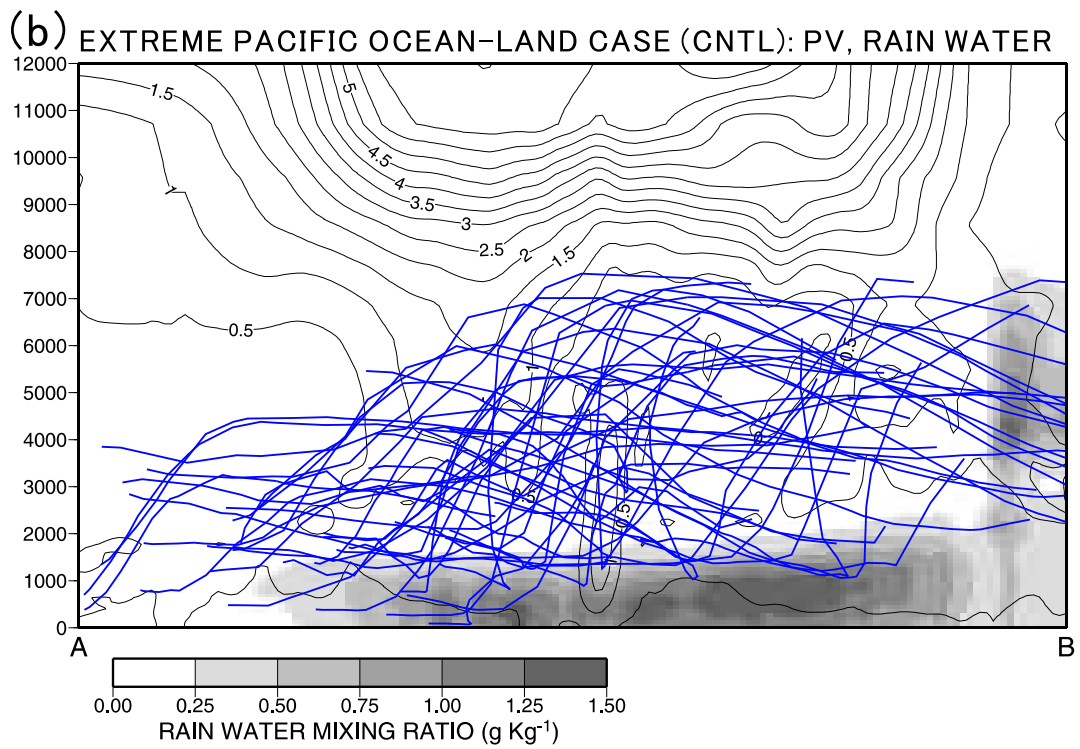
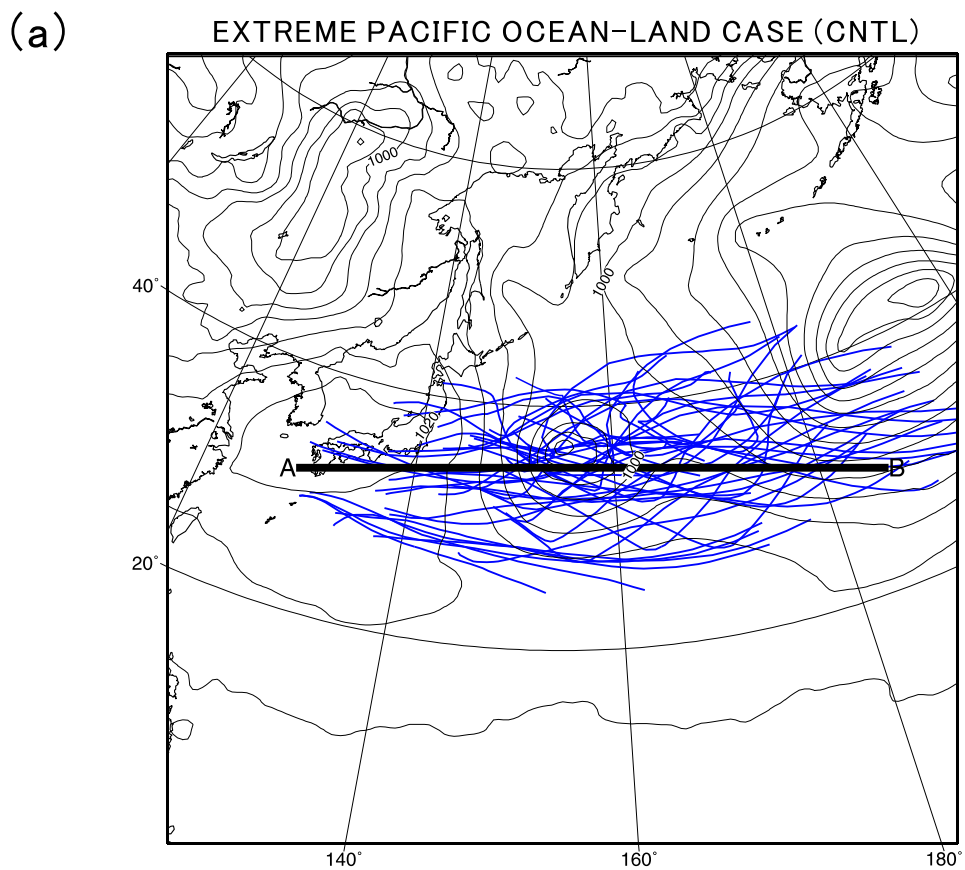
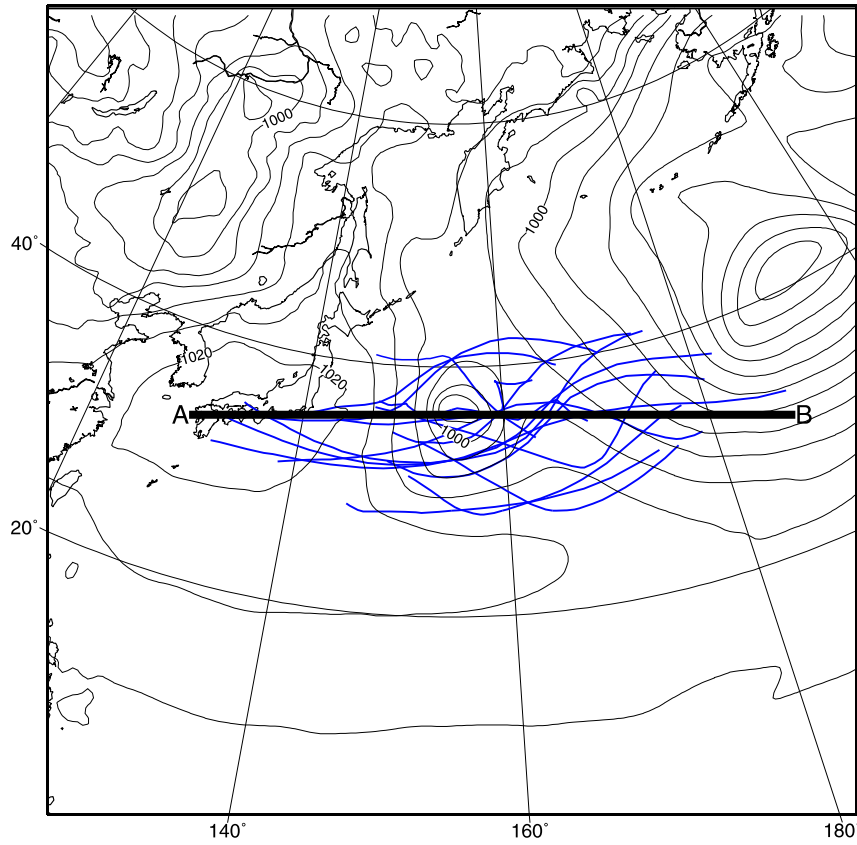


Figure 40. Same as Fig. 36, but of the extreme PO-L CNTL.

(a)

EXTREME PACIFIC OCEAN-LAND CASE (DRY)



(b)

EXTREME PACIFIC OCEAN-LAND CASE (DRY): PV, RAIN WATER

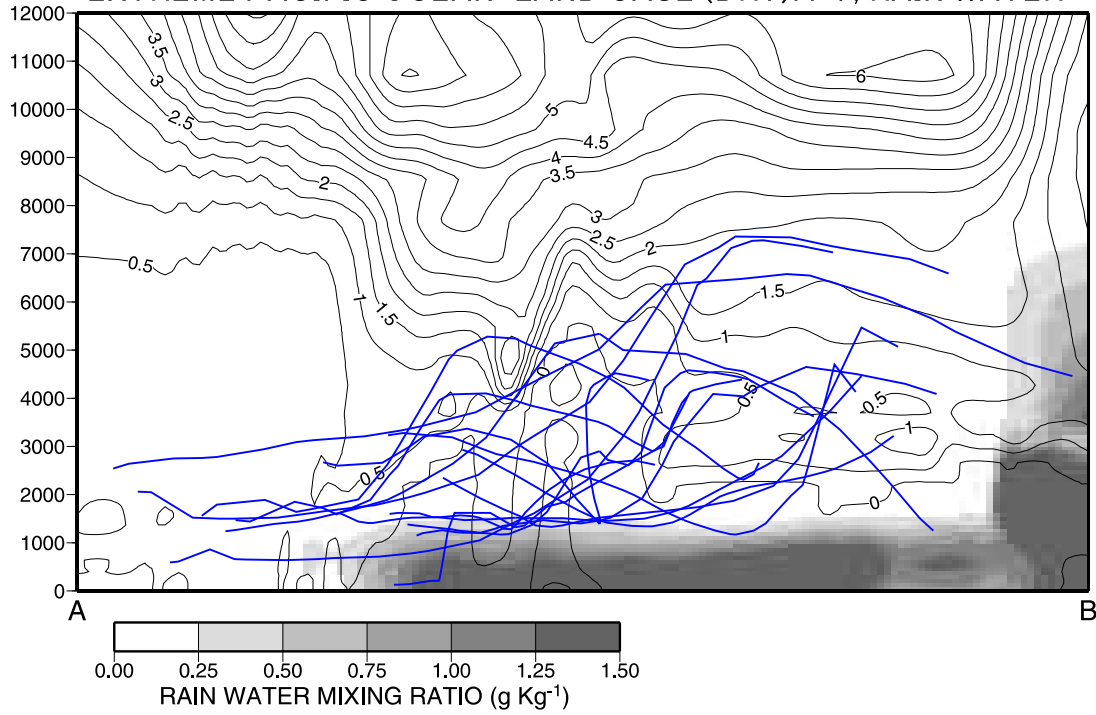


Figure 41. Same as Fig. 36, but of the extreme PO-L DRY.

EXTREME PACIFIC OCEAN-OCEAN CASE (DRY)

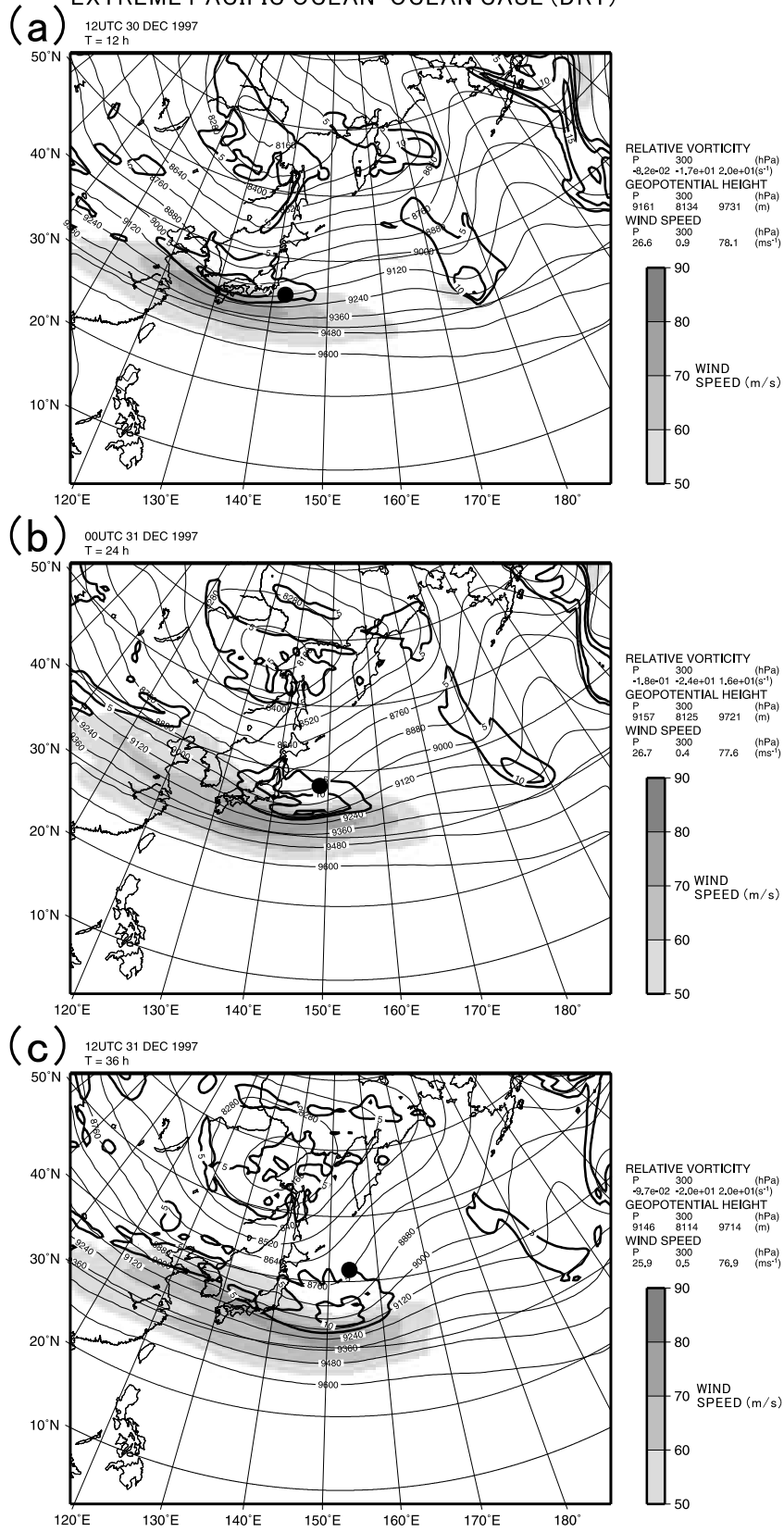


Figure 42. Same as Fig. 24, but of the extreme PO-O DRY.

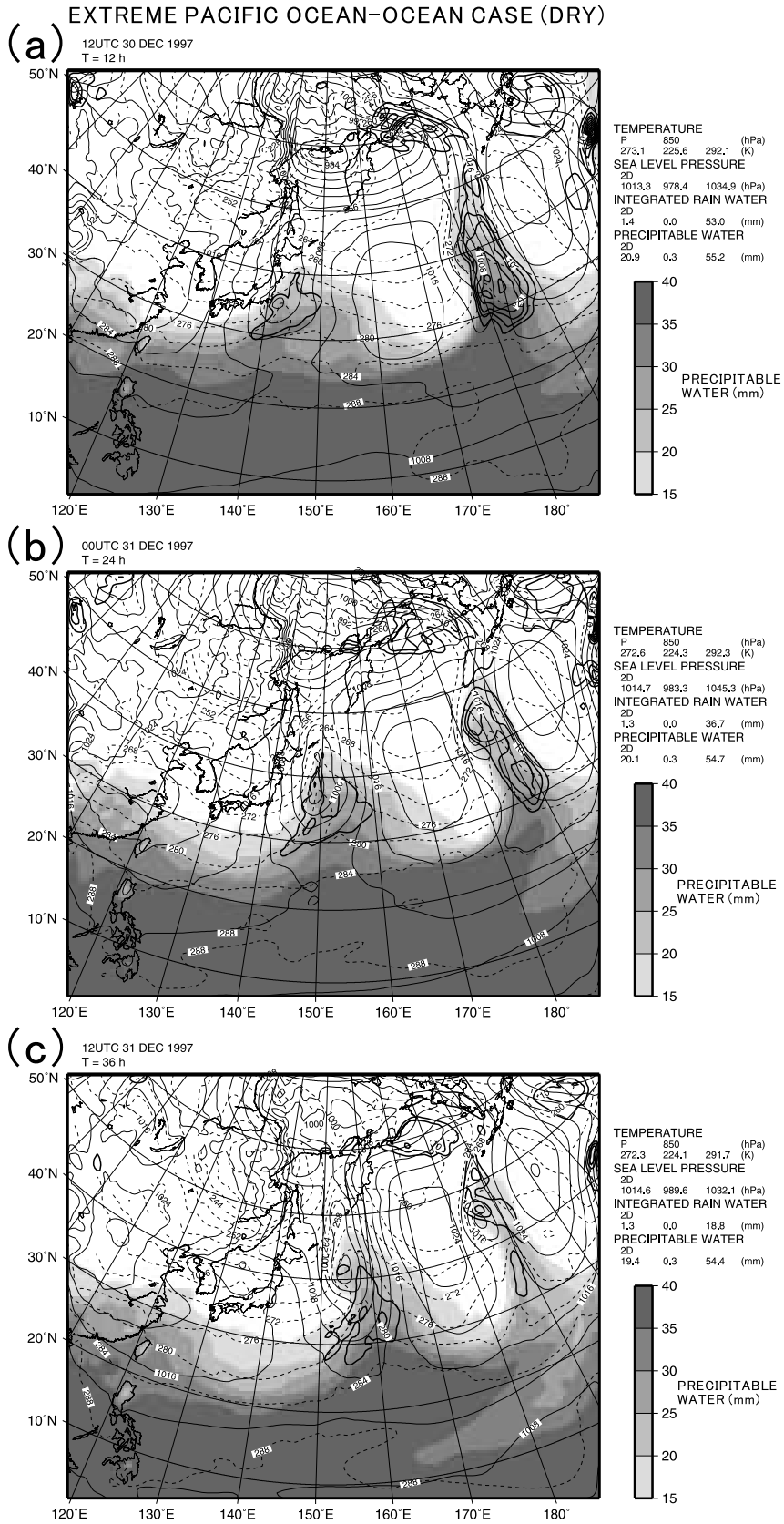


Figure 43. Same as Fig. 25, but of the extreme PO-O DRY.

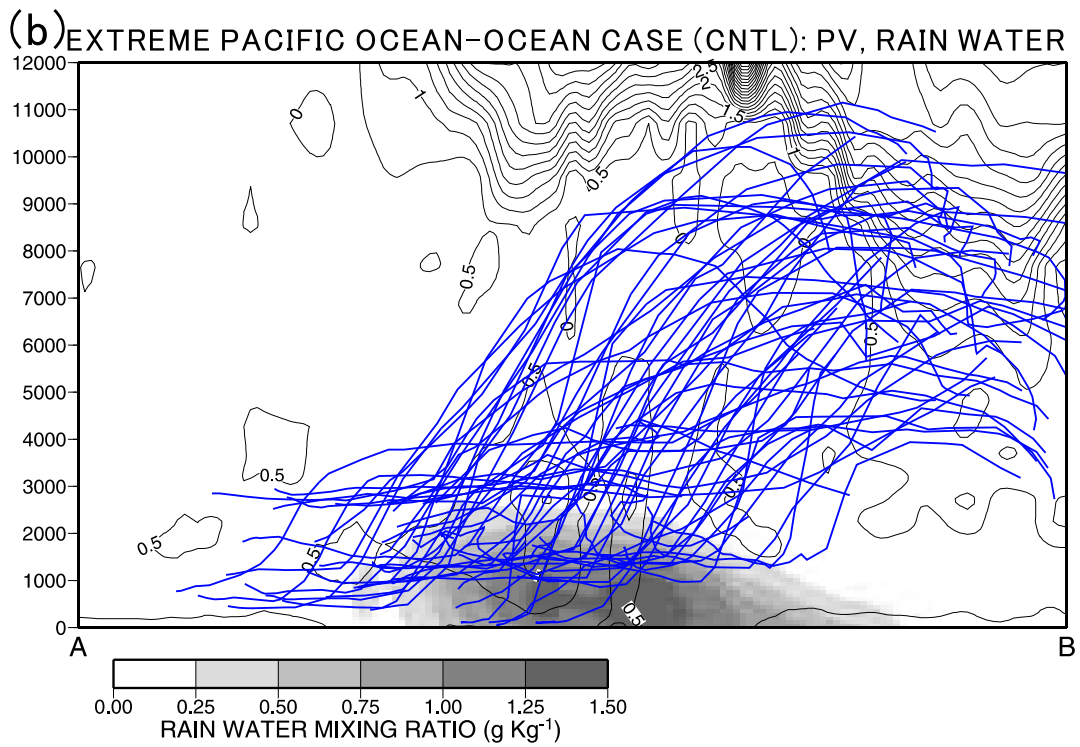
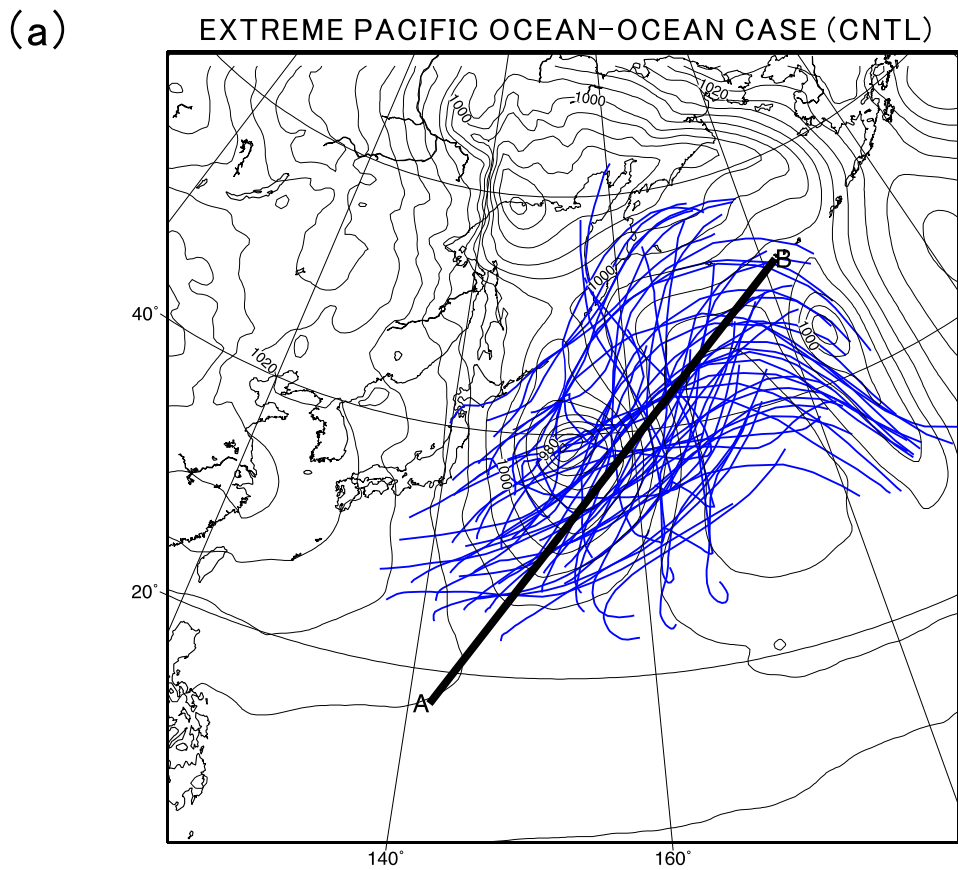
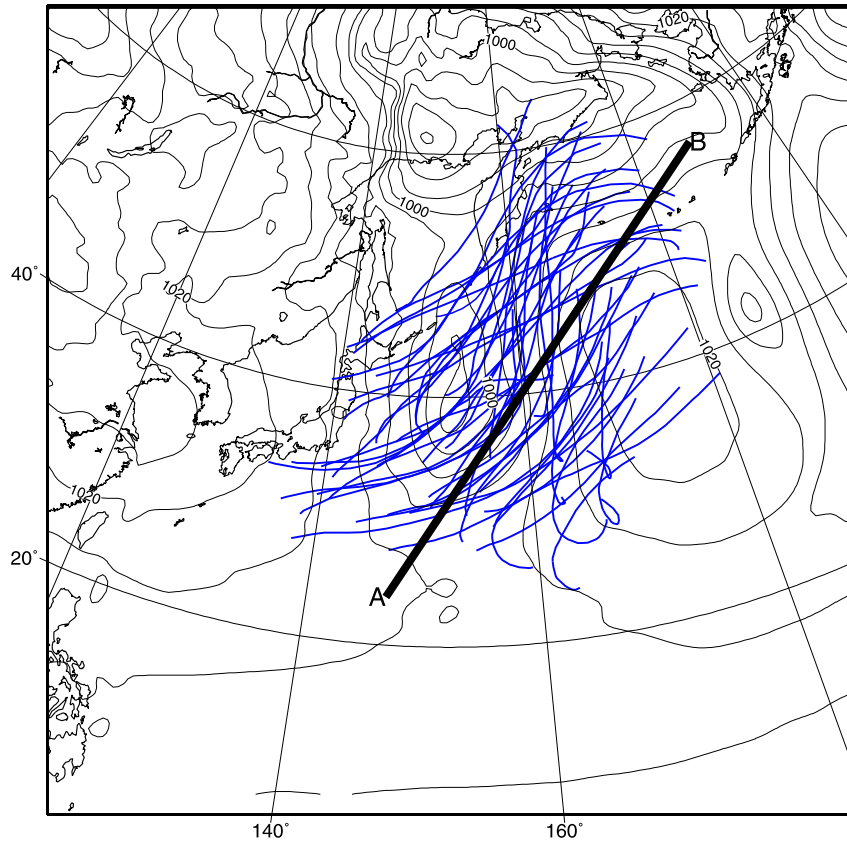


Figure 44. Same as Fig. 36, but of the extreme PO-O CNTL.

(a)

EXTREME PACIFIC OCEAN-OCEAN CASE (DRY)



(b)

EXTREME PACIFIC OCEAN-OCEAN CASE (DRY): PV, RAIN WATER

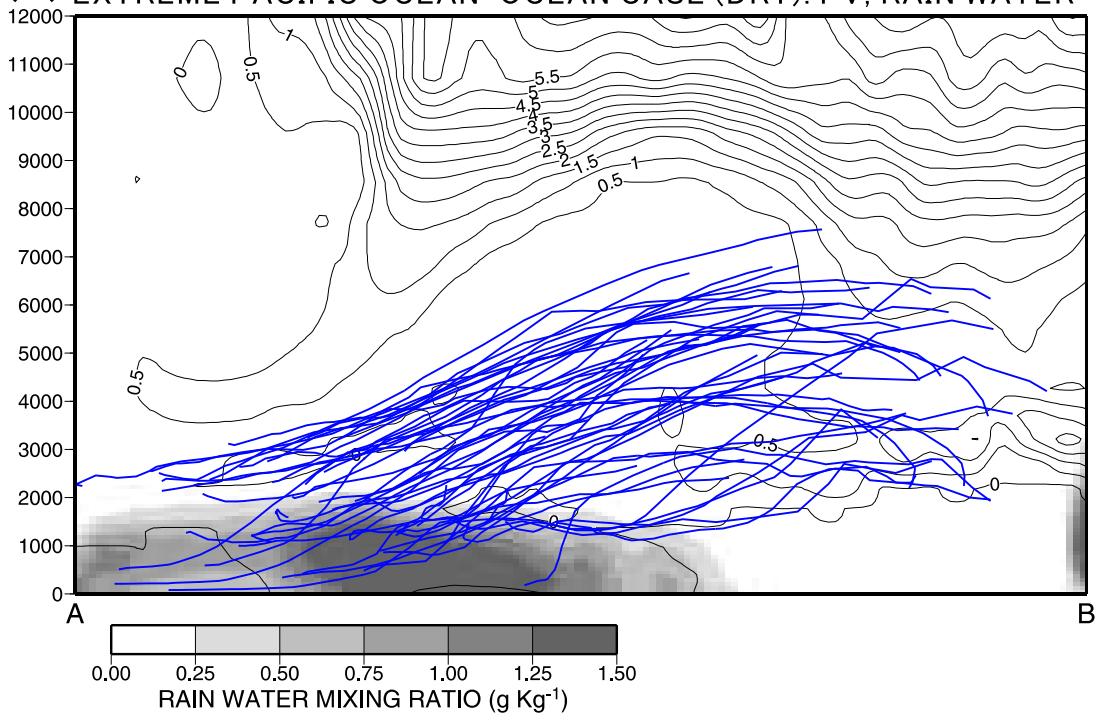


Figure 45. Same as Fig. 36, but of the extreme PO-O DRY.

MONTHLY AVERAGED FIELDS IN THE NORTH ATLANTIC REGION  
300 hPa Z,  $\zeta$

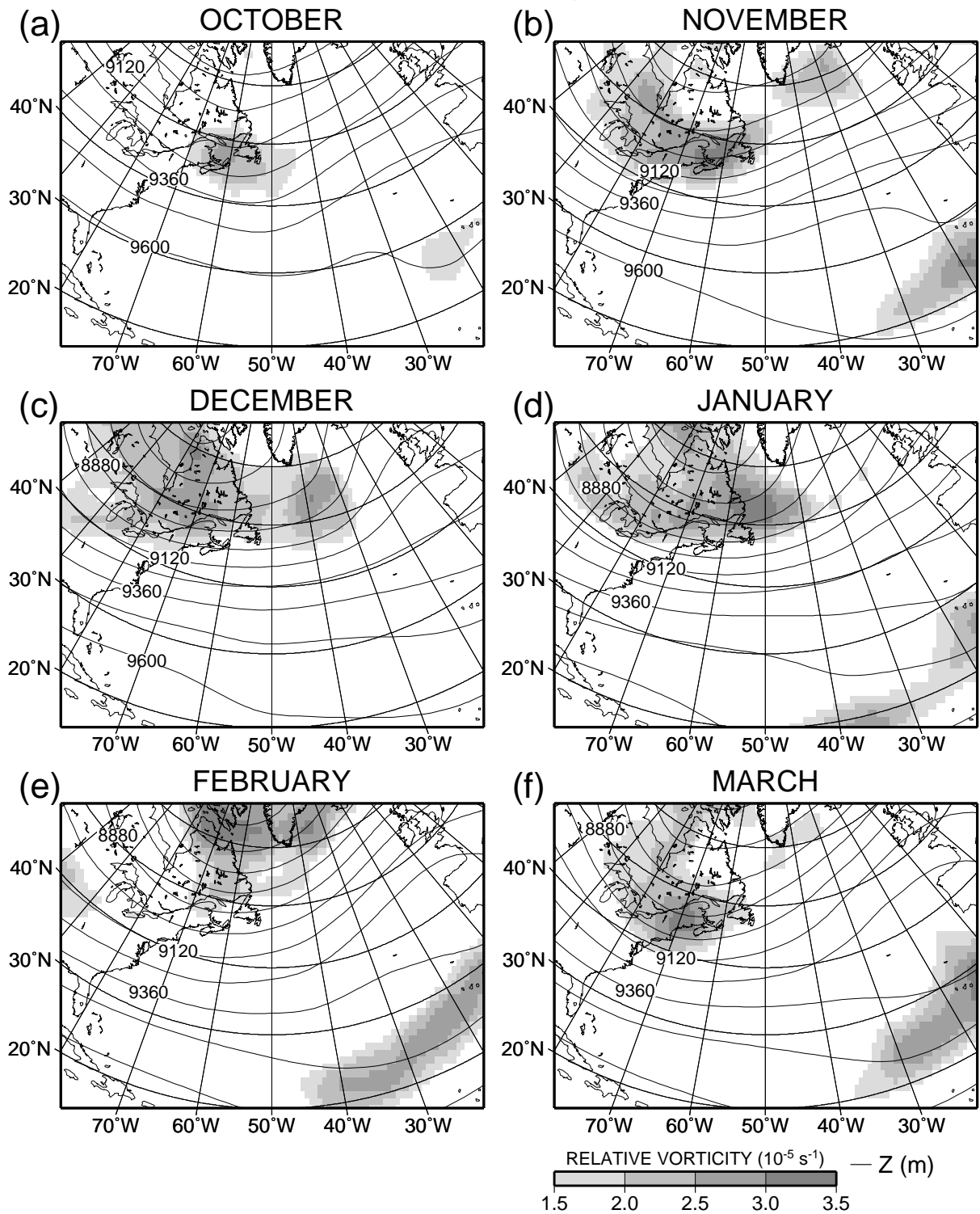


Figure 46. Same as Fig. 9, but for the North Atlantic region.

MONTHLY AVERAGED FIELDS IN THE NORTH ATLANTIC REGION  
850 hPa  $\theta$ ,  $|\nabla\theta|$

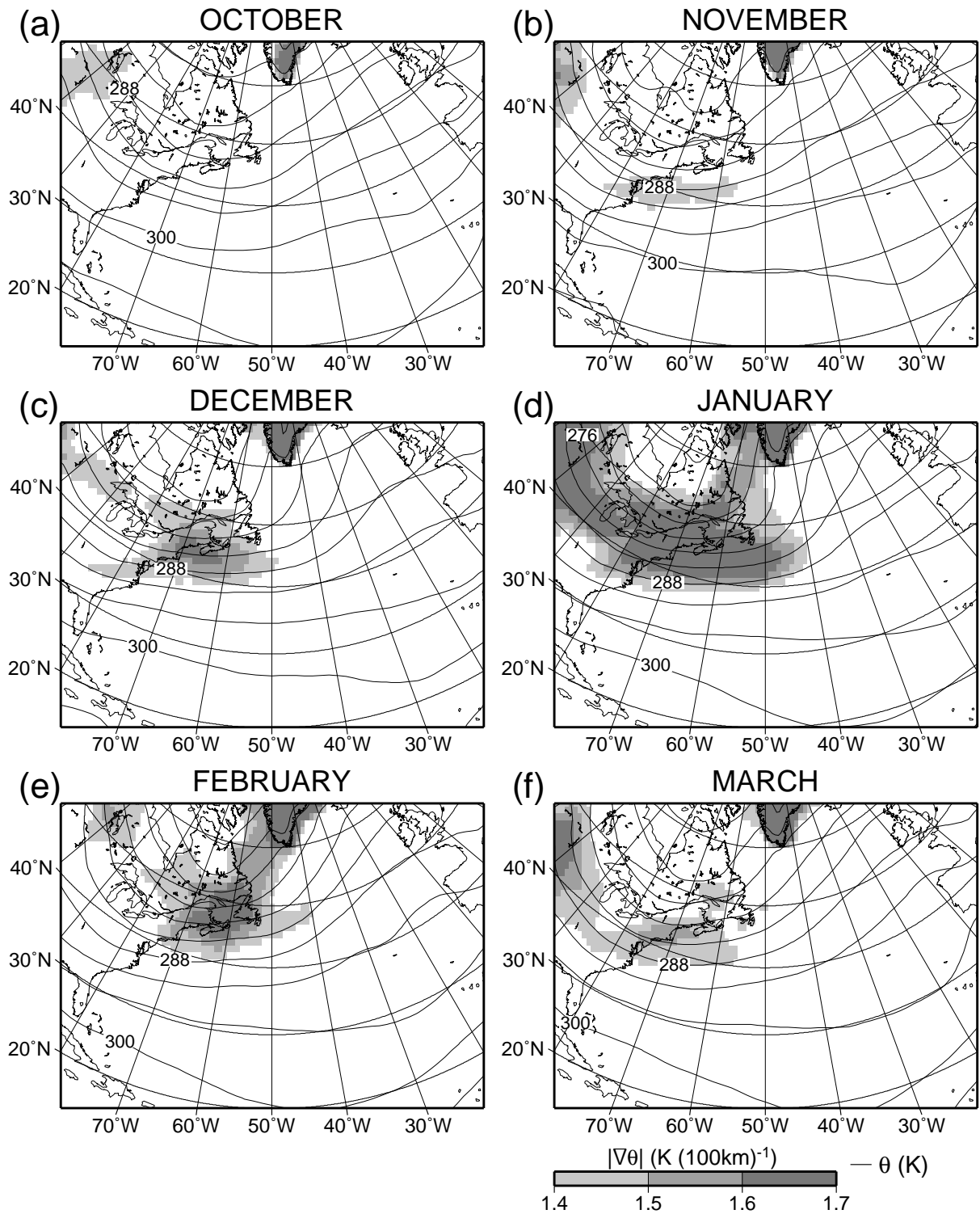


Figure 47. Same as Fig. 10, but for the North Atlantic region.

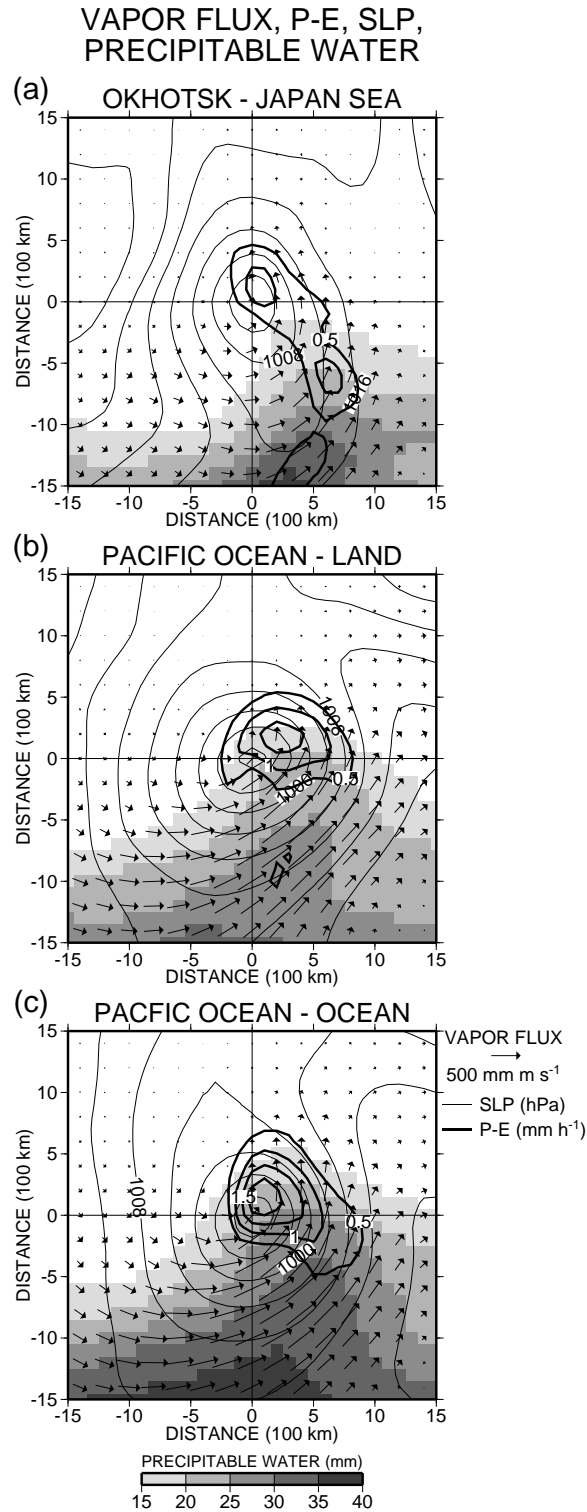


Figure 48. Moisture composite analyses at the maximum deepening rate for (a) OJ, (b) PO-L, and (c) PO-O cyclones. Bold solid lines show positive P–E (P: precipitation, E: evaporation, in  $\text{mm h}^{-1}$ , contour interval is  $0.5 \text{ mm h}^{-1}$ ), thin solid lines show the sea level pressure in hPa (contour interval is 4 hPa), gray scale shows precipitable water in mm, and arrows show vertically integrated horizontal water vapor flux. A center of each panel shows the surface cyclone center.

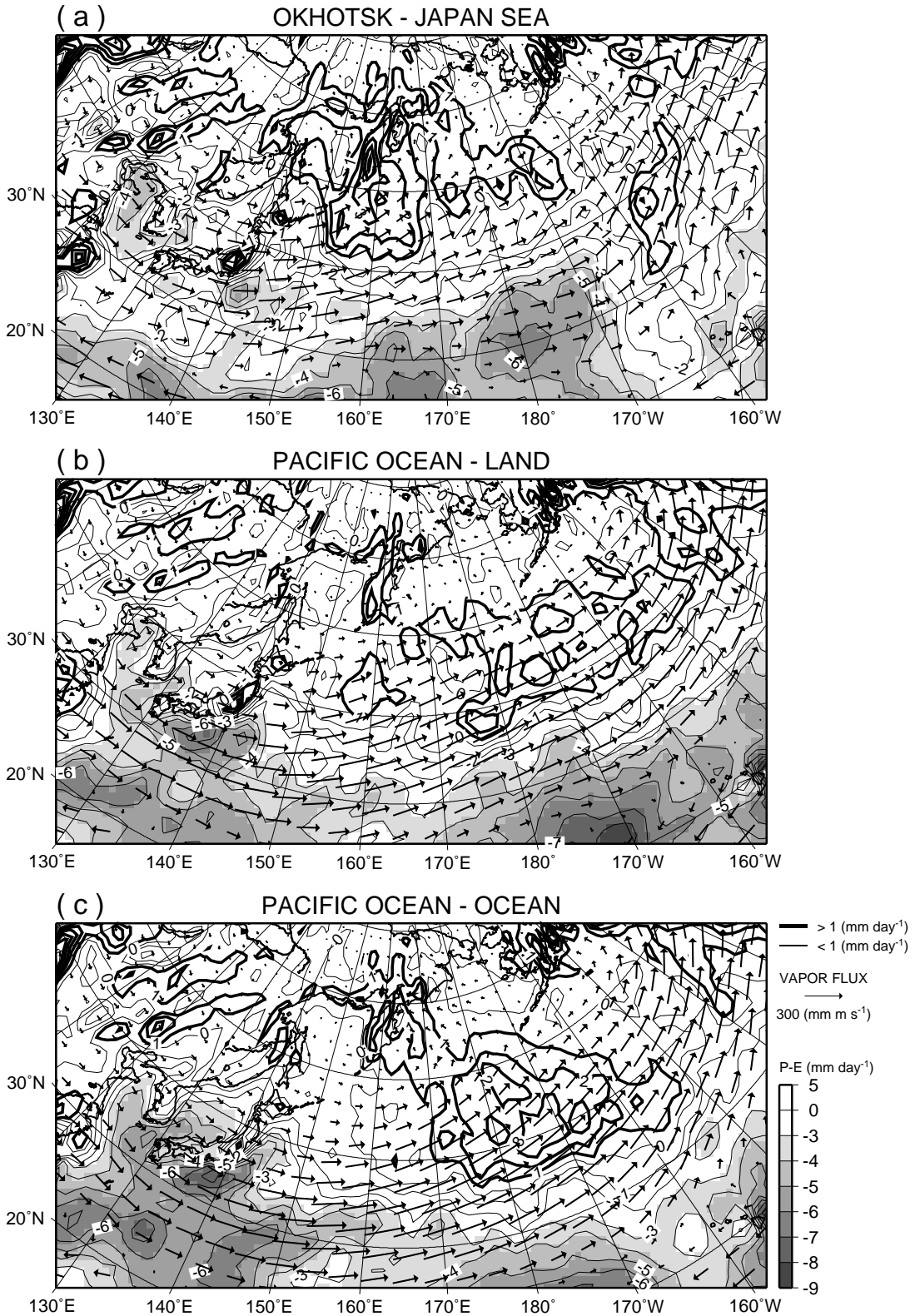


Figure 49. Composite charts of vertically integrated water vapor flux (arrow), P–E (unit of mm day<sup>-1</sup>, shade with bold solid line is over 1 mm day<sup>-1</sup>, thin solid line under 1 mm day<sup>-1</sup>, contour interval is 1 mm day<sup>-1</sup>) averaged between formation and minimum central sea level pressure for (a) OJ, (b) PO-L, and (c) PO-O cyclones.

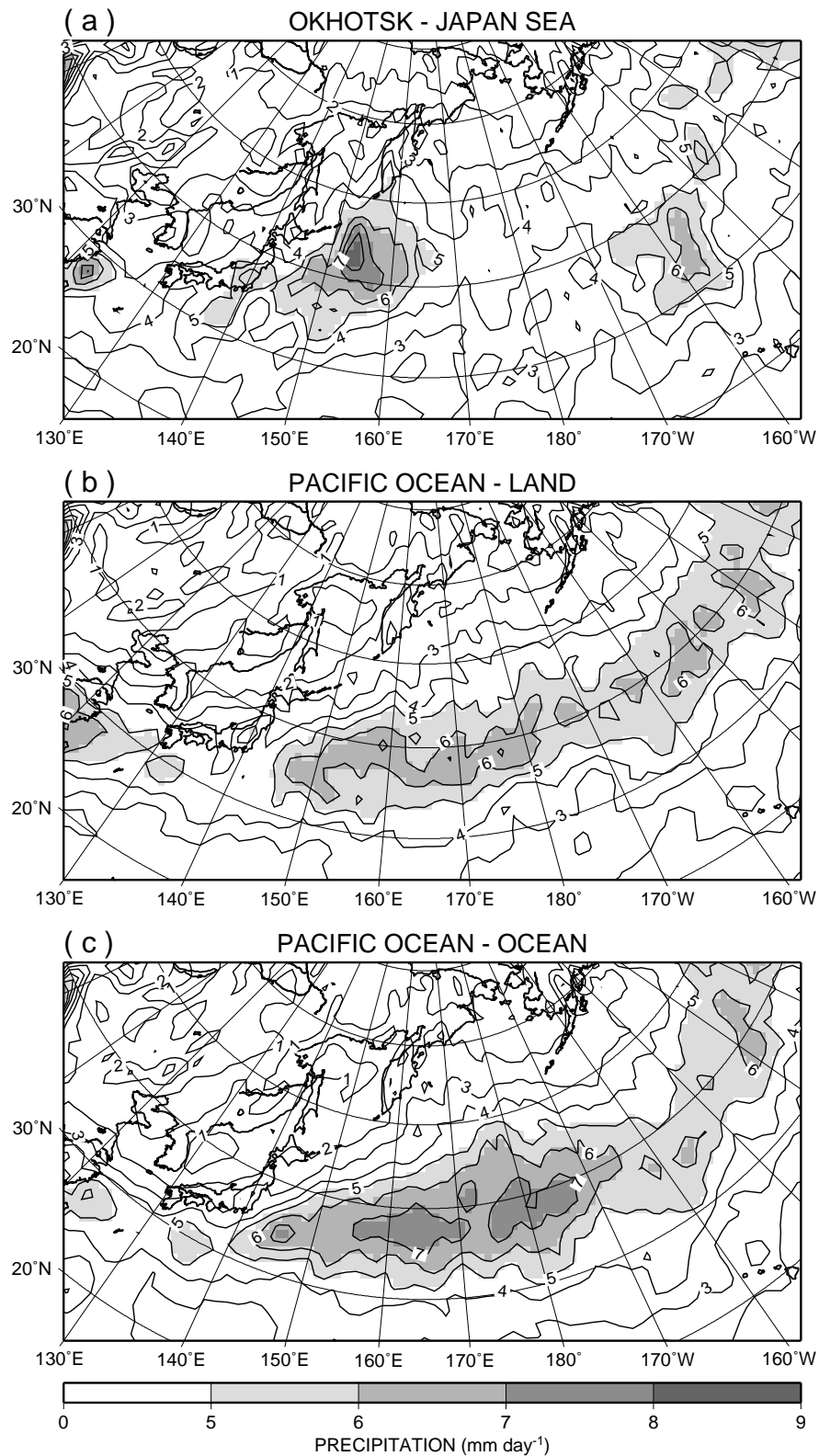


Figure 50. Composite charts of positive P–E averaged between formation and minimum central sea level pressure (solid line and shade, unit of  $\text{mm day}^{-1}$ , contour interval is  $1 \text{ mm day}^{-1}$ ) for (a) OJ, (b) PO-L, and (c) PO-O cyclones.

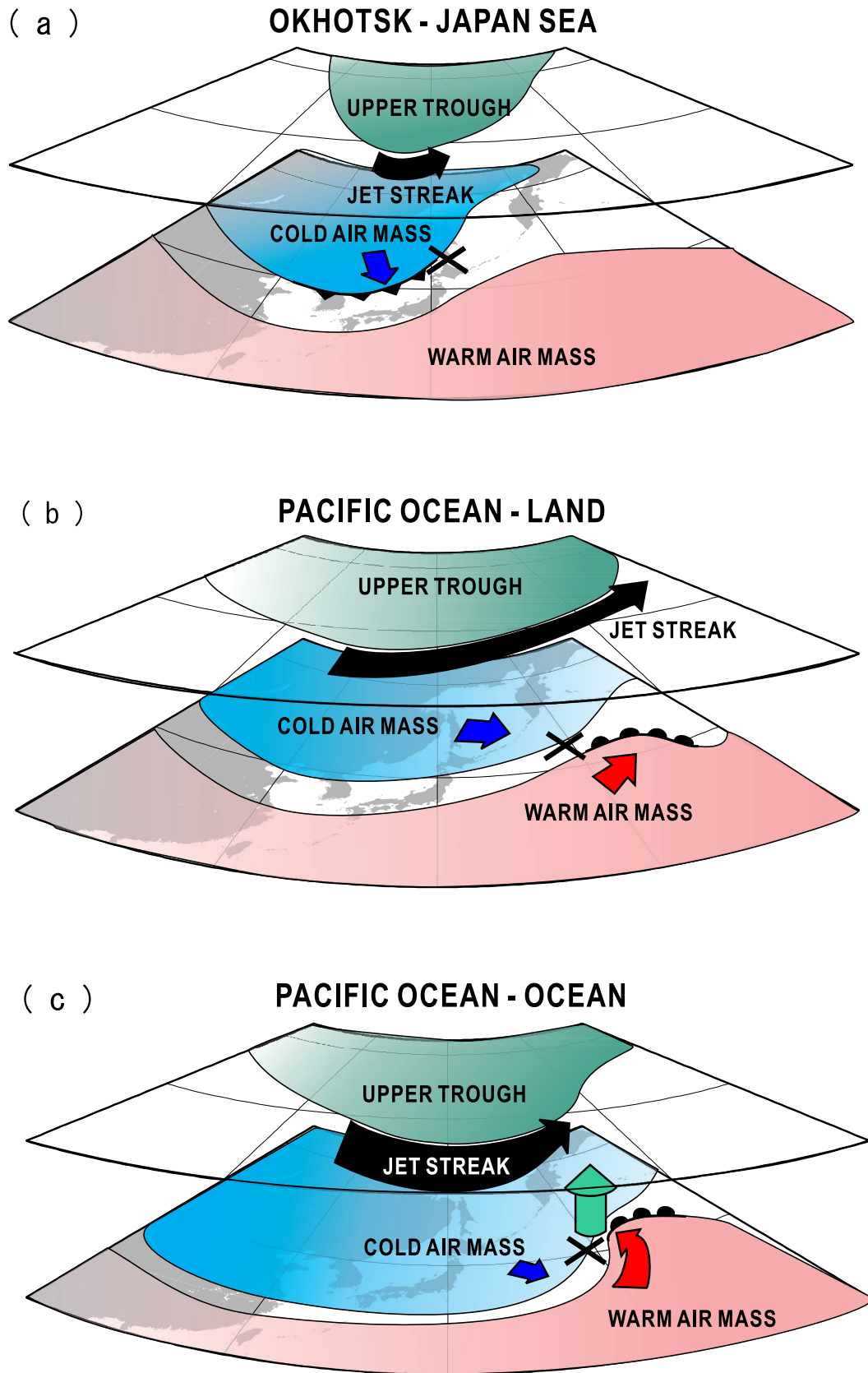


Figure 51. Schematics illustrations of the three types of cyclones. (a) OJ cyclone, (b) PO-L cyclone, (c) PO-O cyclone.